Processing and Properties of Multifunctional Polylactide/Graphene Composites

Yuqing Gao

2017

SUBMITTED IN PARTIAL FULFILMENT OF THE REQUIREMENTS OF THE DEGREE OF DOCTOR OF PHILOSOPHY AT QUEEN MARY UNIVERSITY OF LONDON

Statement of Originality

I, Yuqing Gao, confirm that the research included within this thesis is my own work or that where it has been carried out in collaboration with, or supported by others, that this is duly acknowledged below and my contribution indicated. Previously published material is also acknowledged below.

I attest that I have exercised reasonable care to ensure that the work is original, and does not to the best of my knowledge break any UK law, infringe any third party's copyright or other Intellectual Property Right, or contain any confidential material.

I accept that the College has the right to use plagiarism detection software to check the electronic version of the thesis.

I confirm that this thesis has not been previously submitted for the award of a degree by this or any other university.

Signature:

Date: 08/20

Table of Contents

Abbreviations

AFM	atomic force microscope
AR	aspect ratios
CA	cellulose acetate
CB	carbon black
CMPVA	carboxymethyl polyvinyl alcohol
CNF	carbon nanofibre
CNT	carbon nanotube
CPC	conductive polymer composite
DMA	dynamic mechanical analysis
DSC	differential scanning calorimetry
EG	expanded graphite
EVOH	ethylene vinyl alcohol
FGS	functionalized graphene sheets
FWHM	full width at half maximum
GNP	graphite nanoplatelet
GNS	graphene nanosheets
GO	graphene oxide
HDPE	high density polyethylene
HDT	heat distortion temperature
IFRs	intumescent flame retardants
LBL	layer-by-layer
LDPE	low density polyethylene
LLDPE	linear low density polyethylene
MFM	melt flow multiplication
MNT	montmorillonite
MWCNT	multi-walled carbon nanotube
OM	optical microscopy
PA	polyamide
PANI	polyaniline
PC	polycarbonate
PCL	polycaprolactone
PDMS	polydimethylsiloxane

PEI	polyethylenimine
PEN	poly(ethylene-2, 6-naphthalate)
PEO	polyethylene oxide
PET	poly(ethylene terephthalate)
PI	polyimide
PLA	polylactic acid
PMMA	poly(methyl methacrylate)
PODBS	poly(4,4'-oxybis(benzene)disulfide)
PP	polypropylene
PS	polystyrene
PU	polyurethane
PVA	poly(vinyl alcohol)
PVC	poly(vinyl chloride)
PVDF	polyvinylidene difluoride
PVOH	polyvinyl alcohol
RGO	reduced graphene oxide
RT	room temperature
S-EG	ultrasonicated expanded graphite
SEM	scanning electron microscope
SEPS	polystyrene-block-polyethylene/polypropylene-block-polystyrene
SSSP	solid-state shear pulverization
SWCNT	single-walled carbon nanotubes
TEM	transmission electron microscope
T_g	glass transition temperature
TGA	thermogravimetric analysis
TiO_2	titanium dioxide
TPU	thermoplastic polyurethane
TRG	thermally reduced graphene
WVTR	water vapour transmission rate
XRD	X-ray diffraction

Acknowledgements

It is a great pleasure to thank many people who made this thesis possible.

First, I would like to express my deepest gratitude to my two supervisors, Prof. Ton Peijs, and Dr. Emiliano Bilotti. I feel so lucky that I have two the best supervisors during my Phd. Thank you for guiding and sharing me all these valuable knowledge and skills, as well as mentoring and supporting me over these years. Your guidance and approach to education and research has been invaluable to my career.

I would also like to thank all my talented and hardworking colleagues for all the discussions, knowledge sharing, and all the help. Special thanks are given to Dr. Olivier Picot, Dr. Wei Tu, Dr. Fang Mai, Dr. Han Zhang, Dr. Rui mao, Dr Menglong Huang, Dr Jian Yao, Dr Alice Williams, Dr.Jia Ma for their support, cooperation, friendship.

Last but not least, I would like to express my deepest gratitude to my family.

Abstract

This thesis aims to utilize graphene nanoplatelets (GNPs) in biobased and biodegradable thermoplastic polylactide (PLA) matrix for improved properties and multifunctionalities. A comprehensive comparative study was carried out on the effect of the addition of GNPs with different sizes. The mechanical, electrical, thermal and barrier properties of resulting PLA/GNP nanocomposites and their inter-relationship with the microstructure of the composites is revealed. The effect of annealing on dynamic percolation and conductive network formation of PLA/GNP composites including the effect of hybrid GNP fillers of different size is reported, indicating the underlying mechanisms for different behaviours of GNP fillers of different size.

Multifunctional engineering biopolymers with improved performances (mechanical and electrical) and added functionalities (barrier properties) were successfully developed through controlled filler distribution and orientation using multilayer co-extrusion technology. Changes in mechanical properties of the PLA/GNP multilayer nanocomposites were successfully correlated with GNP orientation in the filled layers. Multilayer PLA/GNP nanocomposites demonstrated excellent mechanical and barrier properties with low filler loadings compared to traditional mono-extruded films.

List of Tables

List of Figures

Chapter 1 - Introduction

1.1 Research background

Graphene exhibits extraordinary characteristics, ranging from high intrinsic mechanical properties to excellent electrical conductivity and optical transparency. These properties open new opportunities to revolutionise a variety of practical applications, e.g. multifunctional composites, detectors, smart wearables, paints and printing. However, practical advances will depend on our ability to use these two dimensional (2D) building blocks to construct complex three dimensional (3D) highly organised structures with practical dimensions while being able to manipulate chemistry and architecture at multiple length scales.

Nature-made nanocomposites usually exhibit superior properties than those of man-made composites. For instance, nacre is composed of 95% of mineral platelets and the toughness is nearly 3000 times higher than the building block mineral particle. Such biocomposites usually containing several levels of hierarchy, ranging from macroscale to nanoscale [1]. In contrast, traditional nanocomposites, as produced by melt-mixing, solution casting or in-situ polymerization, have generally a relatively low reinforcing efficiency because of difficulties in creating nanocomposites which display homogeneous dispersions of these nanoparticles, good interfacial adhesion between particles and matrix, and high levels of structural organisation of these particles within the matrix [2].

1.2 Aims of research

In this thesis, the aim is to utilize graphite nanoplatelets (GNPs) as nano-scale reinforcements in polymer composites and achieve optimized mechanical, electrical, thermal and barrier properties. To achieve this, GNPs of different size will be used as fillers in biobased polylactide (PLA) and different processing routes including traditional melt-mixing and compression

moulding, as well as a multilayer coextrusion methodologies will be applied. The relationship between the microstructure of the composites and their resulting properties will be studied.

1.3 Outline of thesis

This thesis presents an overview of producing PLA/GNP composites through traditional melt-compounding and moulding, and mono-extrusion as well as multilayer coextusion technology and shows the relationship between microstructure of the nanocomposites and their various properties.

Background knowledge of graphene and its polymer composites is presented in Chapter 2, with a focus on the various properties, together with a detailed review on polylactide (PLA) based composites. A review on composites made by multilayer coextrusion methods is also provided.

Lab-scale micro-compounding was used to produce graphite nanoplatelet (GNP) based composites in Chapter 3, using a bio-based polymer, polylactide (PLA), with the aim to have a comprehensive understanding of the effect of GNP size on various properties of composite, including morphology, mechanical, electrical and rheological properties. In addition to this, we discuss the enhancement of electrical conductivity of PLA/GNP composites through thermal annealing and studied the differences in dynamic percolation behaviour of composites with different GNP filler sizes in Chapter 4.

Although composites with good mechanical performances can be made using melt-compounding technology such as twin-screw extrusion, these technologies have limitation with respect to producing highly organised composites. To improve the in-plane orientation of the GNPs in nanocomposite films, forced assembly multilayer co-extrusion technology was used in Chapter 5 to produce highly organised PLA/GNP films. Structure-properties relationships and micro-confinement effects of these multilayer films were revealed.

The thesis concludes with conclusions as well as ideas for future work in Chapter 6.

Chapter 2 - A literature review of polymer/graphene composites

2.1 Introduction to graphene

Graphene is composed of sp^2 carbon atoms organised in a 2D hexagonal lattice structure as shown in Figure 2.1 [3]. Ideally it can be regarded as the basic building element of all other carbon materials. For example, 0D fullerenes can be viewed as wrapped-up graphene, 1D nanotubes as rolled-up graphene and 3D graphite as stacked layers of graphene. Single-layer graphene was first isolated from graphite in 2004 [3] and since then numerous research have been conducted on its exceptional mechanical, thermal and electrical properties [3,4].

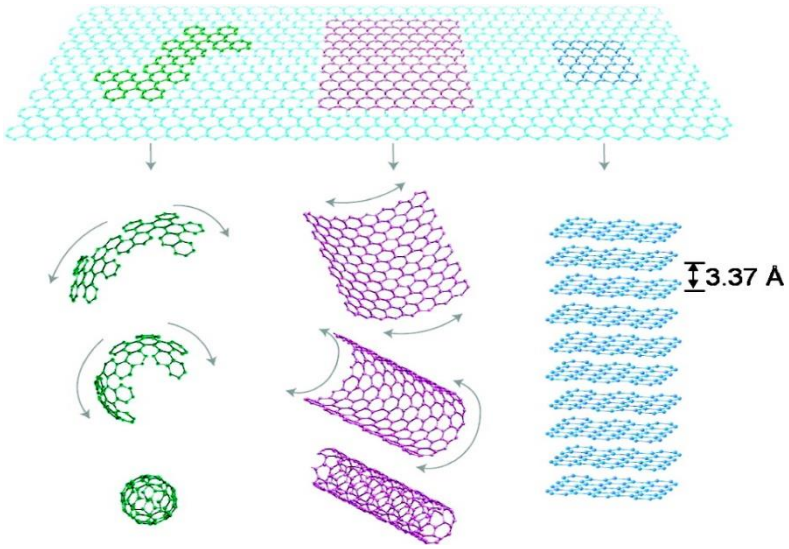

Figure 2.1. Graphene visualized as the building elements for 0D buckyballs, 1D nanotube and 3D graphite. Reproduced from [3].

In the last decade, researchers have successfully produced graphite nanoplatelets (GNP), which was thinner than traditional expanded graphite (EG). GNP is a 2D filler made up of several layers of single graphene sheets. The weak van der Waals forces tie these layers together and a distance of ca. 0.34 nm was reported between individual layers [5]. In contrast to traditional 2D nanofillers including nanoclays, GNPs possess high thermal and electrical conductivity with lower mass density. Hence, GNPs becomes an ideal filler for enhancing the properties of polymers and introducing multifunctionalities in composites. Moreover, the production costs for GNPs are relatively low [5–7] compared to that of carbon nanotube (CNTs). Plus, GNPs can also be obtained from an abundant natural sources like graphite [9,10], which makes GNP a cost-effective replacement for carbon nanotubes.

The past few years have witnessed polymer/GNP nanocomposites becoming a popular area of research [11–15]. Remarkable quantities of work were conducted on producing monolayer graphene sheets, corresponding oxides or GNPs which contain only very few sheets of graphene [16–22]. Nevertheless, it remains very challenging to produce monolayer graphene in large quantities while keeping their outstanding properties. The progress of polymer/graphene nanocomposites has been reviewed extensively [17,23–26] and shows that polymer/GNP nanocomposites have increasing practical applications because of their interesting properties and simplicity of fabrication.

This chapter will focus on providing a comprehensive overview of recent research in the field of polymer/GNP nanocomposites, encompassing properties, fabrication and related theories. Properties of other nanocarbon based polymer composites will also be compared, although CNTs, graphene oxide (GO) and functionalized graphene sheets (FGS) and their derivatives will not be discussed in detail.

2.2 Properties of graphene

In this chapter, we will mainly discuss the mechanical and electrical properties of graphene based on single layer, few layer and multilayers.

2.2.1 Mechanical properties

The C-C covalent bond is considered to be one of the strongest atomic bonds in nature. Pioneering measurements showed that single layer graphene exhibited a high Young's modulus of 1 TPa and an strength of 130 GPa by Lee et al. [27]. A representative stress–strain curve was obtained through nanoindenting graphene membranes in an atomic force microscope (AFM) and is shown in Figure 2.2, along with the theoretical prediction by Liu et al. [28] using the density functional theory.

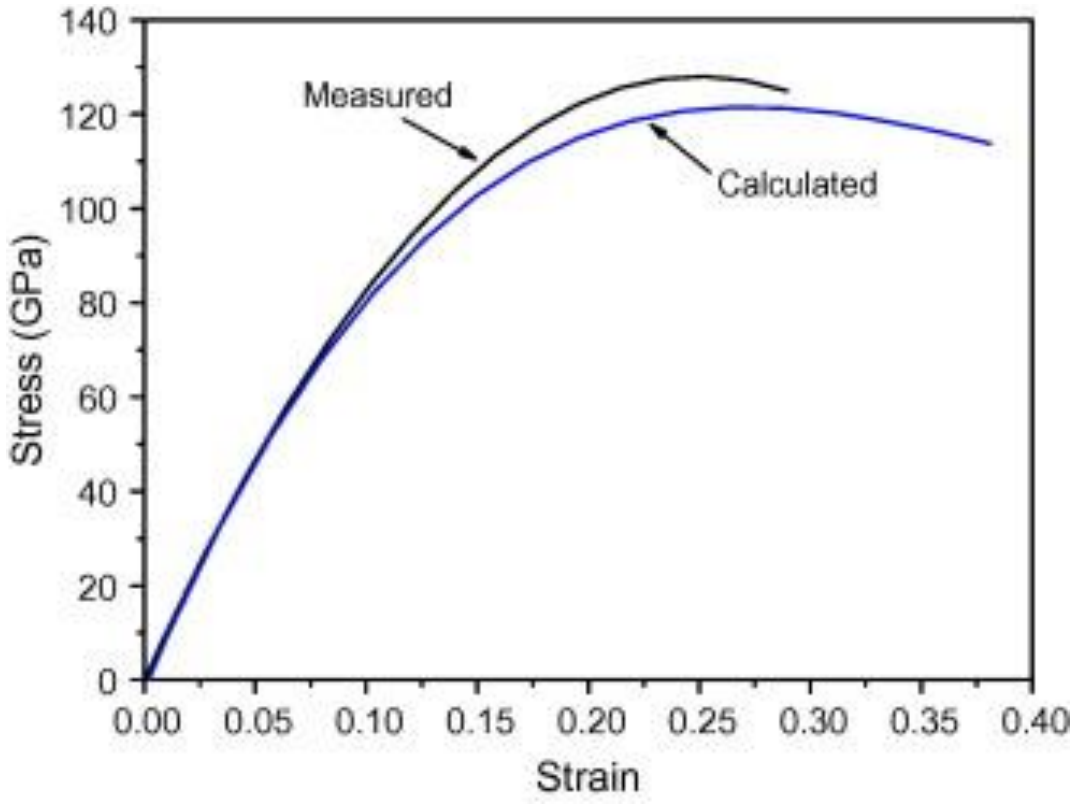

Figure 2.2. Experimental and theoretical stress–strain curves for graphene monolayer. Reproduced from [4].

Such experiments reported the Young's modulus as 1000 ± 100 GPa, which is similar to the theoretical estimated value of 1050 GPa. This is also very close to that of 1020 GPa for bulk graphite [29]. This value is presented in Figure 2.3 and compared with traditional materials.

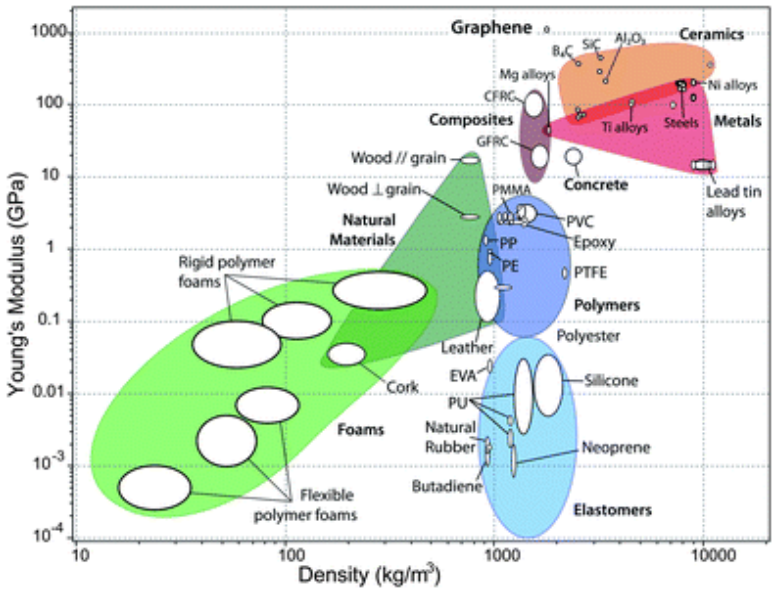

Figure 2.3. Comparison between traditional materials and graphene. Reproduced from [30].

Raman spectroscopy is a good tool to probe the mechanical performance of graphene by monitoring Raman band shifts under stress. In fact, such an approach has been successfully applied to carbon fibres [31], carbon nanotubes [32] as well as graphene. It was noted that, when graphene deformed [33–47], the 2D Raman bands will shift along with the strain as shown in Figure 2.4. Gong et al. [42] calculated the Young's modulus as 1200 ± 100 GPa for a graphene monolayer, which is very close to the results measured through direct tensile or bend testing.

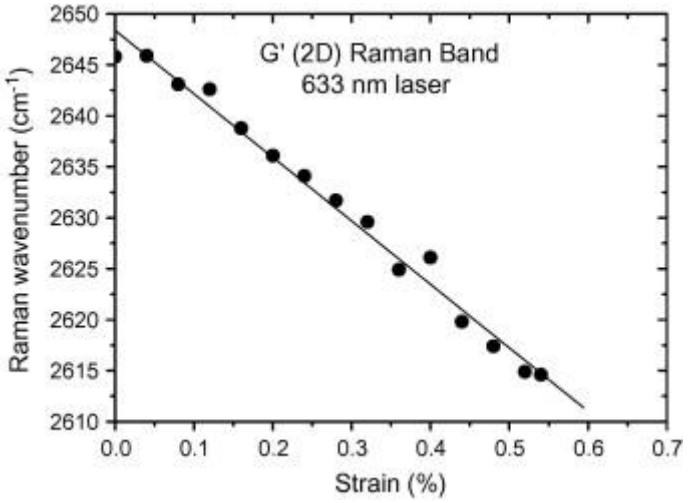

Figure 2.4. Relationship between Raman 2D band wavenumber and strain for single layer graphene sheet. Reproduced from [42].

The fracture toughness of a material is more important than strength in engineering applications. Zhang et al. [48] measured the fracture toughness of graphene in a scanning electron microscope (SEM) by in-situ tensile tests as shown in Figure 2.5 and a critical stress intensity factor of 4 MPa$\sqrt{m}$ was reported. This a low value compared with that of metallic materials (15-50 MPa $\sqrt{m}$), indicating that graphene under strain will exhibit a brittle behaviour when breaking.

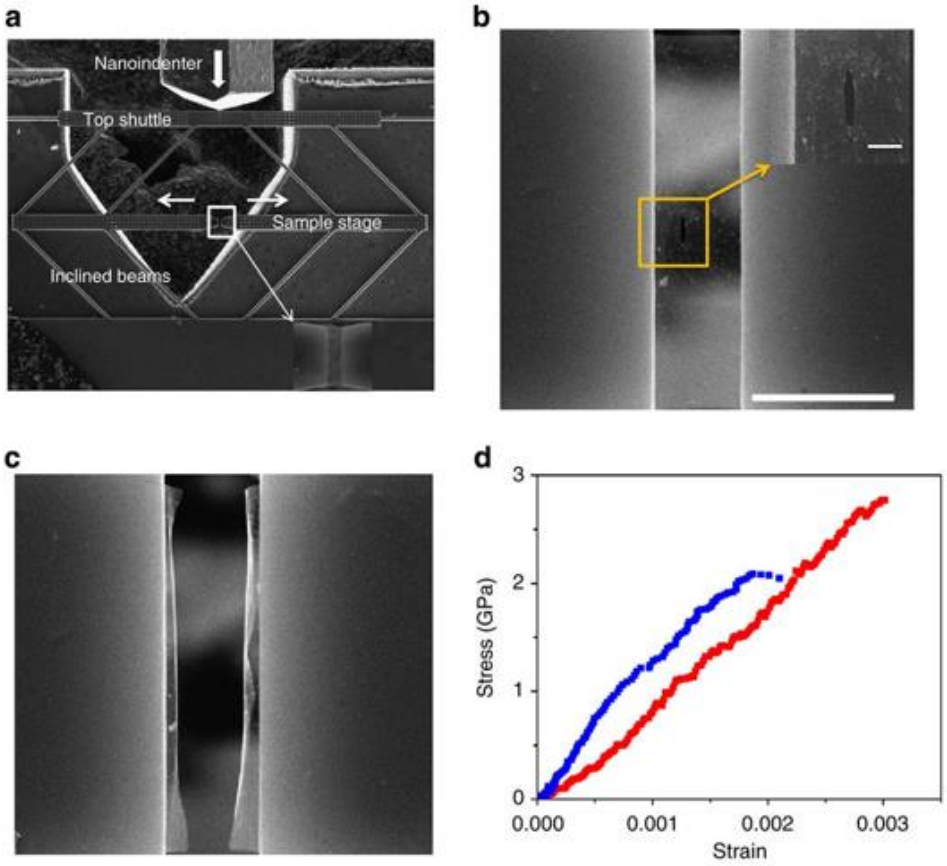

Figure 2.5. (a) Set-up for measuring the mechanical properties of graphene in a SEM. (b) graphene samples before test in the SEM. (c) graphene samples after test in the SEM. (d) Typical stress-strain curves for graphene taken to break. Reproduced from [48].

2.2.2 Electrical properties

The electrical conductivity of graphene has been widely measured in the literature [49–54]. The conductivity of graphene is reported to be ~10^8 S/cm for single layer and decreases to ~10^6 S/cm for few layers. The conductivity is reported to decrease when the number of graphene layers increases, and will eventually reach that of the bulk graphite (~10^5 S/cm) [49,50].

2.2.3 Characterization of graphene

Atomic force microscopy (AFM) can determine the thickness of graphene. For example, Novoselov et al. [55] used to characterise graphene as shown in Figure 2.6 (left) and reported a thickness of 0.4 nm, while 0.335 nm is considered as the average interlayer spacing between graphene layers. Apart from thickness, AFM can be used for the imaging of different morphologies including folds [56] and wrinkles [57,58] on the graphene surface.

Scanning electron microscopy (SEM) can give qualitative information regarding the diameters as well as 3D morphology of graphene particles [20]. For example, McAllister et al [20] observed an agglomerated functionalized single graphene sheets (FGSs) powder with a "fluffy" appearance as shown in Figure 2.6 (right).

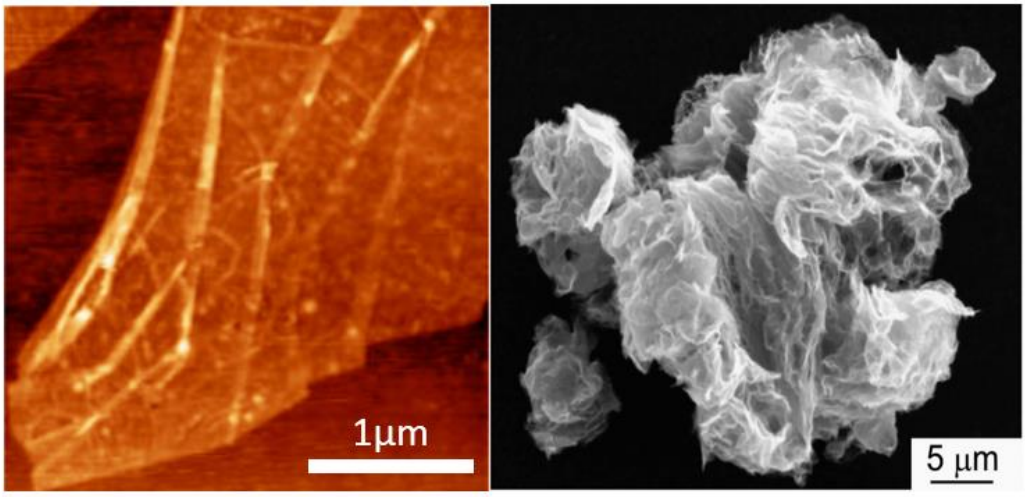

Figure 2.6. Single-layer graphene visualized by AFM (left), Reproduced from [55] and SEM image of dry, as-produced agglomerated FGS powder (right), Reproduced from[20].

X-ray diffraction is another useful tool to identify single or few-layer graphene as shown in Figure 2.7. Typically, graphite exhibited a peak (002) Bragg reflection at 2θ=26° and the number of layers can be estimated using the Scherrer equation as reported in several studies [59,60].

Raman spectroscopy has played crucial role in the characterization of graphene structure. For single layer graphene, a typical G band usually appears at 1582 cm^{-1} and a 2D band usually

peaks at about 2700 cm^{-1} as shown in Figure 2.8. When there is a disordered graphene sample, a D band originates from disorders will also show at ~ 1350 cm^{-1}. Monolayer graphene, bilayer graphene as well as few layer graphene showed difference characteristics under Raman as shown in Figure 2.9. For single layer graphene, its 2D band intensity is nearly twice of that of its G band, yet for bilayers and multilayers, the 2D band is weaker than the G band.

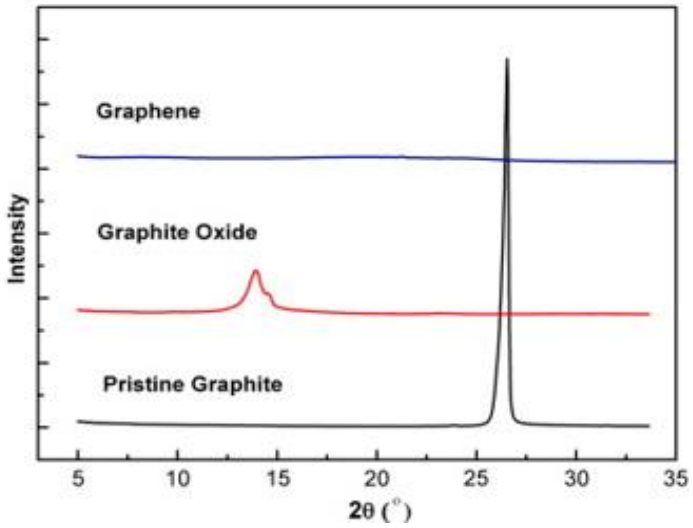

Figure 2.7. Comparison between graphene, graphite oxide and pristine graphite through XRD. Reproduced from [61].

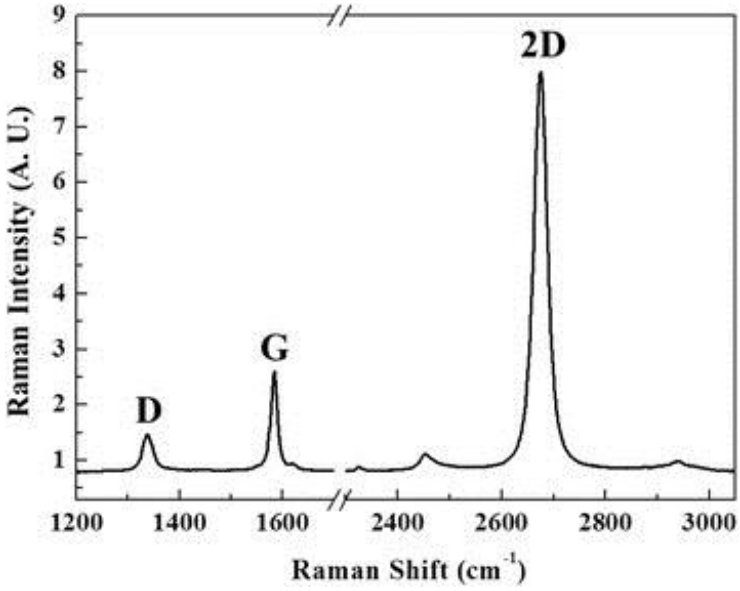

Figure 2.8. Raman spectrum for monolayer graphene. Reproduced from [62].

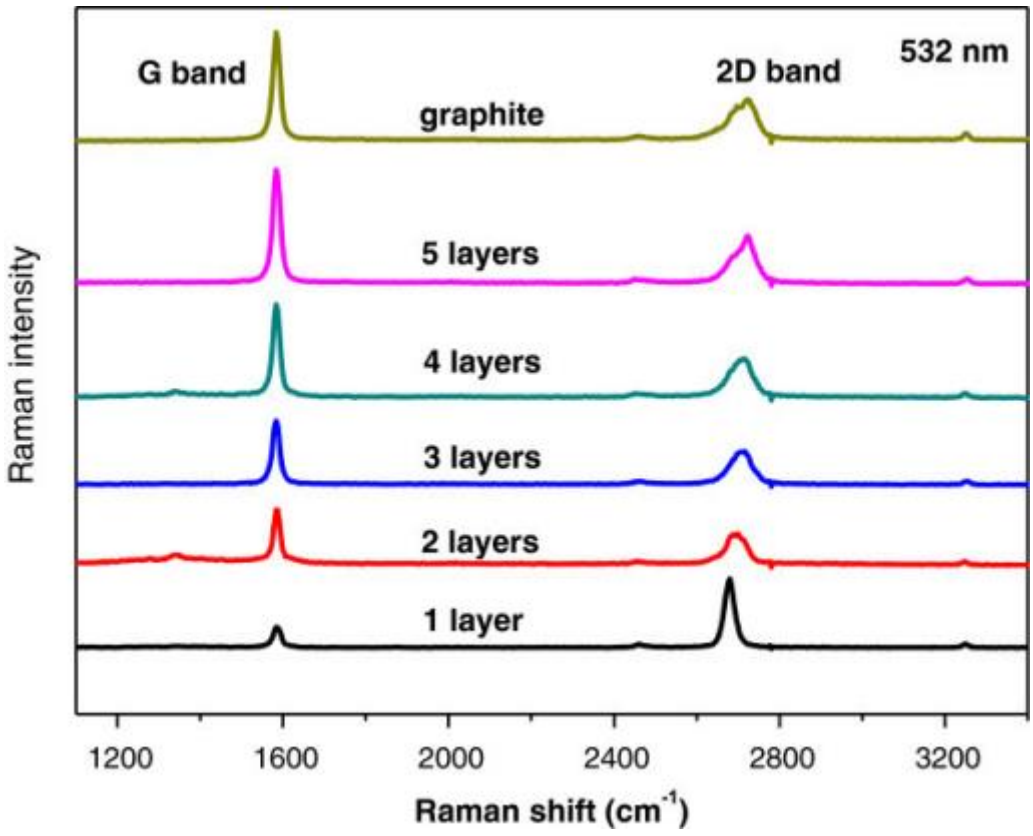

Figure 2.9. Comparison between Raman spectra for single layer, two layer, multilayer graphene and graphite samples. Reproduced from [63].

2.3 Properties of polymer/graphene nanocomposites

2.3.1 Mechanical properties of polymer/GNP composites

The mechanical properties of polymer/GNP composites are affected by many factors, including filler-matrix stress transfer as well as filler properties.

Stress transfer

Stress transfer is of critical importance in the realm of nanocomposites. The classic shear-lag theory developed by Cox [64] was widely used to describe the reinforcing effect for composites filled with platelets , including bone [65], shells [66], clays [67] and graphene [4].

Sandwiching single layer graphene between polymer layers as shown in Figure 2.10, the strain across the single layer graphene, e_f, can be expressed using shear-lag analysis as:

$$e_f = e_m \left[1 - \frac{\cosh(ns\frac{x}{l})}{\cosh(ns/2)} \right] \quad (2.1)$$

Where e_m is the strain and parameter n is given by:

$$n = \sqrt{\frac{2G_m}{E_g}\left(\frac{t}{T}\right)} \quad (2.2)$$

Where G_m is the shear modulus of polymer matrix, E_g is the Young's modulus of single layer graphene, l is the length of the single layer graphene along the x axis, t is the graphene thickness, s is the aspect ratio of the graphene along the x axis and T is the thickness of the composite. n is a parameter reflecting the effectiveness of the interfacial stress transfer [68].

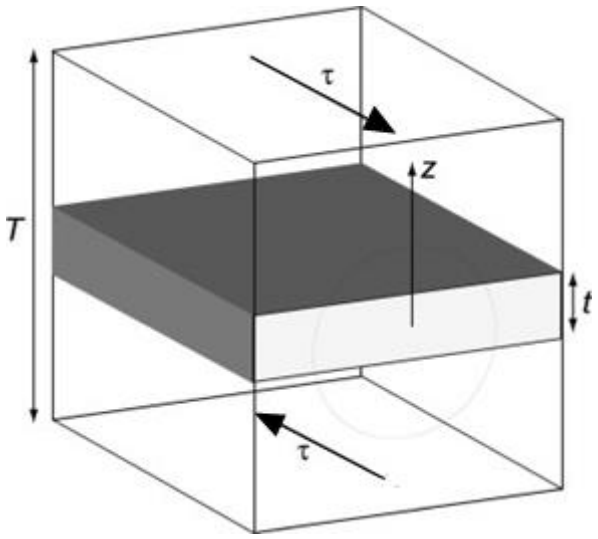

Figure 2.10. Shear-lag model for monolayer graphene confined in polymer matrix. τ is the shear stress at a distance z from the centre of the monolayer. T is the thickness of the composite, t is the thickness of single layer graphene.

In addition, the shear stress, τ_i, at the polymer-filler interface is presented as [42] :

$$\tau_i = nE_g e_m \frac{\sinh\left(ns\frac{x}{l}\right)}{\cosh(ns/2)} \quad (2.3)$$

In order to achieve the best platelet reinforcement, a high value of ns is desired according to Equation (2.2) and (2.3).

Critical length

In order to assess the reinforcing potential of fibres and platelets, the 'critical length' (L_c) concept was introduced for composites. This parameter is determined as double the minimum length over which the stress runs from zero at the filler end to reach the failure stress of the filler in the mid-session. Gong et al.[42] evaluated the degree of attachment between PMMA matrix and monolayer graphene through strain-dependent Raman band shifts and reported the critical length for graphene to be in the order of 3 µm as shown in Figure 2.11. It is commonly accepted that the filler length need to reach 10-times L_c for optimal reinforcement. Therefore, large graphene flakes with diameters greater than 30 µm are required for effective mechanical reinforcement.

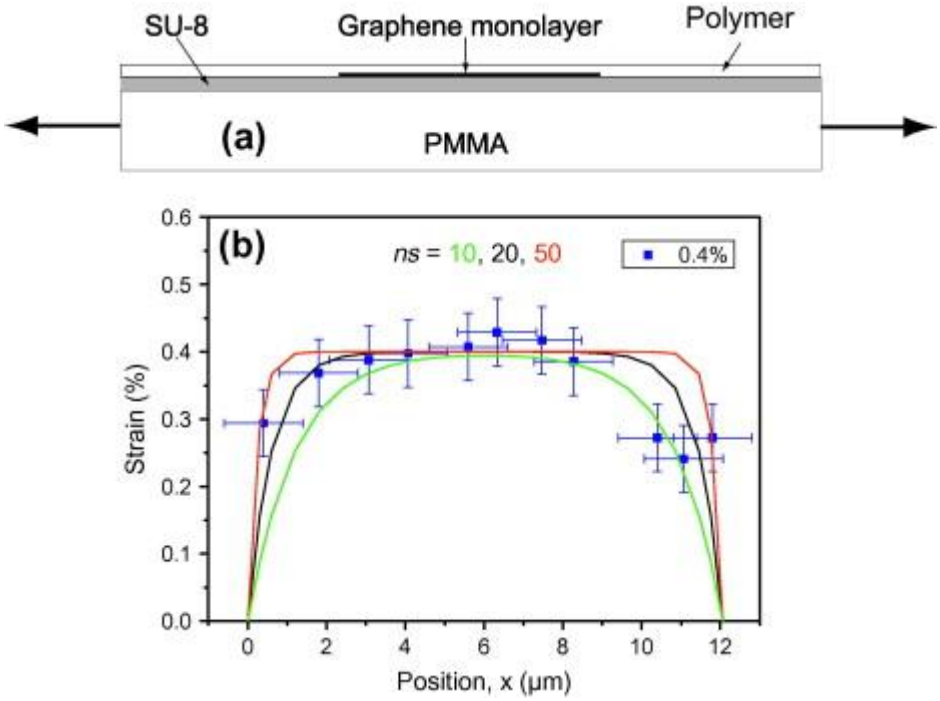

Figure 2.11. (a) Illustration of PMMA/graphene composite containing single layer graphene. (b) Strain distribution as a function of position x along the the tensile axis on the graphene with strain fixed at 0.4%. ns values of 10, 20, 50 are used. Reproduced from [42].

Bilayer, trilayer and multilayer graphene

Poor stress transfer of graphite is usually a result of layer sliding. This observation applies to multilayer graphene as well. In the coated state, when polymer is in contact with the top and bottom surfaces of the multilayer graphene flake, Gong et al. [69] argued that, for multilayer graphene, the effective Young's modulus (E_{eff}) can be expressed as:

$$\mathrm{E}_{eff} = \frac{\mathrm{E}_g}{\frac{\mathrm{n}}{2} - \mathrm{k}\left(\frac{\mathrm{n}}{2} - 1\right)} \ (\mathrm{n} > 2) \tag{2.4}$$

where n is the number of graphene layers, E_g is the Young's modulus of monolayer graphene, parameter k is the stress transfer efficiency factor, taken as 0.6 according to Gone et al. [69]. The relationship between E_{eff} and the number of layer that follows Equation (2.4) is shown in Figure 2.12. The effective graphene Young's modulus remains the same for single layer and double layers and started decreasing with increasing number of layers.

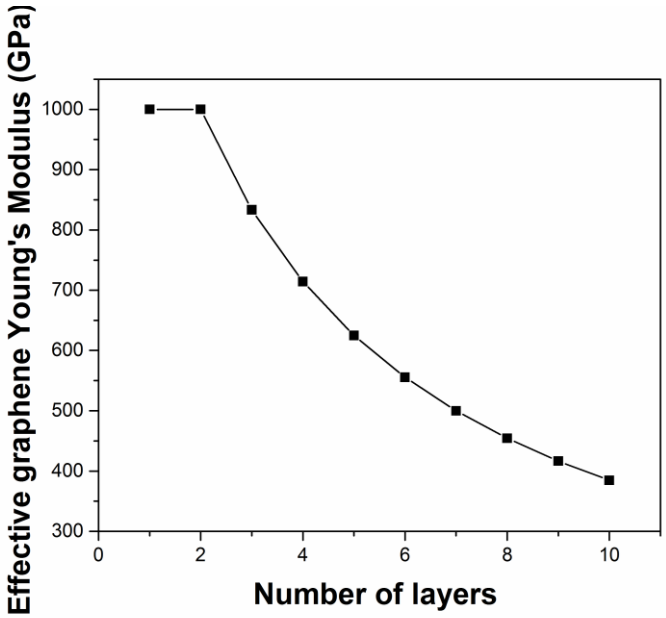

Figure 2.12. Relationship between effective Young's modulus and the number of graphene layers. Reproduced from [69].

Bulk nanocomposites

When graphene is incorporated in the polymer matrix, the rule of mixtures (ROM) is usually applied to anticipate the Young's modulus (upper bound) E_c of composites:

$$E_c = E_p V_p + E_m(1 - V_p) \tag{2.5}$$

Or when we consider the effective reinforcement:

$$\frac{E_c}{E_m} = V_p \frac{E_p}{E_m} + V_m \tag{2.6}$$

where E_p is the Young's modulus of the filler, E_m is the Young's modulus of the polymer matrix and V_p is the volume portion of fillers and $V_p + V_m = 1$.

When there is uniform stress, the Young's modulus (lower bound) is expressed as:

$$\frac{1}{E_c} = \frac{V_p}{E_p} + \frac{V_m}{E_m} \tag{2.7}$$

Or when we consider the effective reinforcement:

$$\frac{E_c}{E_m} = \frac{E_p}{V_m E_p + V_p E_m} \tag{2.8}$$

For many years researchers have attempted to develop more accurate models for predicting the Young's modulus of composites [70–73]. Halpin and Tsai [70] established a new model for the prediction using ribbon-shaped fillers. When graphene particles are aligned in the polymer matrix, the effective reinforcement is considered as:

$$\frac{E_c}{E_m} = \frac{1 + \xi \eta V_p}{1 - \eta V_p} \tag{2.9}$$

Here η is expressed as:

$$\eta = \frac{\frac{E_p}{E_m} - 1}{\frac{E_p}{E_m} + \xi} \tag{2.10}$$

In Equation (2.10), the parameter ξ is linked to the filler aspect ratio and is stated as *2l/t* [69]. This model has been successfully applied in numerous research studies of graphene/polymer nanocomposites.

According to Equation (2.9), it is expected that the Young's modulus increases with increased filler loading and higher aspect ratio, which is often also found in experiments [74].

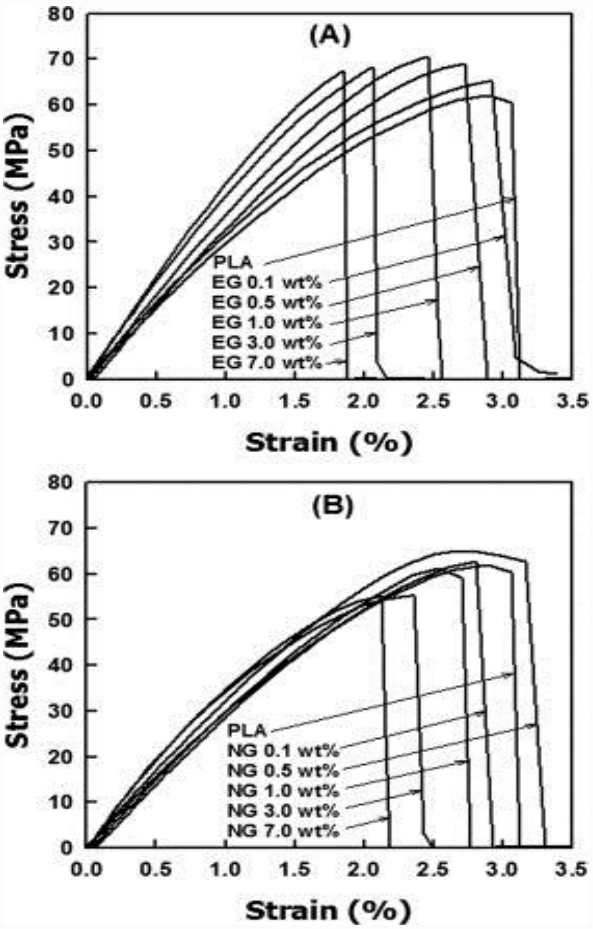

Figure 2.13. Stress–strain relationship for PLA/EG (A) and PLA/NG (B) composite films as a function of filler loading. Reproduced from [73].

While predicting Young's modulus for polymer composites is relatively straight forward using models such as the Halpin-Tsai model, other mechanical properties like tensile strength,

toughness etc. are far more complicated to predict as they are controlled by many more factors, including the status of dispersion, interfacial bonding and failure modes. These aspects lead to mechanical properties with different concentration dependencies. Mechanical properties of typical polymer/graphene nanocomposites are presented in Table 2.1.

*Table 2.1. Mechanical properties of graphene or graphene-based polymer nanocomposites. * S=Solution mixing, M=Melt mixing, P= In-situ polymerization, SSSP= solid-state shear pulverization.*

Polymer	Filler	Mixing method*	Filler loading	% increase Young's modulus	% increase tensile strength	% increase flexural strength	Ref
PMMA	EG	S	21 wt%	21	-	-	[75]
	GNP	S	5.0 wt%	133	-	-	[76]
PP	EG	M	3.0 vol%	-	-	8	[5]
	xGNP-1	M	3.0 vol%	-	-	26	[77]
	xGNP-15	M	3.0 vol%	-	-	8	[77]
	Graphite	SSSP	2.5 vol%	-	60	-	[78]
LLDPE	xGNP	S	15 wt%	-	200	-	[79]
HDPE	EG	M	3.0 wt%	100	4.0	-	[80]
	UG	M	3.0 wt%	33	-	-	[80]
PPS	EG	M	4.0 wt%	-	-	−20	[81]
	S-EG	M	4.0 wt%	-	-	−33	[81]
PVA	GO	S	0.7 wt%	-	76	-	[82]
	Graphene	S	1.8 vol%	-	150	-	[83]
TPU	Graphene	S	5.1 vol%	200	-	-	[84]
PET	EG	P	5.0 wt%	39	-	-	[85]
		P	10 wt%	42	-	-	[10]

In terms of strength (tensile, compression, flexural) and elastic modulus, three categories of strengthening results are reported: (1) strength decreases with increasing loading [13,86–

92,92,93]; (2) strength increases with increasing loading [13,93]; (3) strength increases to a maximum value at a certain loading, and then decreases with additional graphene [74,95–97]. The last phenomenon is usually a result of agglomeration at higher GNP concentrations (greater than 5 wt% as in most literature), which results in stress concentration sites and weak interfaces.

While some success has been reported for improving the elastic modulus as well as tensile strength with the addition of graphene, very little success have been reported in terms of improved toughness. So far, few studies have managed to improve the impact toughness of polymer/graphene nanocomposites [96,98–101]. In fact, more studies reported a reduction of impact toughness with addition of graphene [78,79,91,94,102]. More specifically, even in the case that toughness improved with increasing filler loading, the highest toughness values for composites were still below that of the pure polymer [79]. Similarly, the strain at break, which is indication of ductility, often decreases with further loading of graphene or GNPs to polymer matrices [74,79,86,101].

2.3.2 Electrical properties of polymer/GNP composites

Many studies [75,103–109] have shown that polymers can be transformed from an insulator to a conductor with the addition of graphene (Figure 2.13). Such transitions are usually explained by the percolation theory using a power law equation [110]:

$$\sigma = \sigma_0 \, (V_f - V_c)^s \tag{2.11}$$

where σ is the bulk composites conductivity, σ_0 is the effective conductivity of the filler, V_f is the volume fraction of the filler, V_c is the critical filler volume fraction at the percolation threshold and parameter s is the critical exponent. The value of s is a variable depending on the filler orientation, filler shape and particle dispersion. s and V_c are usually obtained by fitting experimental data ($\log \sigma$~$\log(V_f - V)_c$) as shown in the inserted graph in Figure 2.14. Alternatively, the electrical percolation can be taken as the concentration where its resistance decreases to 10% of that of neat polymer following work by Kim and Macosko [111]. It is

usually reported that $s \approx 1.2$ for a 2D particle (in-plane) distribution [112,113] and $s \approx 1.8$ for a 3D (random) distribution [110,114,115]. Nevertheless, higher values can be frequently found in the literature.

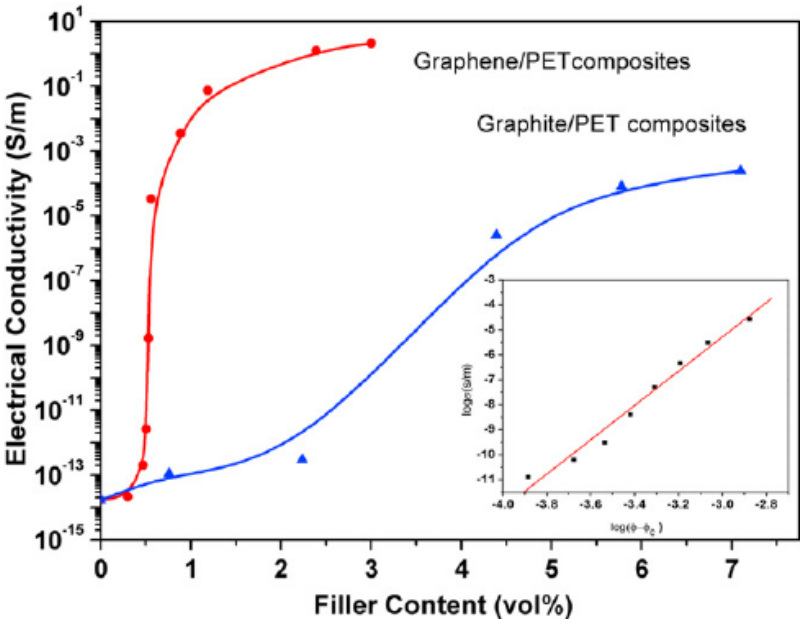

Figure 2.14. Relationship between electrical conductivity and filler volume fraction for PET/graphene nanocomposites (red) and PET/graphite composites (blue). Reproduced from [61].

In the case of GNPs, Li and Kim established the percolation threshold as [116]:

$$\varphi_{f\_2D} = \frac{2\pi D^2 t}{(D + D_{IP})^3} \tag{2.12}$$

$$\varphi_{f\_3D} = \frac{27\pi D^2 t}{4\,(D + D_{IP})^3} \tag{2.13}$$

where φ_{f_2D} and φ_{f_3D} are the percolation thresholds for composites with 2D and 3D randomly oriented fillers, D is the length of filler, t is the thickness of filler and D_{IP} is the inter-particle distance.

The classic quantum-mechanical tunnelling theory [117] reported that, when the DIP is close to 10 nm, electron hopping will happen and result in rapidly increased electrical conductivity of composite. Using DIP = 10 nm, Li et al. [116] revealed the relationship between percolation threshold and aspect ratio of GNP using Equation (2.12) and (2.13) and compared them with models by Celzard et al. [118] and Lu et al. [119]. A good fit of model prediction with experiment data was achieved as shown in Figure 2.15.

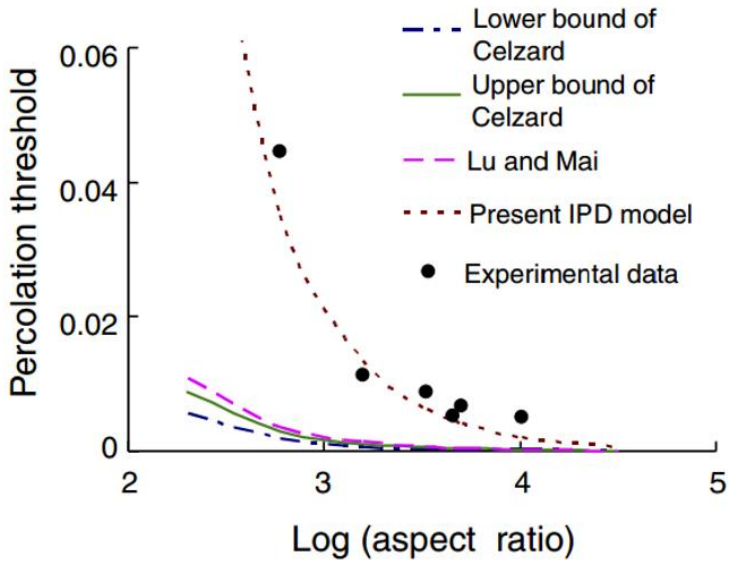

Figure 2.15. Percolation threshold as a function of filler aspect ratio. Reproduced from [116].

Typical electrical properties of polymer/graphene composites are presented in Table 2.2. As expected, a higher percolation threshold is observed for polymer/GNP composites fabricated by melt compounding. Nevertheless, the plateau values of electrical conductivity show little difference regardless of the production method. Most electrical properties of polymer/GNP nanocomposites exhibit plateau values around 10^{-4} to 10^{-3} S/cm. However, polymer composites based on carbon nanotube (CNT) usually exhibit a considerably lower percolation thresholds (~0.1 vol %) [120] than those based on GNP.

*Table 2.2. Electrical properties of polymer/GNP nanocomposites. * S=Solution mixing, M=Melt mixing, P= In-situ polymerization.*

Polymer	**Mixing method***	**Percolation threshold**	**Electrical conductivity (S/cm)**	**Ref**
PP	M	0.1 vol%	~10^{-4} @ 3.0 vol%	[5]
HDPE	M	2.5 vol%	~10^{-6} @ 8.0 wt%	[96]
HDPE	M	16 wt%	~10^{-4} @ 25 wt%	[94]
HDPE	M	5.7 wt%	~10^{-4} @ 8.0 wt%	[121]
PVDF	S	2.4 wt%	~10^{-4} @ 4.0 wt%	[122]
PVA	S	6.0 wt%	~10^{-7} @ 7.0 wt%	[97]
CMPVA	S	0.8 wt%	~10^{-6} @ 4.0 wt%	[123]
PMMA	S	N/A	~10^{-4} @ 5.0 wt%	[76]
PMMA	P	2.0 wt%	~10^{-4} @8.0 wt%	[124]
LLDPE	S+M	12–15 wt%	~10^{-7} @ 20 wt%	[79]
PLA	M	3–5 wt%	~10^{-7} @ 7.0 wt%	[74]
PAN	S	3–4 wt%	~10^{-3} @ 6.0 wt%	[125]
PEN	M	0.3 vol%	–	[126]
Nylon-6	P	0.75 vol%	~10^{-3} @ 3.0 wt%	[127]
PODBS	P	4.0 wt%	~10^{-3} @ 5.0 wt%	[128]
Silicone rubber	S	0.9 vol%	~10^{-5} @ 2.0 vol%	[86]
PET/GNP	M	5.7 wt%	~10^{-1} @10 wt%	[109]

2.3.3 Barrier properties of polymer/GNP composites

Graphene is usually regarded as a potential material for barrier films. For example, the addition of an extremely low amount (0.02 vol%) of crumpled graphene greatly improved the barrier properties of the resulting composites as illustrated in Figure 2.16 [129].

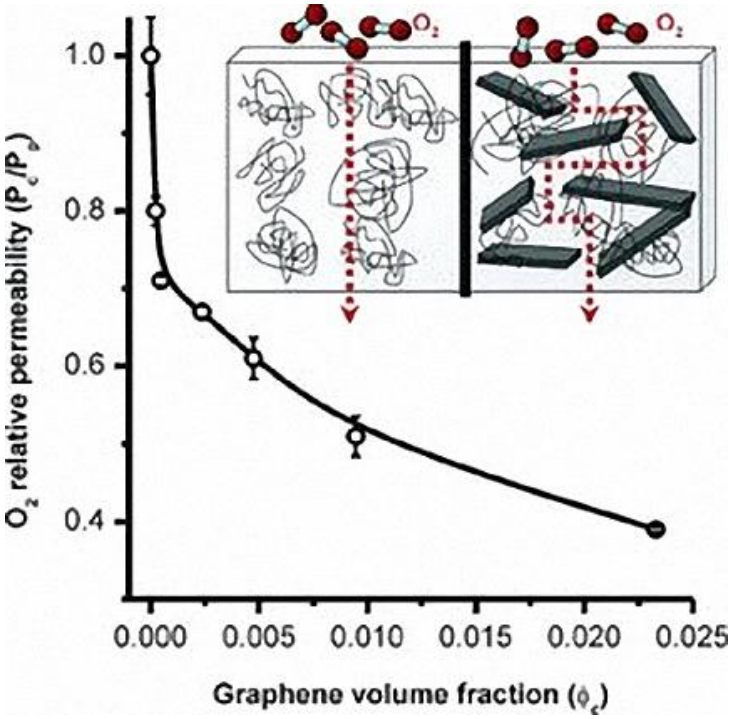

Figure 2.16. Relationship between Oxygen relative permeability and graphene volume fraction in polystyrene (PS)/graphene composites. [129].

In 1976, Nielsen developed the 'tortuous path' model to model the barrier properties of filled polymer system (Figure 2.17.), stating that the path that water or gas molecules must take to pass through the polymer is increased with the addition of a high aspect ratio filler.

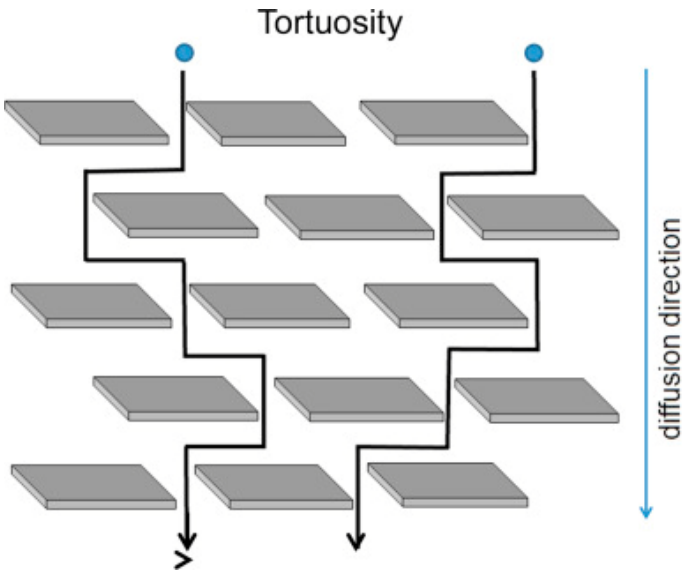

Figure 2.17. Illustration of the Nielsen model. Reproduced from [130].

Nielsen [131] also developed the following equation:

$$\frac{P}{P_0} = \frac{1-\varphi}{1+(\frac{D}{2t}).\varphi} \tag{2.14}$$

Where P and P_0 are the permeability of the polymer composites and neat polymer matrix, D is the filler diameter, t is the filler thickness and φ is the filler volume fractions.

The Nielsen model has been widely adopted for polymer/clay composite. For instance, Duan et al. [132] showed that a good fit was found for predicting the water vapour transmission rates (WVTR) of PLA/MNT films to the Nielsen model (Figure 2.18).

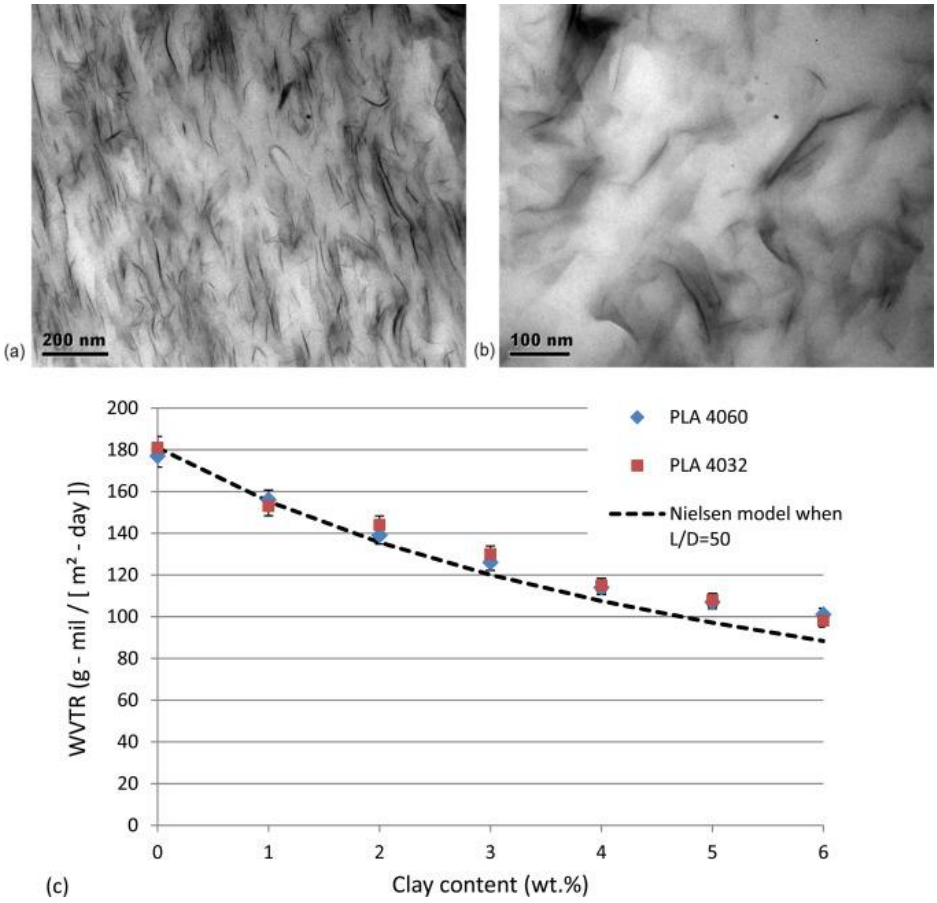

Figure 2.18. (a) Polylactide (PLA)/Clay nanocomposite under TEM with aligned platelets; (b) Polylactide (PLA)/Clay nanocomposite under TEM with randomized platelets; (c) Relationship between WVTR of PLA nanocomposites and clay content, compared with the Nielsen model. Reproduced from [130].

Typical results on barrier properties of polymer/graphene composites are summarised in Table 2.3.

Table 2.3. Summary of results on water permeability of graphene based nanocomposites. S=Solution mixing, M=Melt mixing, P= In-situ polymerization.

Polymer	Filler	Mixing method*	Max. reduction in permeability	Ref
PA12	FGS	M	37% @ 0.6 wt%	[133]
PI	GO	S	90% @ 0.001 wt%	[134]
PI	Graphene	S	93% @ 0.1 wt%	[135]
PI	GO	S	82% @ 0.1 wt%	[135]
PI	GO	S	89% @ 1.0 wt%	[136]
PANI	Graphene	S	88% @ 0.5 wt%	[137]
PU	GO	S	76% @ 3.0 wt%	[138]
EVOH	Graphite	S	59% @ 1.0 wt%	[139]
PVA	GO	S	68% @ 0.72 vol%	[140]
PVA	GO	S	20% @ 2.0 wt%	[141]
CA	GO	S	47% @ 0.8 wt%	[142]
PU	GO	S	76% @ 3.0 wt%	[138]
PVA	GO	S	68% @ 0.72 vol%	[140]

Based on Table 2.3, it seems that significantly improved barrier properties can be achieved with a low graphene loading, as compared to nanoclay based systems. For example, for traditional polyimide/MNT nanocomposites, 8 wt% nanoclay was required to reach a reduction in WVTR of 83% [143]. However, Tseng et al.[134] found that an extremely low GO content of 0.001 wt% achieved a similar reduction.

2.3.4 Synergy with other carbon/non-carbon nanofillers

Polymer composites containing more than one filler often display superior properties [115,144,145] compared to composites filled only with a single nanofiller type as summarized in Table 2.4. Among these hybrid systems, GNP/CNT seems to be the most common binary system and compositions with higher GNP loadings usually achieve optimum increased

properties. For example, epoxy resins with GNP and SWCNT in a 3:1 weight ratio exhibited a greater thermal conductivity compared to those based on an individual filler, yet decreased electrical conductivity as shown in Figure 2.19 [146]. It is believed that the bridging interactions (Figure 2.20) between GNPs and SWCNTs enhanced the interfacial connections for thermal conduction, while eliminating the effective electrical transport.

Table 2.4. Summary of recent researches on polymer nanocomposites with hybrid fillers.

Polymer	Filler	Enhanced property	Ref
PDMS	GNP+CNT	Electrical	[147]
Epoxy	GNP+CNT	Electrical	[146]
Epoxy	GNP+CB+CNT	Electrical	[148]
PVA	ND+CNT+FG	Mechanical	[149]
Epoxy	CNT+GNP	Electrical, Mechanical	[150]
PEI	GNP+CNT	Electrical	[151]
PP	CNT+CB	Electrical	[152]
Epoxy	CNT+silicon gel	Electrical, Rheological	[103]
TPU	CNT+nanoclay	Electrical	[153]

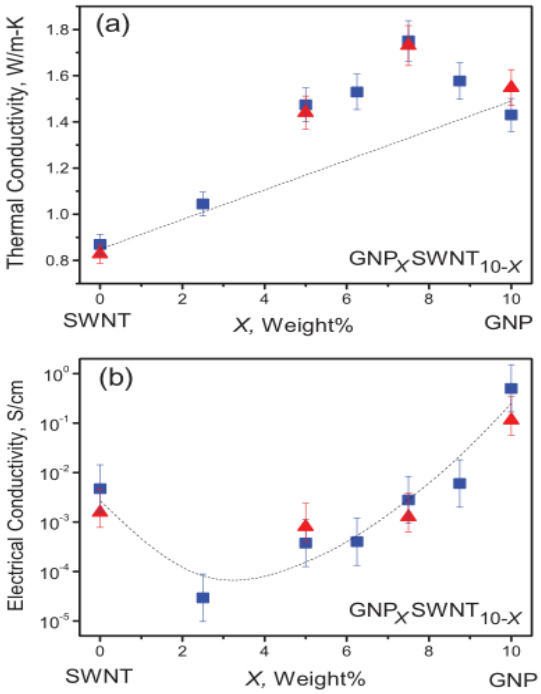

Figure 2.19. Thermal and electrical conductivities as a function of GNP filler percentage (x) for epoxy composites with GNP_xSWNT_{10-x} filler. Reproduced from [146].

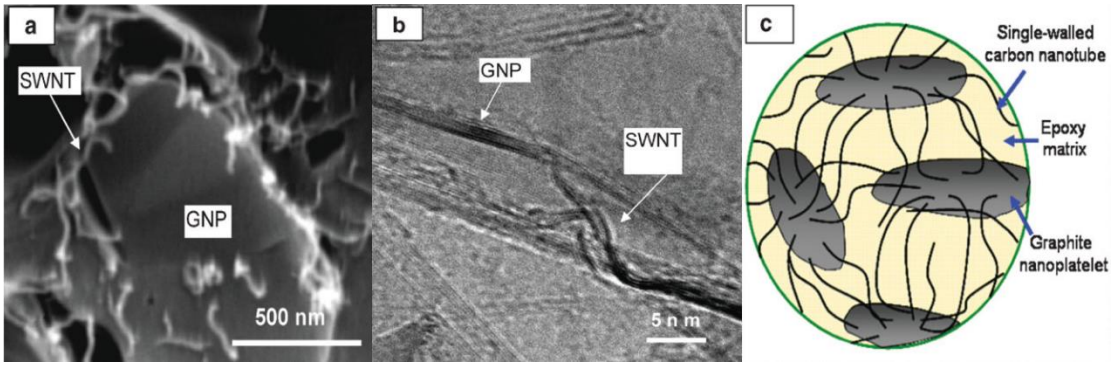

Figure 2.20. (a) SEM and (b) TEM images of epoxy composite with GNP and SWNT. (c) Illustration of typical GNP-SWNT connections. Reproduced from [149].

Apart from improved electrical conductivity, increased mechanical properties have also been reported in a few studies using hybrid fillers. It is reported that both the stiffness and hardness of PVA/CNT/graphene composites increased by four times compared to those with single nanocarbon reinforcement as shown in Figure 2.21 [149].

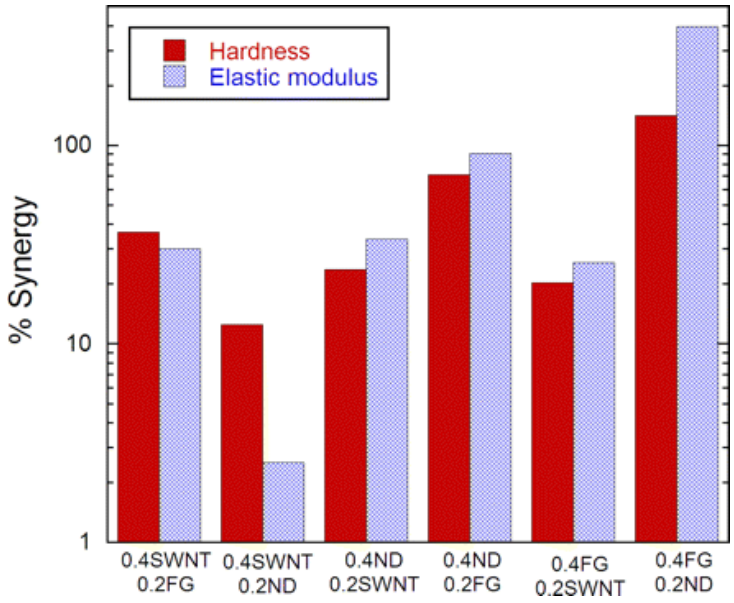

Figure 2.21. Percentage synergy for composites with different filler ratio in terms of hardness and elastic modulus. Reproduced from [149].

Apart from carbon nanofillers, the addition of a secondary non-conductive filler to nanocarbon based conductive polymer composites (CPCs) was also reported to enhance the electrical conductivity of these hybridized nanocomposites through the volume exclusion

effect [115,153–156]. Wilkinson et al. [115] grew nanotubes onto silica gel particles and reported a percolation threshold of 0.62 wt% (equivalent to 0.20 wt% CNTs) for these hybrid particles. This result was second only to the 0.06 wt% reported by Kilbride et al. for CNT/PVOH [157] but much lower than values reported for other hybrid systems (0.675 and 10 wt%, respectively) [158,159]. A subsequent study [103] from the same group showed that such binary systems also have the added benefit of achieving significantly reduced mechanical shear moduli (up to five orders of magnitude) while displaying a very low electrical percolation threshold (~ 0.16 wt% CNT). Bilotti et al. [153] reported controlled dynamic percolation of CNT/TPU composites by adding an insulating nanoclay and found altered percolating networks of CNTs in thermoplastic polyurethane (TPU) explained by the volume exclusion theory [156].

2.4 PLA/graphene composites

2.4.1 Introduction to PLA

With the increasing demand for environmentally friendly materials, polylactide (PLA) has attracted a lot of interest from both industry and academia. PLA possesses several desirable features including biocompatibility, sustainability and biodegradability. In 1954, DuPont firstly patented a PLA with high-molecular weight and started the commercialization of PLA. Over the past 10 years, Nature Works LLC becomes the leading company in the field of PLA markets. Two key types of PLA products developed by them are a) Natureworks™, which are polydilactide-based resins designed for packaging or plastics and b) Ingeo™, which are polydilactide-based fibres that are designed for the application of specialty textiles and fibre.

PLA is a member of aliphatic polyesters and is mainly produced using renewable resources from nature. Lactic acid (CH_3–CHOHCOOH) is the monomer for the building of PLA chains. It has two stereoisomers which are both optically active: dextro- (D -) and levo- (L -) (Figure 2.22). Notably, the two isomers share the same physical properties despite the structure difference.

The major production method to PLA from lactic acid is via the polycondensation reaction, yet organic solvents are required for the extraction of resulting water to get high molecular weight grades. A second route is through the ring-opening polymerization of the monomer as shown in Figure 2.23. Different forms of lactide can be produced as a result as shown in Figure 2.24, namely: L-lactide, D-lactide and meso-lactide. Production through the ring-opening polymerization route enables the tailoring of polymer chains by controlling the ratios between different lactides as shown in Figure 2.25, producing PLAs with different properties, including glass transition temperature, melting temperature, crystallinity and molecular weight. For example, PLA with high percentage of L-lactide usually possess high crystallinity. In fact, it was reported that, by maintaining the D-lactide content below 2%, highly crystalline polymers can was produced [160]. In contrast, amorphous PLAs was achieved when the D-lactide proportion reached higher than 15% [161]. Notably, neat poly-L-lactide (PLLA) is semi- crystalline (37%) [162], while PLA based on meso-lactides is amorphous. In terms of melting temperature, both PLLA and PDLA have a melting point of ~180 °C, yet varying melting point from 130 °C to 220 °C can be achieved depending on the structure of polymer chains [161].

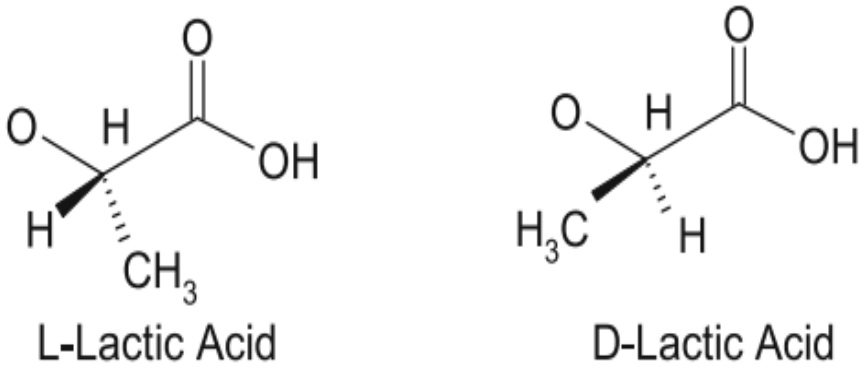

Figure 2.22. L-lactic acid and D-lactic acid. Reproduced from [163].

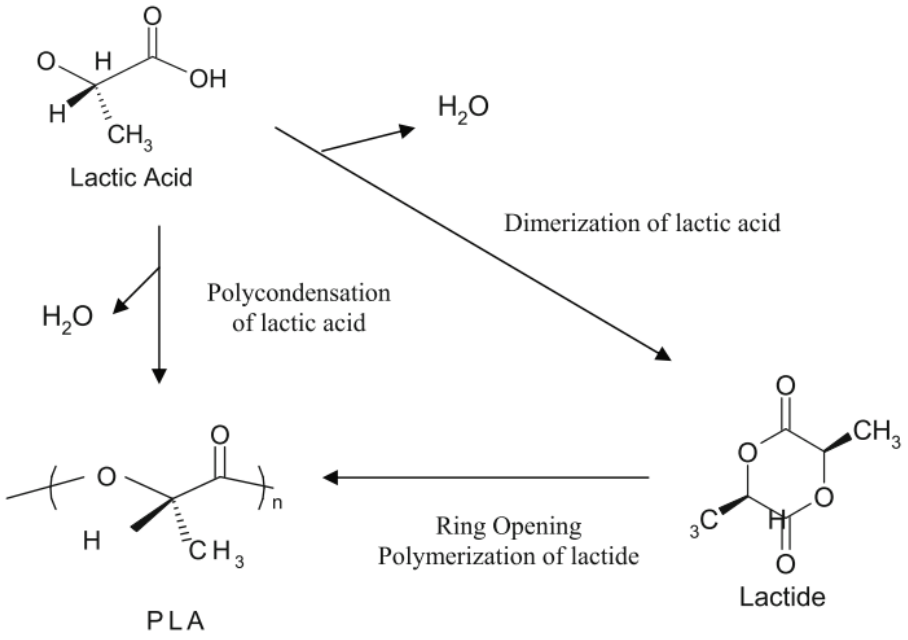

Figure 2.23. Two routes for the production of PLA from Lactic Acid. Reproduced from [163].

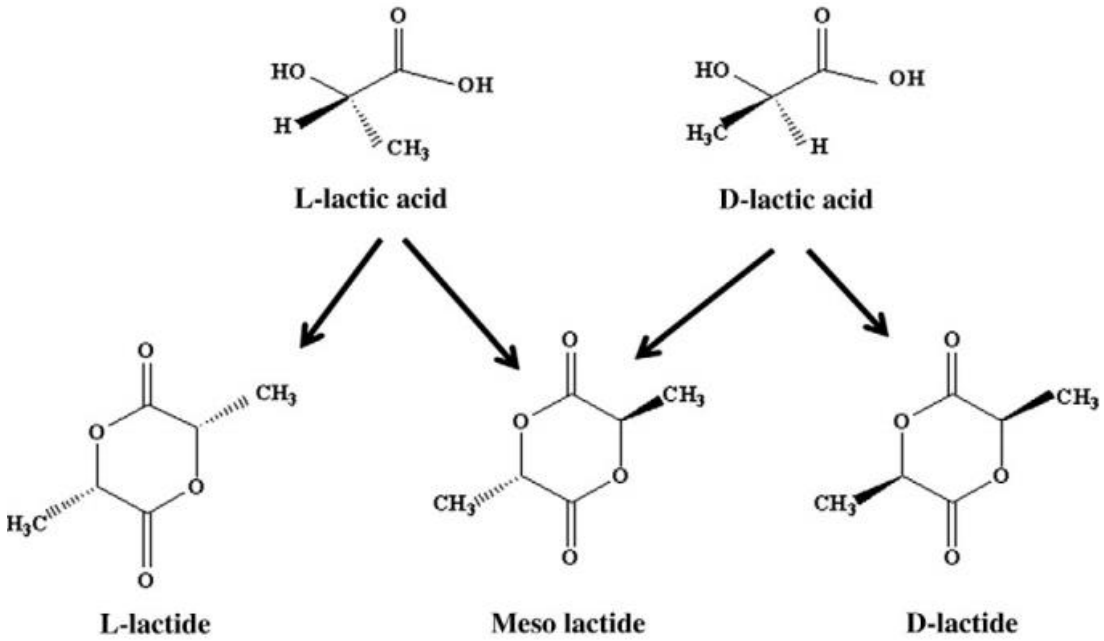

Figure 2.24. Possible forms of lactides. Reproduced from [163].

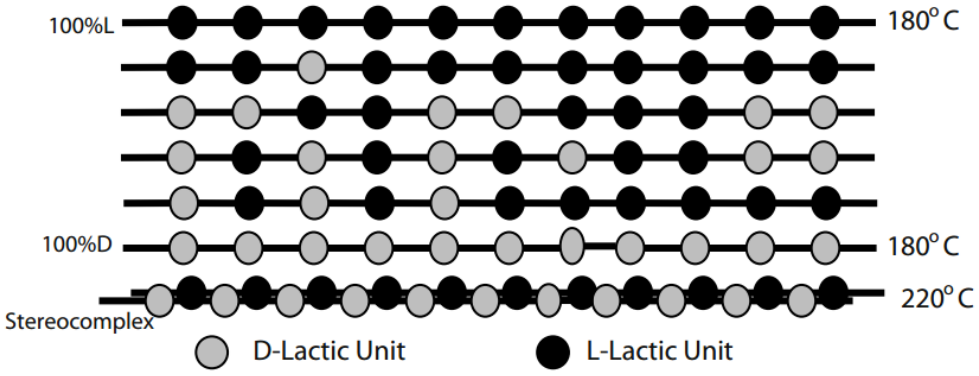

Figure 2.25. Typical PLA chains combining the D-lactic acid and L-lactic acid with varying ratios. Reproduced from [163].

Crystallinity of the PLA have a huge impact on the mechanical and thermal properties and the crystallization process depends on many factors including the thermal processing history [164], addition of additives [165], as well as chain composition [166]. In general, PLA crystals have three structures, named α [167–169], β [170–173], and γ [174] forms. The α-crystal develops upon melt or cold crystallization and is the most occurring and stable polymorph [168]. The β form grows by stretching the α-crystal while the γ form develops on hexamethylbenzene substrate [174]. In addition, the existence of a disorder PLLA form (α'), was confirmed [175–179]. Notably, during the crystallization process of PLLA in the industrial melt processing temperature region of 100-120 °C, both α' and α form crystals is developed [175–178]. It was further noticed that the disordered α' form can reform into the ordered α form upon annealing as shown in Figure 2.26 [180].

The mechanical properties of PLAs can vary from soft materials to stiff plastics. Semi-crystalline PLA usually possesses better mechanical properties compared to amorphous PLA as shown in Table 2.5 [181]. Stereochemistry, processing conditions also have impact on the properties of as shown in Table 2.6 [182]. Compared with other commodity polymers as in Table 2.5 [183], the mechanical properties of semi-crystalline PLLA are promising. Nevertheless, PLA has a low impact strength and slow crystallization rates, both of which limit its industrial applications [184].

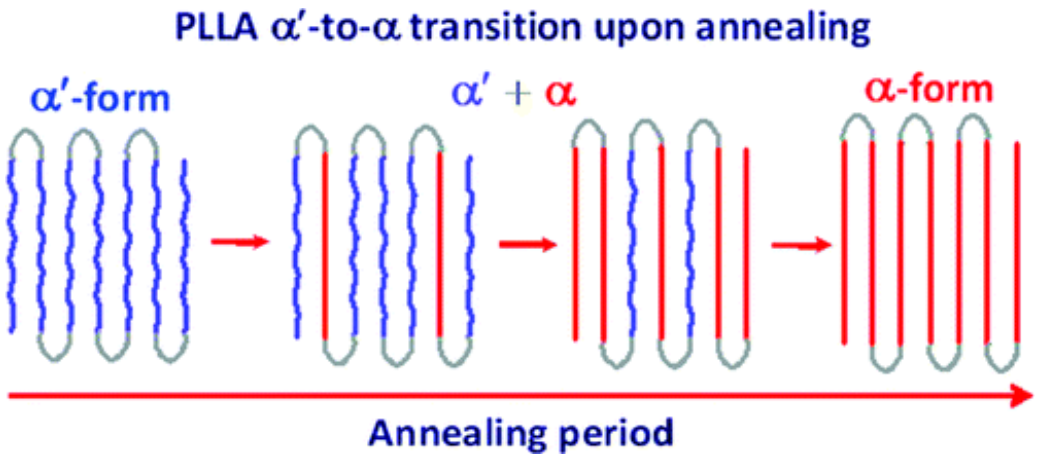

Figure 2.26. PLLA α'-to-α transition upon annealing. Reproduced from [180].

Table 2.5. Summary of the properties of PLA polymers, reproduced from [181].

	PLLA	Annealed PLLA	PDLLA
Crystallinity	3%	45%	amorphous
Tensile strength (MPa)	59	66	44
Elongation at break (%)	7	4	5.4
Modulus of elasticity (MPa)	3750	4150	3900
Yield strength (MPa)	70	70	53
Flexural strength (MPa)	106	119	88
Unnotched izod impact (J/m)	195	350	150
Notched izod impact (J/m)	26	66	18
Rockwell hardness	88	88	76
Heat deflection temperature (°C)	55	61	50

2.4.2 Properties of PLA/GNP composites

Many methods have been proposed [185–190] to reinforce PLA. One solution that has been pursued over the past years is the incorporation of nanofillers into the PLA matrix [189,191,192]. This chapter will review the most recent advances in PLA/graphene nanocomposites.

Mechanical properties of PLA/GNP nanocomposites

Typical effects on mechanical properties for graphene-based PLA composites are presented in Table 2.8. Most studies revealed that the modulus of composites increased with the addition of GNP similar to other polymers [193–197] or decreased after a critical filler loading [198]. The strength of PLA/graphene composites decreased [196] or increased to a maximum value at a specific concentration, and then decreased with additional filler loading [193,197,198], following the general trend of most polymer nanocomposites. With the

addition of graphene, the toughness or the elongation at break of PLA composites usually decreased [193,196], yet unchanged or even improved toughness was also reported [193–195,197,198].

Table 2.6. Summary of the properties of PLA copolymers with different processing condition, reproduced from [182].

Process condition	**Copolymer ratio of (L/D,L)-PLA**	**Tensile strength (MPa)**	**Young's modulus (GPa)**	**Elongation at break (%)**	**Molecular weight (10^3)**
Injection molded, crystallized	100/0	64.8	4	—	800
Injection molded, amorphous	90/10	53.4	1.03	4.6	—
Injection molded, crystallized	90/10	58.6	1.29	5.1	—
Extruded, biaxially oriented, strain crystallized	90/10	80.9	3.41	41.2	145
Extruded, biaxially oriented, strain crystallized, heat set	90/10	70.1	2.76	20.7	145
Extruded, biaxially oriented, strain crystallized	95/5	68.6	1.88	56.7	120
Extruded, biaxially oriented, strain crystallized, heat set	95/5	60.7	1.63	63.8	120
Injection molded, amorphous	80/20	51.7	2.1	5.7	268
Extruded, biaxially oriented, strain crystallized	80/20	84.1	2.94	18.2	268
Extruded, biaxially oriented, strain crystallized, heat set	80/20	80.1	2.54	32.3	268

Table 2.7. Summary of the properties of polymers, reproduced from [183].

Polymer	T_g (°C)	T_m (°C)	Tensile strength (MPa)	Tensile modulus (MPa)	Elongation at break (%)
PLA	40–70	130–180	48–53	3,500	0.5-12
LDPE	-100	98–115	8–20	300–500	100–1,000
PCL	-60	59–64	4–28	390–470	700–1,000
PS	70–115	~100	34–50	2,300–3,300	1.2–2.5
PVA	58–85	180–230	28–46	380–530	–
PET	73–80	245–265	48–72	200–4,100	30–300

Table 2.8. Mechanical properties of PLA/graphene composites by melt mixing. S=Solution mixing, M=Melt mixing.*

Filler	Mixing method*	Filler loading	% increase Young's modulus	% increase tensile strength	Ref
GNP	S	0.4 wt%	156	129	[193]
GO	S	0.5 wt%	–	106	[194]
GNS	S	0.2 wt%	18	26	[195]
PFG	M	5.0 wt%	80	10	[199]
EG	M	2.0 wt%	33	10	[74]
EG	M	4.0 wt%	56	18	[196]
RGO	M	0.3 wt%	–	3.4	[197]
GNP	M	0.3 wt%	–	1.7	[197]
xGNP	M	0.3 wt%	70	-32	[198]
GNP	M	0.1 wt%	-4.0	–	[200]
MWNT	M	0.15 wt%	3.5	–	[200]
TRG	S	1.0 wt%	–	8.5	[201]

Electrical properties of PLA/GNP composites

Typical results for the electrical conductivity of PLA/graphene composites are presented in *Table 2.*9. Most conductive polymer composites (CPCs) showed improved electrical

conductivity with increasing GNP content with the conductivity levelling off at around 10^{-4} to 10^{-3} S/m, regardless of GNP concentration. Typical percolation thresholds ranged from 4 to 13 wt% GNP in PLAs.

Notably, apart from the general factors that influence the electrical conductivity of PLA/graphene composites, the degree of crystallization has an important influence on the conductivity. PLA is a semi-crystalline polymer thus the conductivity of its CPCs is affected by crystallinity. For example, Fang et al. [202] attributed the increase in conductivity to a change in crystallinity for PLA/CNT composites, since the nanotubes were inclined to be concentrated in the amorphous part during blending. Sullivan et al. [203] altered the crystallization characteristics of PLA significantly by varying the cooling rate during compression moulding of films and noticed that, for the same GNP content, the electrical conductivity increased by ~3 orders of magnitude which correlated with an increase of ~40 % in crystallinity.

*Table 2.9. Electrical conductivity of PLA/graphene composites. * S=Solution mixing, M=Melt mixing.*

Filler type	Mixing method*	Percolation threshold	Electrical conductivity (S/m)	Ref
GNP	S	4.5 vol%	0.1 @ 8.4 vol%	[204]
GNP	S	0.1 vol%	0.1 @ 0.1 vol%	[204]
rGO	S	-	10^{-5} @ 2.5 vol%	[205]
rGO	M	0.1 wt%	10^{-9} @ 2.0 wt%	[206]
rGO	S	0.1 wt%	10^{-4} @ 2.0 wt%	[207]
CNT	S	0.8 wt%	10^{-4} @ 2.0 wt%	[207]
EG	M	4.0 wt%	10^{-7} @ 14 wt%	[74]
NG	M	13 wt%	10^{-8} @ 8.0 wt%	[74]

Water barrier properties of PLA/GNP nanocomposites

Research on the permeability of PLA nanocomposites has mainly focused on PLA/nanoclay systems with only few PLA/graphene composites studied so far. An overview of barrier properties of PLA nanocomposites is listed in *Table 2.*10. The maximum reduction in permeability ranges from 1 to 90 %, depending on the loading as well as the type of the filler.

Apart from the filler aspect ratio as discussed in the previous session, the crystallinity of the polymer composites also has an impact on the barrier properties [208].

Table 2.10. Summary of literature on water barrier properties of PLA-based composites (MMT=Montmorillonite, S=Solution mixing, M=Melt mixing, P=In-situ polymerization). Reproduced from [130].

Filler	Mixing method	Maximum % reduction in permeability	Ref
MMT	M	50% @ 5.0 wt%	[209]
MMT	M	92% @10 wt%	[210]
Clay	S	5% @ 5.0 wt%	[211]
Clay	S	36% @ 5.0 wt%	[211]
Clay	M	60% @ 5.0 wt%	[212]
MMT	M	58% @ 5.0 wt%	[213]
Clay	M	95% @15 wt%	[214]
Clay	M	43% @ 6.0 wt%	[132]
Cellulose	S	10% @ 1.0 wt%	[215]
MMT	M	37% @ 5.0 wt%	[216]
Halloysite	M	55% @ 12 wt%	[217]

2.5 Polymer composites by multilayer coextrusion

2.5.1 Introduction to multilayer coextrusion

The forced assembly multilayer coextrusion technology was originally developed nearly five decades ago by Tollar James [218] and involved the use of either two or more extruders to feed material into a feed block followed by one or more multiplier dies as shown in Figure 2.27 [219]. This was a continuous melt-processing method that can have a throughput of 9 kg/hour and is very easy to scale up. In each multiplier die the layered polymer melt is split vertically, compressed and expanded, and then recombined one on top of the other [220,221]. This process is repeated for each multiplier die. If the feed block produces two layers, the final number of layers after n multipliers is 2^{n+1} .This solvent-free process is not only cost-effective and environmentally friendly compared to layer by layer (LBL) deposition technology, but is also able to tune the structure of layered polymeric systems from nano- to micro- scale, which cannot be achieved by traditional polymer blends. With the current state-of-the-art, up to

4,096 layers of thicknesses as thin as 20 nm can be coextruded using 11 units of layer multiplying dies [222].

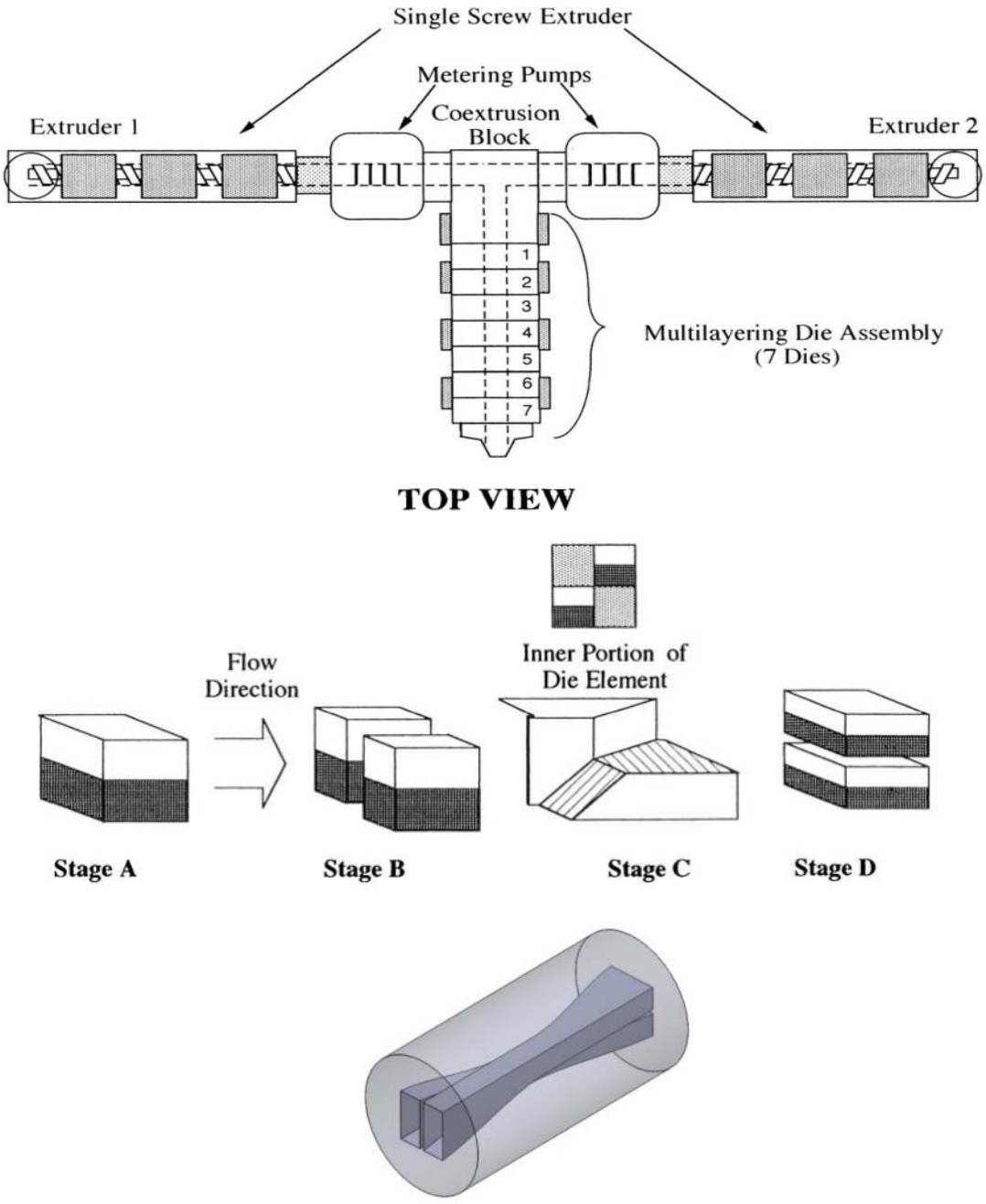

Figure 2.27. Top: Illustration of the production of multi-layered polymer nanocomposite films using 7 dies. Adapted from [219]. Bottom: The standard multiplier die. Adapted from [221]

The following section will provide a comprehensive review of recent advances in multilayer polymer composites with a focus on graphene fillers.

2.5.2 Properties of multilayer coextruded polymer composites

The multilayer coextrusion technique has been used to produce multilayer structures with interesting properties such as increased crystallization [222], barrier properties [223,224],

optical properties [225], electrical conductivity [226–228] and mechanical properties [226,229–239]. By tuning the hierarchical structure and layered configuration, these multilayer films can possess outstanding performances in gas barrier applications and in capacitors and data storage [240–246]. A summary of the most recent research is listed in Table 2.11. Most studies are focused on a PP matrix with a few studies on PE, PMMA with fillers including CB, CNT and GNP etc. Notably, these increased properties are usually linked to: a) increased number of crystals and b) increased filler orientation during the layer multiplying stage and details of the improved properties will be discussed in the next session.

Table 2.11. Summary of studies on multilayer composites.

Layer A	**Layer B**	**Enhanced properties**	**Comments**	**Ref**
HDPE	HDPE+SGF	Mechanical	Increased filler orientation	[237]
LDPE	Mica	Mechanical	Increased alignment & exfoliation	[235]
PEO	EAA	Mechanical	Increased aligned PEO crystals	[229]
PET	PET+talc	Barrier	Increased aligned crystals	[224]
PMMA	PMMA+GNP	Mechanical	Tensile modulus increased 2-fold	[234]
PP	PP+CB	Mechanical, Electrical	Increased elongation at break	[226]
PP	Talc+PP	Mechanical	Increased Young's modulus at the cost of some loss in ductility	[231]
PP	PP+CNT	Mechanical	Increased Young's modulus without significant loss in ductility.	[233]
PP	EVA	Mechanical	Increased crystallinity	[236]
PP	PP+IFR	Flame retardant	Improved flame retardant without loss in mechanical properties	[247]
PP	PEO	Barrier	Decreased permeability from increased crystallinity	[248]
PP+CB+CNT	PP+CB+CNT	Electrical	Lower percolation threshold	[227]
PS	SEPS	Mechanical, Electrical	Improved toughness after annealing	[230]
PS	PMMA	Mechanical	Increased strength and ductility	[234]

Electrical properties

Multilayer extrusion has been successfully applied to tailor the electrical properties of polymer composites. This is usually achieved by the optimization the filler distribution/orientation during the layer multiplying process. Xu et al. [228] used multilayered coextrusion to produce polypropylene (PP) and carbon black (CB) filled PP multilayer composites as shown in Figure 2.28 and proved that multilayer composites can display varied electrical behaviours depending on the number of layers and morphology of the CB particles in the PP+CB layers at identical total CB loading as shown in Figure 2.29.

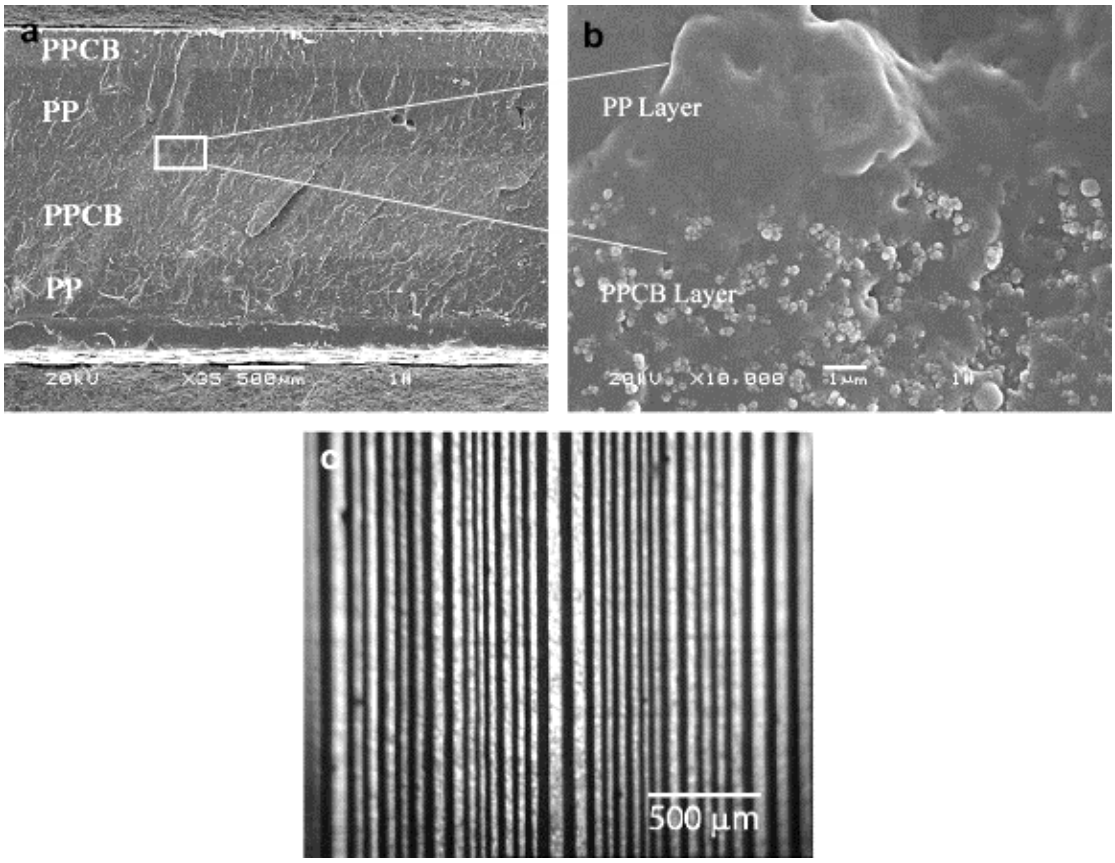

Figure 2.28. (a) PP/PP+CB composites with 4 layers under SEM. (b) Enlarged version of the rectangular area in (a). (c) Polarized light micrograph of composites with 64 layers. Reproduced from [228].

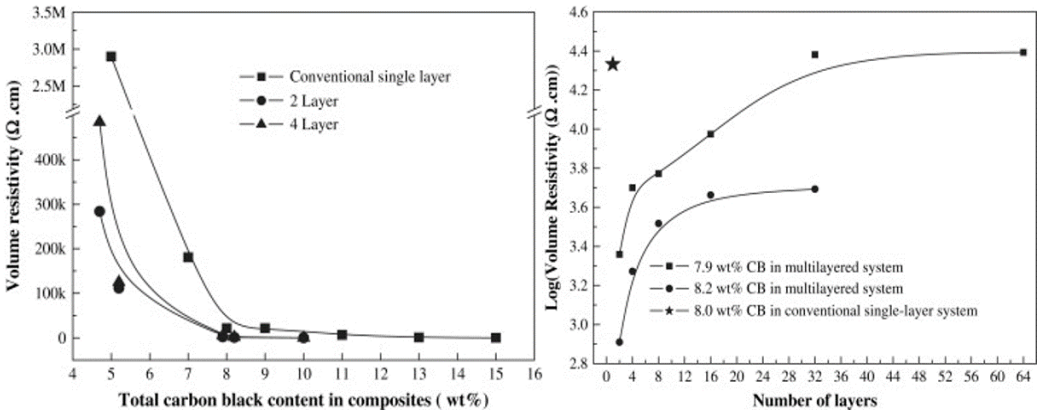

Figure 2.29. Volume resistivity as a function of total carbon black content in composites (left) and number of layers (right). Reproduced from [228].

Mechanical properties

The mechanical properties of multilayer films can also be improved, usually as a result of improved filler distribution and orientation during multilayer coextusion. This technology was used to distribute CNTs in PP by Miquelard-Garnier et al. [233]. The resulting composites containing 0.2 wt% and 1 wt% CNT in PP exhibited an increase of 25–30% in Young's modulus without loss in ductility. Subsequent studies from the same group reported the use of the forced assembly method to orient GNPs in PMMA multilayer films [234]. These films exhibited significant single layer reinforcement of 118% at a concentration of 2 wt% GNP as shown in Figure 2.30, which was higher than previously reported for randomly dispersed GNPs. This increased reinforcing efficiency was explained by the planar orientation of the GNPs in the filled layer.

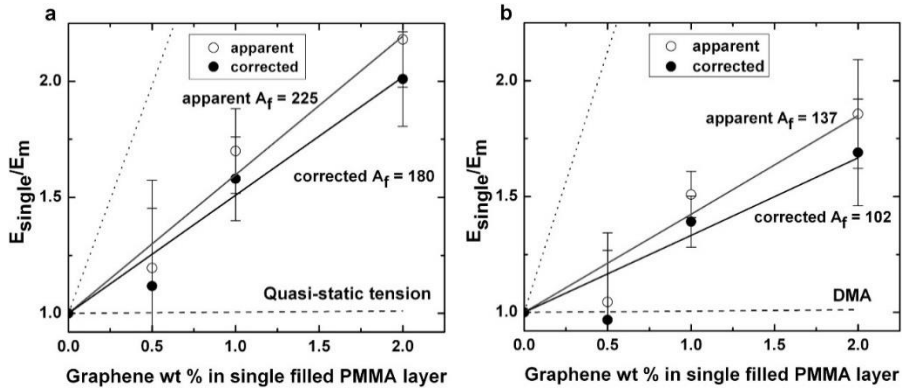

Figure 2.30. Single layer effective reinforcement as a function of graphene loading in graphene filled layers in PMMA/PMMA+GNP 2049 layers system based on quasi-static (left) and DMA (right) experiments. Reproduced from [234].

Apart from improved Young's modulus, increased toughness and strain at break have also been achieved through multilayer coextrusion [226,228,230,232,235]. Gao et al. [226] demonstrated the elongation at break increased from ~100% for monolayer PP/CB composites to 350% for multilayer PP/CB system (Figure 2.31). This was explained to be due to cracks starting from the PP+CB layer were stopped on the multilayer interface, causing scattering crazes in the neighbouring PP phase as illustrated in the micrograph inserted in Figure 2.31. Therefore, more energy is required for complete cracking, resulting in an increased ductility. Similarly, Lichao et al. [235] reported that elongation at break of multilayered LDPE/mica composites are 3 times larger than those of conventional samples.

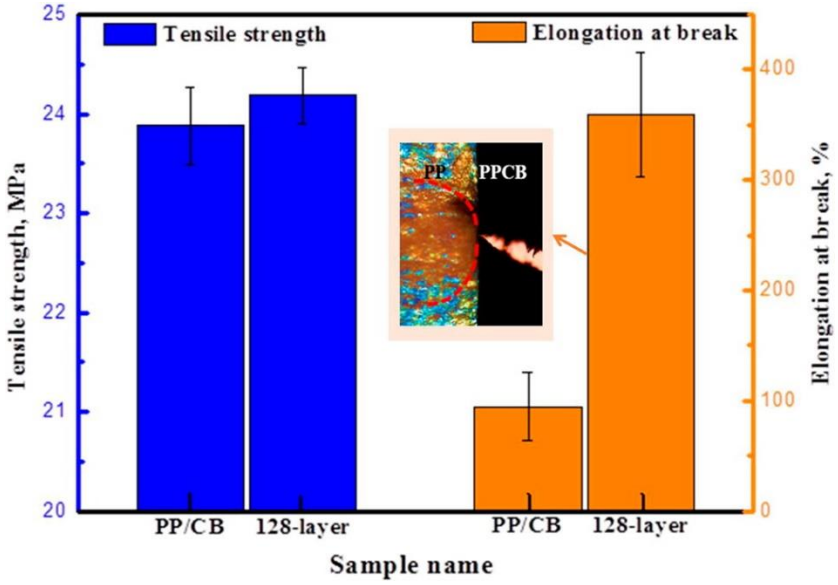

Figure 2.31. Black: Change in tensile strength for traditional PP/CB composites and 128 layer PP/PP+CB composites. Orange: Change in elongation at break for traditional PP/CB composites and 128 layer PP/PP+CB composites. Both composites have a total CB loading of 7 wt%. Reproduced from [226].

2.6 Conclusions

Over the years, graphite nanoplatelets (GNPs) has been used successfully to fabricate polymer composites with multifunctionality. The unique 2D structures provide more interfaces between the matrix and fillers at the same loading compared to that of 1D CNT. In order to achieve optimal reinforcement, proper morphological control is required. For example, platelets with imperfections and folds usually decrease their reinforcing capabilities, therefore

processing methods that contribute to the exfoliation and dispersion of GNPs will produce composites with greater reinforcement. Moreover, controlled alignment of GNPs and better quality of distribution can also enhance other properties of the resulting composites. For instance, polymer/graphene composites subjected to thermal annealing demonstrated a randomized GNP orientation and improved electrical conductivity was achieved [111], whereas highly-oriented platelets usually improve the mechanical properties [249]. It can be concluded that, for achieving targeted properties, a processing method should be carefully selected.

Multilayer coextrusion was used widely in the past years to achieve composites with desired properties simultaneously by engineering the spatial organization of fillers in the polymer matrix. In addition, variable properties could be achieved by altering key parameters such as the number of layers, fillers loadings in the filled layers and selections of paired polymers. Such advanced technology with specific morphological control can guide future research on polymer graphene composites, producing man-made nanocomposites with nano-engineered hierarchy [250].

Chapter 3 - Influence of filler size on properties of PLA/GNP nanocomposites

3.1 Introduction

According to the review in Chapter 2, the properties of GNP itself will have a significant impact on the properties of the resulting composites. Therefore, it is important to have a comparative study to understand the influence of GNP size on the properties of PLA/GNP composites before multilayer coextrusion.

Relatively few studies have investigated the relationship between graphene particle size and composite properties. Kim and Macosko [111] investigated the influence of particle size on composites by incorporating functionalized graphene sheets (FGS) and graphite nanoplatelets (GNP) into a polycarbonate (PC) matrix. They incorporated FGS (thickness (t) = 1-4 nm; diameter (d) ≈ 0.5 µm) and GNP (t ≈ 40 nm; d ≈ 1 µm) into PC and reported a modest increase in Young's modulus of 3.8 % for 1 wt% GNP and 6.7 % for 1 wt% FGS. However, since surface structure was also altered through the introduction of functional groups at the surface of these FGS, reinforcement effects for this system could not be solely attributed to particle size but might also be partly the result of improved interfacial interactions through functional groups. Kim and Jeong [74] investigated the addition of expanded graphite (EG) (t ≈ 15 nm; d ≈ 10 µm) and natural graphite (NG) (t ≈ 20 µm; d ≈ 500 µm) to a PLA matrix and reported an increase in Young's modulus of 38 % for 5 wt% EG and 20 % for 5 wt% NG. Pinto et al. [251] added two types of GNPs, xGNP-C750 and xGNP-M5 from XG Sciences, Inc. into PLA and found Young´s modulus increased by 14 % in the case of 5 wt% filler content. Also, tensile strength

was increased by 20 % for xGNP-C750 and by 6 % for 5 wt. % of xGNP-M5. However, in that study characterization was focused on the biodegradation behaviour rather than on the effect of particle size on composite physical properties, which were not discussed or analysed in any detail.

In this chapter, we investigated the influence of particle size on mechanical, electrical and thermal properties of PLA nanocomposites through the use of two types of GNP. For this purpose, we selected two types of xGNPs from XG Sciences, Inc. of different particle sizes and aspect ratios (AR). Small xGNP-C750 (GNP-S) and large xGNP-M15 (GNP-L) particles were melt-compounded with PLA and the resulting nanocomposite properties were evaluated.

3.2 Experimental

3.2.1 Materials

Polylactide (PLA) (2002D - NatureWorks Co. Ltd., USA,) with a density of 1.24 g/cm^3 and a molecular weight of 204453 g/mol was purchased from Resinex, UK. PLA 2002D has ~4% of D-lactic monomer and a melting temperature of ~170 °C. GNPs were purchased from XG Sciences, Inc. (Lansing MI, USA). xGNP-C750 refers to GNPs with an average diameter (*d*) of 1 µm and a surface area of 750 m^2/g, according to the manufacturer's datasheet. xGNP-M15 has a larger diameter of 15 µm but a lower surface area of 150 m^2/g. According to the manufacturer, xGNP-C750 particles have a slightly lower thickness (t ≈ 2 nm) compared to xGNP-M15 (t ≈ 7 nm), which results in aspect ratios (AR) of ~500 for xGNP-C750 and ~2000 for xGNP-M15. Both GNPs are used as received. For simplicity and clarity xGNP-C750 is referred to as GNP-S (small) and xGNP-M15 as GNP-L (large) in this study.

3.2.2 Sample preparation

Nanocomposites with 5, 7, 10, 13 and 15 wt% GNP in PLA were prepared by melt compounding using an X'plore 15cc mini-extruder (DSM, The Netherlands). Compounding was performed at 180 °C under nitrogen atmosphere. The screw speed was kept constant at 245 rpm for 9 min. The extruded strands were successively pelletized and compression moulded at 180 °C and 50 bar for 3 min in 130 µm thick films using a Collin hot press P300E (Germany) .

3.2.3 Characterization

Raman spectroscopy was performed at room temperature using a 532 nm laser and a power density of 100 mW/mm^2 (LabRam Aramis).

Scanning electron microscope (SEM) (FEI Inspector-F, The Netherlands) were used to characterize the GNP powders as well as PLA/GNP composites. GNP powders were dispersed in acetone and subsequently deposited onto conductive glass slides. All composite specimens for PLA/GNP-S and PLA/GNP-L were prepared by cold-fracturing the composite films in liquid nitrogen. Fracture surfaces were gold sputtered before analysis.

X-ray diffraction (XRD) analysis was performed on a Siemens D5000 Diffractometer using Cu (Kα) radiation (wavelength: 1.54 Å) at room temperature in the range of 2θ = 5° to 40° at a scanning rate of 20 min^{-1}.

The electrical conductivity of all samples was measured by a two-point probe station using a picoammeter (Keithley 6485) and a DC voltage source (Agilet 6614C). Samples were cut in rectangle shapes (20.5 mm x 5 mm x 2 mm) and silver paste coating was used to ensure good contact with the electrodes of the electrometer. Specimens with a resistivity exceeding 10^{10} Ohm are considered as 'non-conductive' as the electrical resistivity is no longer measurable. The electrical percolation was taken as the concentration where its resistance decreases to 10% of that of neat PLA following work by Kim and Macosko [111].

Tensile tests were performed using an Instron 5586 at room temperature, equipped with a 1 kN load cell. Samples were cut in dumbbell shapes (geometry type 5, ASTM 668) and were tested with a rate of 10 mm/min. Reported values were calculated as averages over five specimens.

Dynamic mechanical analysis (DMA) spectra were obtained with a DMA Q800 (TA Instruments). Samples were tested under film tension mode. A frequency of 1 Hz with a temperature ramp of 3 °C/min scanned from room temperature to 150 °C was employed. At least three tests were carried out for each material.

Differential scanning calorimetry (DSC) (Mettler-Toledo 822e) was used to investigate the thermal properties of the nanocomposites. All samples were heated to 200 °C at 10 °C/min. Crystallinity was determined using a heat of fusion for 100 % crystalline PLA of 93.6 J/g [185].

Thermogravimetric analysis (TGA) was performed on a TA Instruments Q500 (TA Instruments). Samples weighing 5-7 mg were heated from room temperature to 700 °C at a rate of 10 °C/min under nitrogen atmosphere.

Heat distortion temperature (HDT) was determined using a DMA Q800 (TA Instruments). A constant load of 1.83 MPa was applied at the mid-point of a 3-point bending sample according to ATSM Standard D648 at a heating rate of 2 °C/min from room temperature to 150 °C.

3.3 Results and discussion

3.3.1 Characterization of GNP filler

The structural defects of graphene play a crucial role in the final properties of this filler and their composites. Raman spectra for both GNP particles are shown in Figure 3.1. Three prominent bands can be seen: D band, G band, and 2D band appearing around 1335, 1580 and 2680 cm^{-1}, respectively. The band frequencies and intensity ratios of D and G bands are listed in Figure 3.1. It is well known that the intensity ratio of D (I_D) to G (I_G) band can be used as an indicator of defect quantity [252,253]. The fewer the defects, the lower the I_D/I_G value. GNP-L exhibits an I_D/I_G value of 0.49, which is lower than that of GNP-S (0.56), indicating less defects. It should be noted that lower I_D/I_G value usually indicates more disordered structures. Such disordered structures include defects, edges, crystal boundaries, symmetry breaking, etc and will be examined using SEM in the next session. It is believed that Raman spectroscopy is also a particularly useful technique to characterise graphene monolayers, bilayers and multilayers [4] as discussed in Chapter 2. For both GNP-S and GNP-L, the 2D band is weaker than the G band, indicating a multilayer structure for both fillers.

Normalized X-ray diffraction (XRD) spectra of both GNP fillers are presented in Figure 3.1. A typical carbon peak at $2\theta = 26°$ is present for both GNP fillers while GNP-L has a much sharper peak, possibly indicating larger thickness for GNP-L [254]. Detailed analysis will be done in the XRD session.

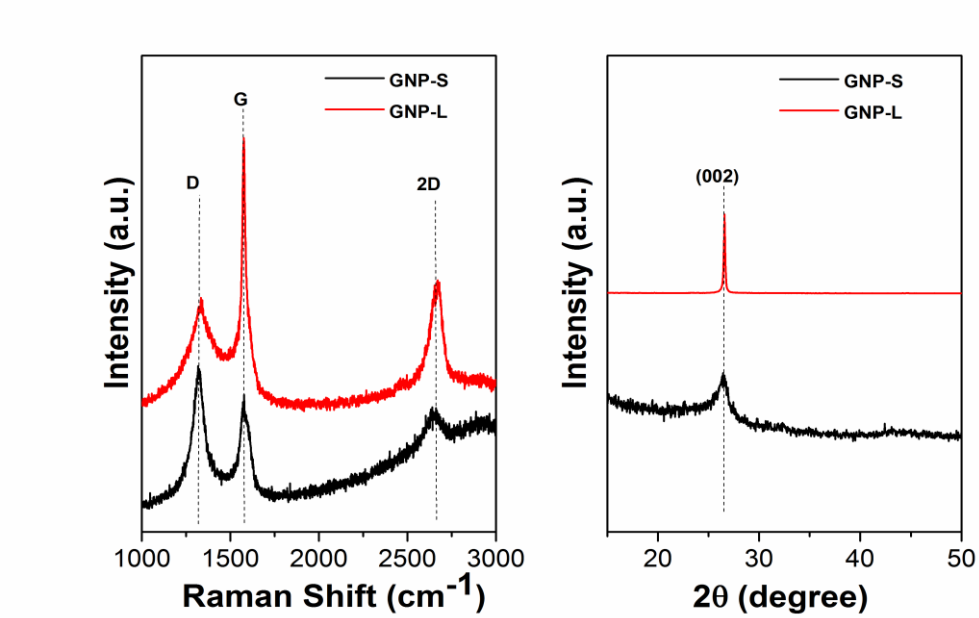

Figure 3.1. Raman spectra for the two GNPs (left) and X-ray diffraction (XRD) patterns of two GNPs (right) before mixing.

Table 3.1. Frequency of D, G and 2D bands and intensity ratio of D and G bands for the two pristine GNPs.

Filler	ω_D (cm^{-1})	ω_G (cm^{-1})	h_{2D} (cm^{-1})	I_D/I_G
GNP-S	1335.2	1580.7	2682	0.56
GNP-L	1333.6	1575.8	2680	0.49

Representative SEM images are shown in Figure 3.2. SEM also indicated that in powder form GNP-S tends to form agglomerates while GNP-L reveals more individual flakes. Platelet dimensions are later summarized in Table 3.2. Similar results were observed by Kumar et al. [255]. Average diameters of GNP-S and GNP-L were calculated to be ~1.2 µm and ~14 µm, respectively using image J software and by measuring at least 50 flakes.

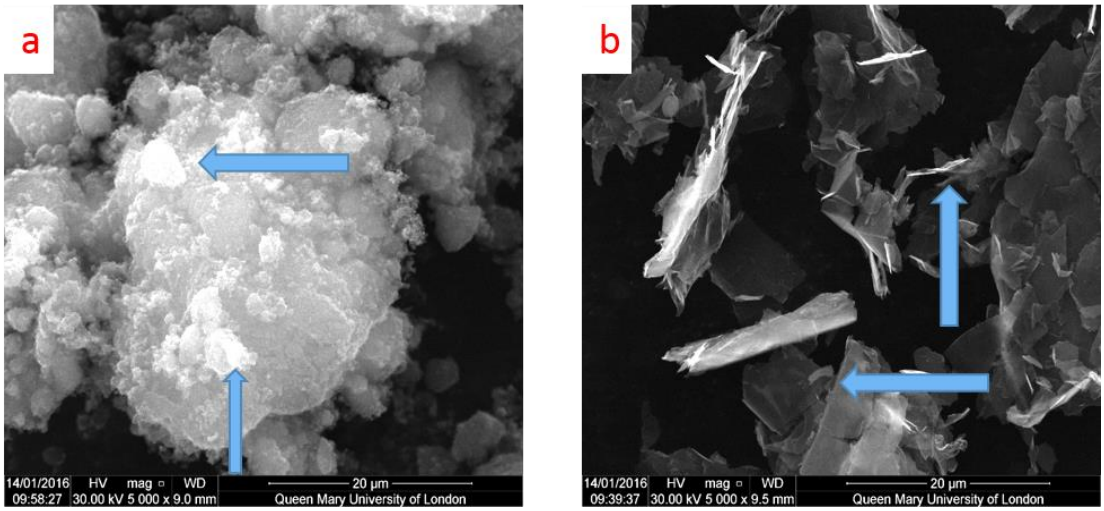

Figure 3.2. SEM images showing pristine (a) GNP-S agglomerates and (b) GNP-L with arrows indicating individual flakes.

3.3.2 Dispersion of GNP in PLA matrix

A uniform and homogeneous dispersion of nanofillers in polymer matrices is vital for achieving an optimal mechanical property profile in nanocomposites. Micrographs of PLA/GNP-L and PLA/GNP-S composites are shown in Figure 3.3 and Figure 3.4. Fracture surfaces were generally rougher for GNP-L, indicating more crack deflection due to the larger GNP-L particles. For GNP-S nanofillers, having a much smaller lateral size than GNP-L, good dispersion can be observed for loadings as high as 10 wt%. The GNP-L particles tend to show some agglomeration for loadings ≥ 7 wt% while a layered graphitic structure is visible at 10 wt%. This agrees with earlier studies by Wang et al. [256], which showed that smaller GNP particles are easier to disperse in epoxy matrices than larger particles.

Figure 3.5 gives a detailed view of some GNP flakes in PLA matrix, with the GNP-L nanoplatelets clearly exhibiting a multi-layered structure with some surface irregularities, cavities and cracks.

SEM images were also analysed using image J software to measure the average size of both GNP-L and GNP-S after compounding. Average particle diameters measured for both small GNP-S and large GNP-L were ~0.7 µm and ~8 µm, respectively. Compared to particle sizes of as-received GNP-S and GNP-L (~1.2 µm and ~14 µm, respectively) as measured by SEM in the previous section, the diameter of GNP-S was reduced by roughly a third while the diameter of GNP-L was nearly reduced by half during melt-compounding. Clearly, larger GNPs are more susceptible to shortening and break-up of nanoplatelets during high-shear melt mixing [233]. In addition, GNPs of larger diameter are more susceptible to breakage after compounding, effectively lowering their aspect ratio even further.

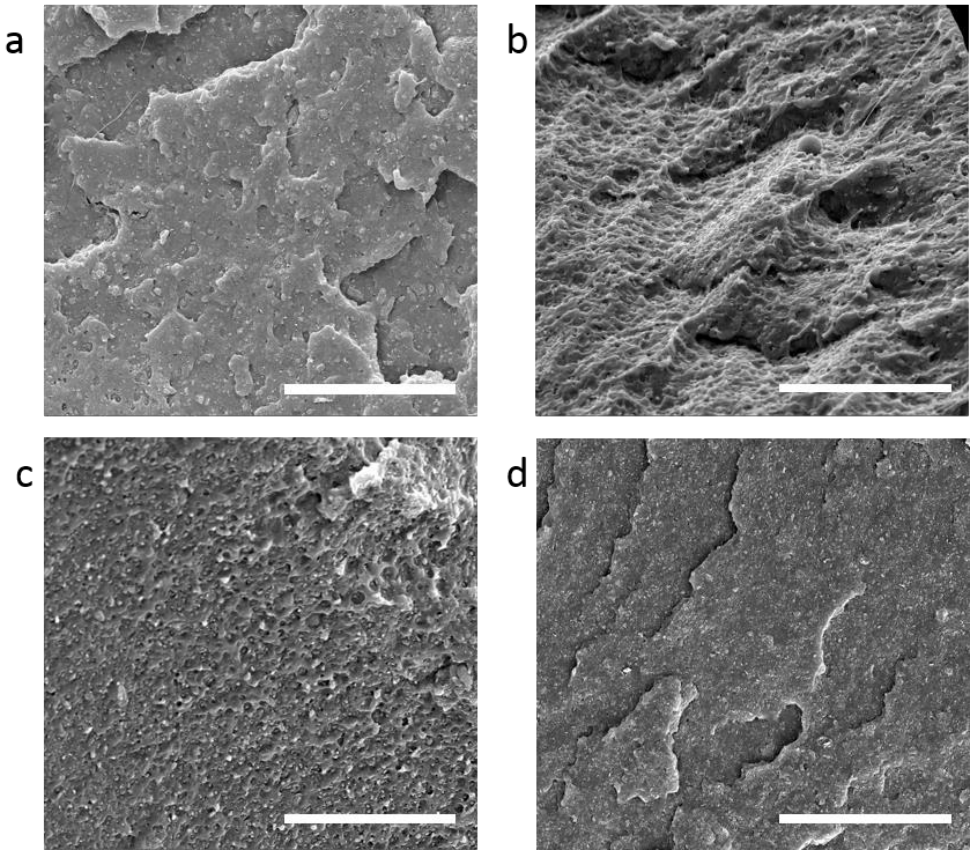

Figure 3.3. SEM images showing dispersion of GNP-S in PLA matrix at filler loadings of (a) 5 wt%, (b) 7 wt%, (c) 10 wt%, and (d) 15 wt%. Scale bar = 20 µm.

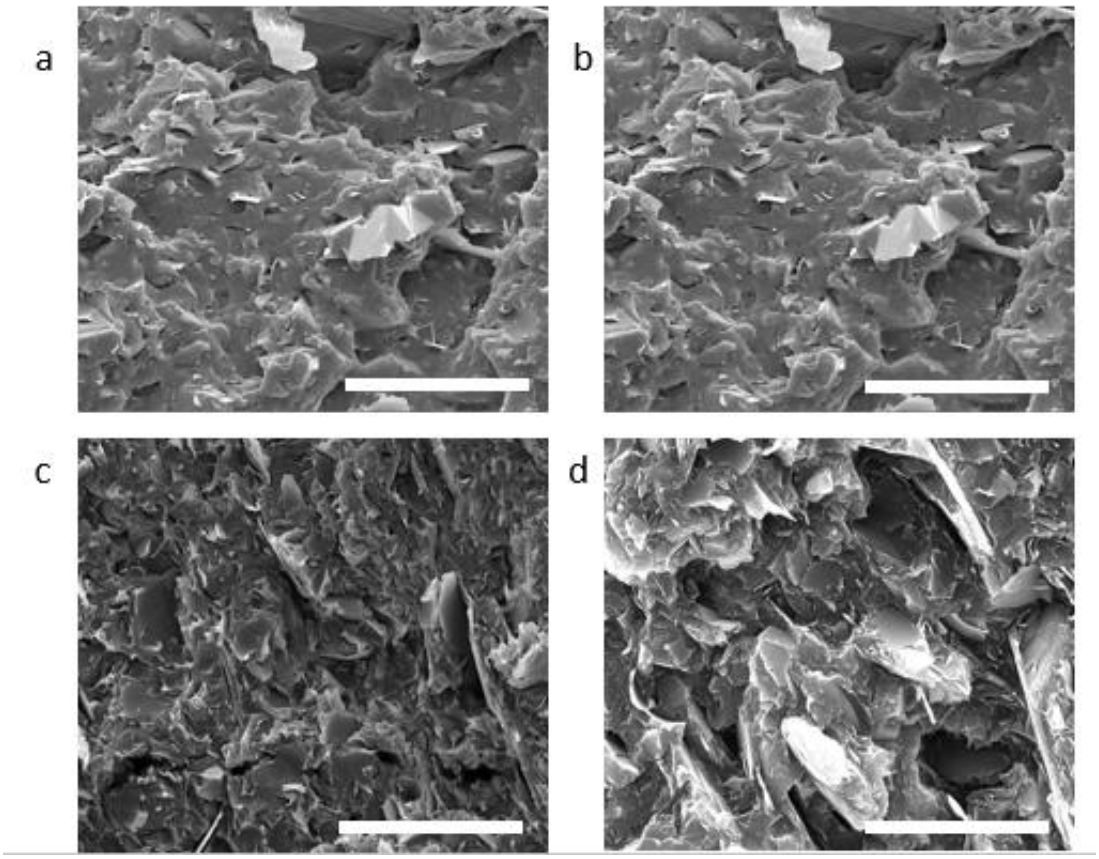

Figure 3.4. SEM images showing dispersion of GNP-L in PLA matrix at filler loadings of: (a) 5 wt%, (b) 7 wt%, (c) 10 wt%, and (d) 15 wt%. Scale bar = 20 µm.

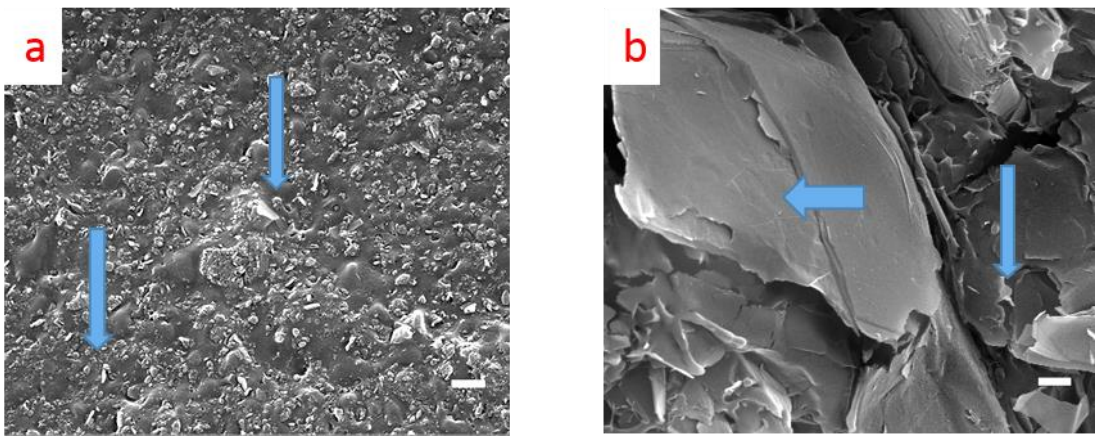

Figure 3.5. Typical GNP particles (15 wt%) in PLA matrix (GNPs indicated by arrows); (a) GNP-S; and (b) GNP-L. Scale bar = 1 µm.

To investigate further the structural features of PLA/GNP-S and PLA/GNP-L composites, X-ray diffraction (XRD) patterns of hot pressed films were obtained and are presented in Figure 3.6.

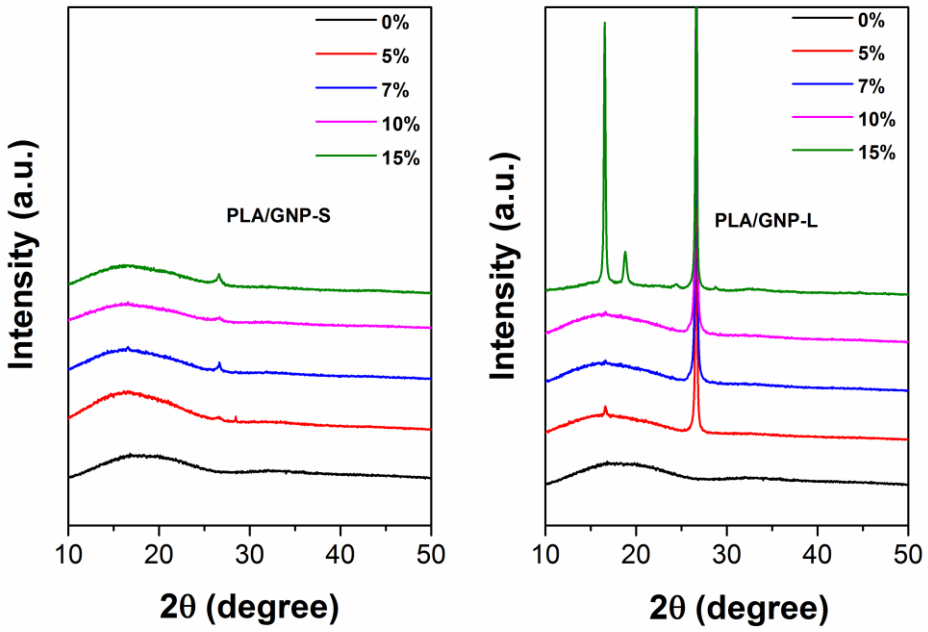

Figure 3.6. X-ray diffraction (XRD) patterns of PLA/GNP-S and PLA/GNP-L nanocomposites with different filler loading, showing structural changes in composites with increasing amount of GNP filler.

A broad amorphous peak from PLA was observed in neat PLA at around 16.8°. This confirms that neat PLA has predominantly an amorphous microstructure. As the graphene loading is increased in both systems, the intensity of this diffraction peak becomes stronger, indicating an increase in crystallinity with increasing GNP loading. Such results were also reported for Poly(lactic acid)/Poly(ethylene glycol)/GNP [198] system as well as Poly(lactic acid)/Epoxidized Palm Oil Blend system [254]. Notably, composites with GNP-L demonstrated a much stronger peak than those with GNP-S at the same loading, indicating that large GNP-L fillers induce a higher polymer crystallinity than small GNP-S in the composites. The XRD results also demonstrated that the crystallinity of PLA is slightly increased with the incorporation of both types of GNP regardless of their size. More quantitative measurements of crystallinity are discussed later in this chapter.

Our data also showed a very strong diffraction peak for all PLA/GNP-L systems at 2θ = 26° (Figure 3.6), which is typical for graphene. Similarly, PLA/GNP-S nanocomposites exhibited a peak at the same position but much weaker. This is understandable since pristine GNP-S is less crystalline than pristine GNP-L as was already shown in Figure 3.1, and as reported in the literature [251].

XRD can also provide information with regards to the stacking thickness of the GNP crystallites. The average out-of-plane crystallite thickness of the GNPs (t) was estimated using the (002) full width at half maximum (FWHM) 2θ values and the Scherrer equation:

$$t = \frac{0.89\lambda}{\beta\cos\theta} \tag{3.1}$$

Where β is the line breadth (FWHM) in radians with the instrumental broadening subtracted, λ is the X-ray wavelength and θ is the diffraction angle of the peak of interest (002). Based on Equation (3.1), it can be calculated that pristine GNP-S has a thickness of ~10 nm while pristine GNP-L exhibits a higher thickness of ~40 nm. These dimensions remain roughly the same in the composites regardless of the GNP loading (~13 nm and ~42 nm, respectively). These thickness values are however far higher than the manufacturer's data (t ≈ 2 nm for GNP-S, and t ≈ 7 nm for GNP-L).

Using the experimental diameter data from SEM and thickness data from XRD, we can now calculate the aspect ratios (AR) of the fillers in the composites to be in the range of 5-200 for GNP-S and 12-420 for GNP-L. Size information is summarized in Table 3.2.

Table 3.2. Average thickness (t) information from XRD and diameter (d) from SEM together with effective aspect ratios (AR) measured as well as back-calculated by micromechanical modelling for the two GNPs in the composites.

Filler	t^a (nm)	t^b (nm)	d^a (µm)	d^b (µm)	AR^b	AR^c
GNP-S	10 (±1)	13 (±6)	1.2 (±0.4)	0.7 (±0.6)	5-200	5
GNP-L	40 (±4)	42 (±4)	14 (±6)	8 (±4)	12-420	12

[a] data for pristine GNPs
[b] data for GNPs in composites
[c] data from mechanical modelling.

The state of GNP dispersion, aspect ratio and orientation was also correlated with nanocomposite properties. In the next section electrical conductivity and the effect of annealing on conductive network formation will be investigated, while corresponding aspect ratios will be estimated from theory and compared with measured data.

3.3.3 Electrical properties

The state of dispersion of nanofillers affects a whole host of physical properties including electrical properties in the case of conductive nanofillers. Figure 3.7 shows the changes in bulk electrical resistivity of PLA/GNP-S and PLA/GNP-L composites before and after annealing for 0.5 h and 1 h respectively as a function of the GNP loading. Considering the melting temperature of ~169 °C for PLA matrix, a higher temperature of 180 °C was selected for annealing.

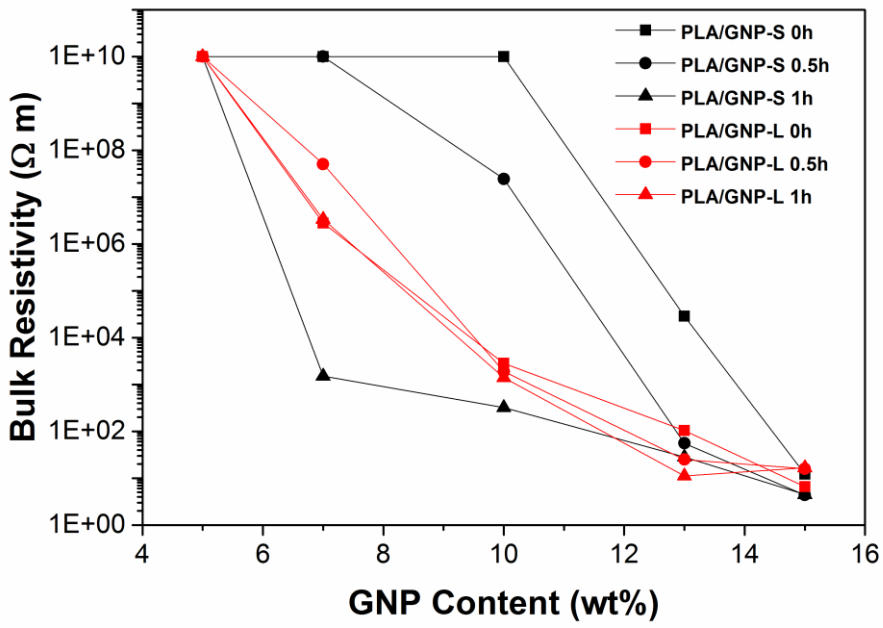

Figure 3.7. Bulk electrical resistivity of PLA/GNP nanocomposites before and after annealing for 0.5 h and 1 h at 180 °C as a function of GNP loading; Black: PLA/GNP-S, Red: PLA/GNP-L. Not measurable data is plotted as 1E+10 Ωm.

Both the addition of GNP-S and GNP-L nanofillers resulted in significantly improved electrical conductivity of PLA at higher filler loadings. In the case of PLA/GNP-L nanocomposites, the electrical resistivity decreased significantly at a filler loading of only 7 wt%, indicating a lower percolation threshold for this higher aspect ratio nanofiller, presumably because of its high aspect ratio as discussed in Chapter 2. On the other hand, the low aspect ratio GNP-S systems showed no conductivity until a fairly high loading of 13 wt%. These results are in agreement with other studies. Kim et al. [74] reported that the percolation threshold for PLA/NG (AR = 25 based on supplier's data) composites lay somewhere between 7 and 10 wt%, while PLA/EG composites based on higher aspect ratio expanded graphite (AR = 667 based on supplier's data) exhibited a percolation threshold between 3 and 5 wt%.

However, interestingly upon annealing, GNP-S revealed a significant decrease in resistivity together with a reduced percolation threshold below 7 wt% (see Figure 3.7). On the contrary, the PLA/GNP-L system showed nearly no change in resistivity and percolation threshold upon annealing. A number of studies have shown that the electrical properties of nanocomposites are not only dependent on filler type and treatment but also on initial dispersion and and processing history [257–261]. Furthermore, it is well documented that the formation of a conductive nanofiller network within a polymer matrix is a dynamic process that depends strongly on time and temperature [153,262–264]. Dynamic percolation phenomena were mainly observed for one-dimensional (1D) carbon nanotubes (CNT) [262,265–268] and zero-dimensional (0D) carbon blacks [269,270]. Zhang et al. [262], for example, observed that the electrical conductivity of annealed TPU/CNT films was up to eight orders of magnitude higher than that of as-extruded pellets. Cipriano et al. [269] studied multiwalled carbon nanotube (MWCNT) and carbon nanofibre (CNF) filled polystyrene composites and also observed an increase in conductivity with different annealing times and temperatures. Deng et al. [271] reported a five fold reduction in percolation threshold in oriented PP/MWCNT tapes after annealing. The MWCNTs involved in most of these studies had typical diameters of around 9.5 nm and lengths of 1.5 µm, which is of the same order as the small GNP-S used in our experiments. Bilotti et al. [153] showed that dynamic percolation is a thermally activated Arrhenius process that links percolation formation to polymer viscosity. All of this supports the observation that smaller fillers are more effective than large fillers in reducing the percolation threshold by annealing, which is the case in our experiment. Further experiments will be designed to investigate this phenomenon in more detail.

3.3.4 Mechanical properties

Tensile behaviour

Figure 3.8 shows representative stress-strain curves of the various nanocomposites, while Figure 3.9 plots the energy to break (or tensile toughness) as calculated from the area under the stress-strain curves. Table 3.3 gives a summary of desired mechanical properties of the composites. Incorporation of both GNP-L and GNP-S increases the Young's modulus of the nanocomposites at all loadings. Tensile strength increased for the composites up to 5-7 wt% depending on filler type but decreased at higher loadings due to agglomeration. Strain at break was reduced with the addition of GNP for all composites, with the exception of the system with 5 wt% GNP-S. Interestingly, despite the fact that fracture surfaces showed some pull-out for larger platelets (see Figure 3.4) the smaller GNP-S platelets preserved better the polymer ductility. Polymer yield was observed for all systems based on GNP-S, while embrittlement was observed for GNP-L based systems. Interestingly, ductility of the PLA was fully preserved for nanocomposites incorporating 5 wt% GNP-S.

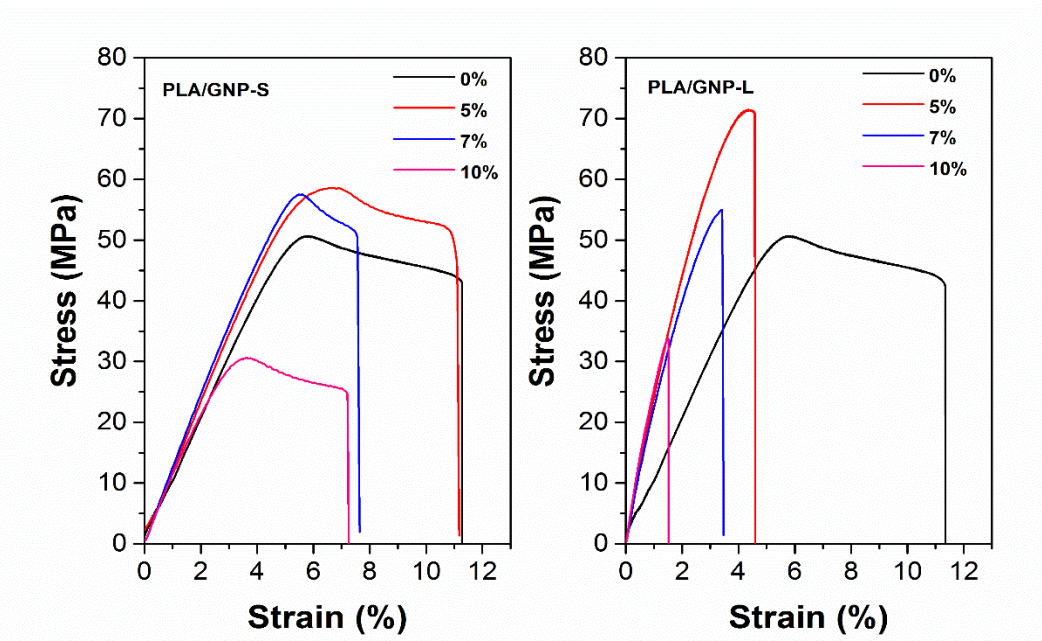

Figure 3.8. Typical stress–strain curves of nanocomposite films for PLA/GNP-S and PLA/GNP-L, showing the highest mechanical reinforcement for 5 wt% GNP-L based nanocomposites and fully preserved ductility for 5 wt% GNP-S based nanocomposites.

Overall a GNP content of 5 wt% gave the best mechanical reinforcement for both the GNP-S and GNP-L systems, with the larger GNP-L nanoplatelets giving the highest increase in Young's modulus and tensile strength, and the smaller GNP-S particles showing the highest ductility.

This is supported by the earlier reported SEM observations. Here pull-out of large GNP-L platelets were indicative of some energy dissipation mechanisms (see Figure 3.4). However, this did not result in a significant overall increase in toughness as larger particles increasingly inhibit yield and plastic deformation of the polymer matrix. In contrast to GNP-L, the GNP-S filler shows little pull-out (see Figure 3.3) because its aspect ratio is too low for effective stress transfer. Higher loadings (≥ 7 wt%) lead to agglomerations of GNPs and resulted in reduced reinforcing efficiency. To conclude, larger platelets exhibit a larger interfacial surface area which makes them more effective in transferring stresses and as a reinforcing filler but at the expense of composite ductility.

It worth noting that interfacial interactions with the PLA matrix are expected to be similar for both GNP-S and GNP-L as both fillers differ only by their size rather than surface chemistry and were also processed under the same conditions. This point is further supported by the fact that little difference in T_g was observed for PLA incorporating either small or large GNPs as will be discussed in more detail in the following section. Regarding toughness, larger interfacial surface area (per plate) will result in higher local stress concentrations in the PLA matrix and embrittlement of the PLA/GNP-L composites. Apart from this, composite ductility may be even more affected by the state of dispersion of the GNPs. More specifically, larger GNPs are more difficult to disperse, causing agglomeration as shown in Figure 3.4 and low toughness. Similar results were reported by Kalaitzidou et al. [77], where larger GNPs in fact showed less reinforcement than smaller GNPs due to agglomerations.

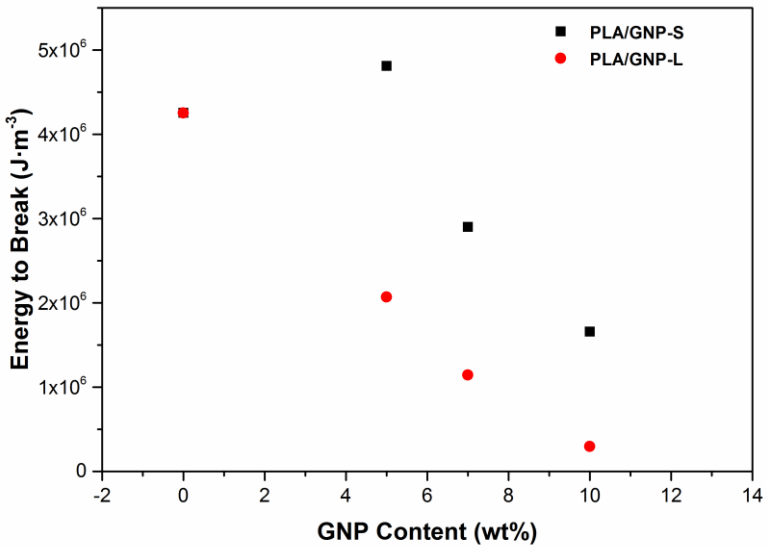

Figure 3.9. Energy to break (or tensile toughness) as a function of GNP loading, showing greater toughness for systems based on GNP-S.

Table 3.3. Summary of mechanical properties for PLA/GNP-S, PLA/GNP-L.

GNP-S (wt%)	Young's Modulus (MPa)	Strain at Break (%)	Tensile Strength (MPa)
0	1043 (±89)	11.2 (±1.2)	50.4 (±7.5)
5	1148 (±71)	10.9 (±0.3)	58.5 (±0.7)
7	1223 (±71)	7.5 (±0.8)	57.5 (±7.3)
10	1354 (±71)	3.4 (±1.3)	30.4 (±5.0)
GNP-L (wt%)	**Young's Modulus (MPa)**	**Strain at Break (%)**	**Tensile Strength (MPa)**
0	1043 (±90)	11.2 (±1.2)	50.4 (±7.5)
5	1290 (±16)	4.5 (±0.2)	71.2 (±4.8)
7	1572 (±79)	2.7 (±0.1)	54.5 (±3.6)
10	1626 (±103)	1.5 (±0.2)	33.5 (±1.2)

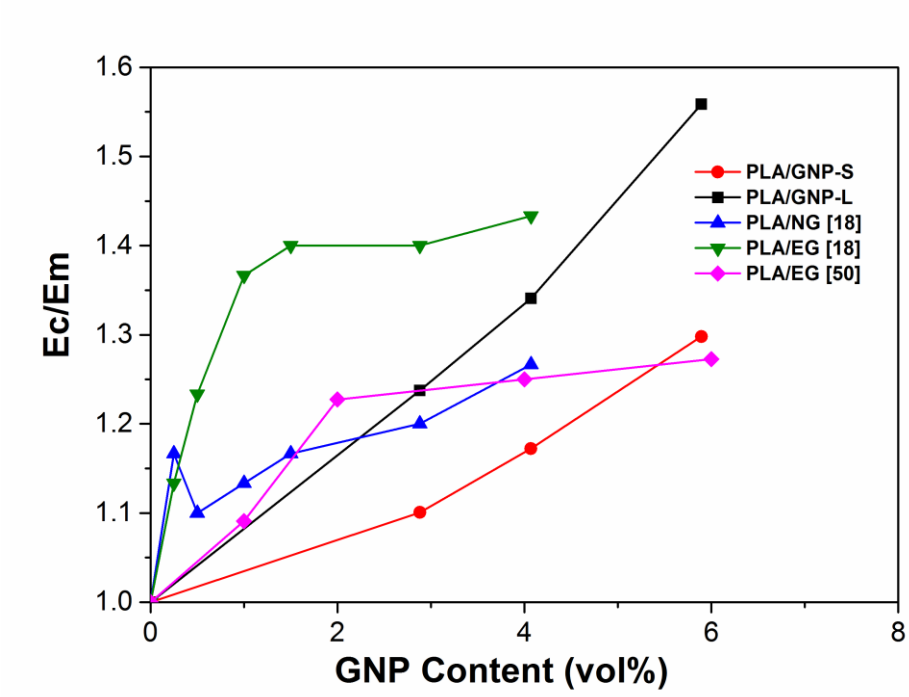

Figure 3.10. Reinforcement efficiency in terms of composite modulus over neat PLA matrix modulus as a function of GNP loading for PLA/GNP-S, PLA/GNP-L together with literature data.

Figure 3.10 shows that the elastic modulus of the current PLA/GNP systems increases linearly with filler content with the maximum increase in Young's modulus of 56 % at around 6 vol%

(10 wt%) GNP-L, being among the highest reported for 3D randomized PLA/GNP nanocomposites. Murariu et al. [196], for example, reported a highest increase of 25 % at 6 vol% graphene loading for PLA/EG composites. Kim et al. [74] reported high reinforcement at relatively low loadings with a 40 % improvement in modulus at 1.8 vol% EG. However, in their system mechanical reinforcement did not increase beyond this filler loading, indicating severe agglomeration and reduced reinforcing efficiency at higher filler loadings. In contrast, the current PLA nanocomposites showed a linear increase in Young's modulus with filler loading in agreement with mechanical models.

Micromechanical analysis

As reviewed in Chapter 2, the Halpin-Tsai model [70] has been used widely in the analysis of graphene and other nanocomposites to predict the aligned reinforcement [263,272,273]. Yet in the case of hot pressed samples after extrusion, 2D platelet-like fillers like graphene often exhibit a 3D random orientation in the polymer matrix made by.

Laminate theory demonstrates that the in plane Young's modulus of a sheet with particles that are randomly oriented in the plane can be approximated by[274]:

$$E_{\text{random 2D platelets}} = 0.375E_{\parallel} + 0.625E_{\perp} \tag{3.2}$$

Where $E_{\parallel}$ is the (upper bound) parallel modulus and $E_{\perp}$ is the (lower bound) perpendicular modulus for unidirectionally aligned platelets as shown in Figure 3.11.

Van es estimated the 3D randomly oriented composites by repeatedly using the 2D randomising method, thus the in-plane Young's modulus of composites with platelets that are 3D randomly oriented can be approximated by [273,274]:

$$E_{\text{random 3D platelets}} = 0.49E_{\parallel} + 0.51E_{\perp} \tag{3.3}$$

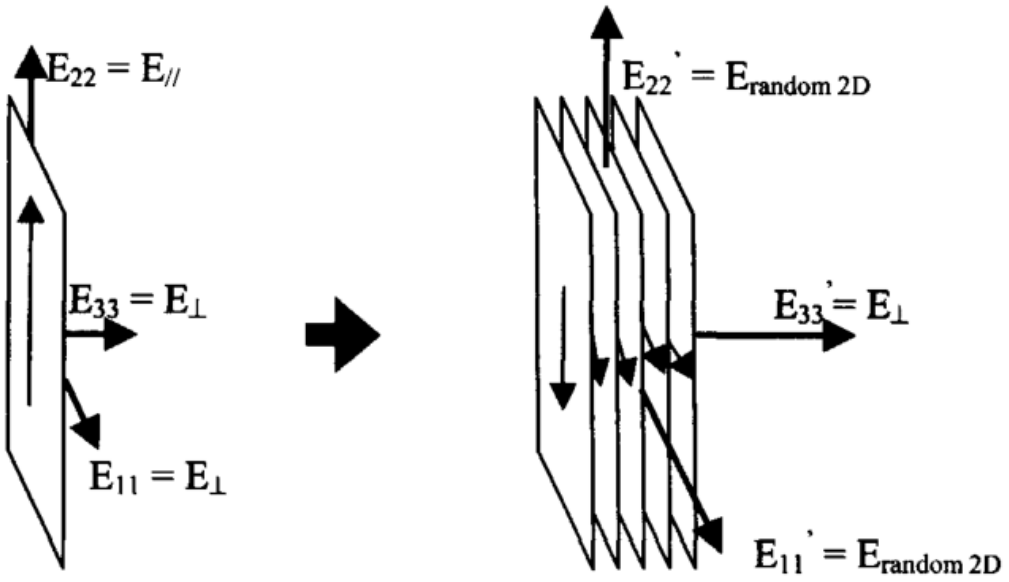

Figure 3.11. Stacking unidirectional plates into 2D random plates.

The Halpin-Tsai equations estimate rather accurately the elastic properties of fibre reinforced composites but generally overestimate the Young's modulus of platelet based composites [274]. This is the consequence of taking $\xi = 2l/t$, which fits better for fibre geometries than platelet geometries. Van Es [274] introduced a correction of the shape factor for composites incorporating platelets with diameter *"d"* and thickness *"t"* assuming that the composite material possesses transverse symmetry around 3-axis. According to his calculations, corrected parameters were proposed for the prediction of Young's modulus $E_{\|}$ and $E_{\perp}$ as:

$$\begin{matrix} E_{\|} & \xi = 2d/3t \\ E_{\perp} & \xi = 2 \end{matrix} \qquad (3.3)$$

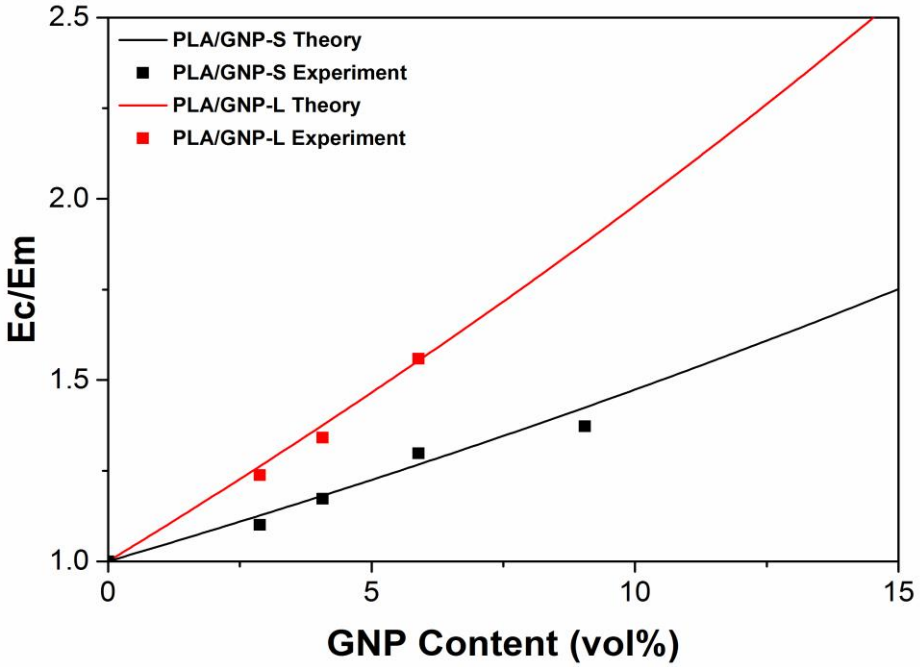

Figure 3.11. Theoretical fit using modified Halpin-Tsai model of GNP reinforcement in PLA matrix. Black squares: experimental data for PLA/GNP-S composites; Red squares: experimental data for PLA/GNP-L composites; Black line: 3D random theoretical fit using AR=5. Red line: 3D random theoretical fit using AR=12.

Experimental data and theoretical fits are plotted in Figure 3.11 and effective aspect ratios were back-calculated assuming 3D random orientations. Using d/t = 5 and 12 and corrected ξ for GNP-S and GNP-L respectively, a good correlation was achieved for composites containing up to 10 wt% GNPs. The low effective GNP aspect ratios (5 and 12) back-calculated from the experimental nanocomposite properties are close to the lower range data from SEM and XRD analysis, suggesting less than optimal reinforcing efficiencies, presumably due to imperfect interfacial interactions. It should be noted that the efficiency of the GNPs could potentially be also improved by orientation of these fillers. Sellam et al. [275], for example, prepared PVA–GO nanocomposites by a layer-by-layer assembly method and found that the effective GO stiffness contribution was twice that of a solution cast system, highlighting the importance of platelet alignment for improved reinforcing efficiency. Further work is foreseen in the near future to explore such possibilities.

Dynamic mechanical behaviour

The glass transition temperature (T_g) was determined from the peak of the tan delta curve from DMA results in Figure 3.12 and average values from at least three tests are summarized in Table 3.4. A small increase in T_g (1~3 °C) is observed with increasing nanofiller content. These results revealed that the additional GNP did not significantly change the mobility of the polymer matrix. It was also noted that addition of both GNP-S and GNP-L lead to a reduction in the sharpness and height of tan δ peak compared to the neat PLA, indicating decreased damping ability and increased crystallinity [276]. Similar reduction was also reported for other PLA-based composites [185,277–279]. Notably, PLA/GNP-L showed more prominent reduction in peak height and sharpness compared to PLA/GNP-S at the same loading, indicating higher crystallinity. DSC will be performed in the next session to give more quantitative information regarding crystallinity.

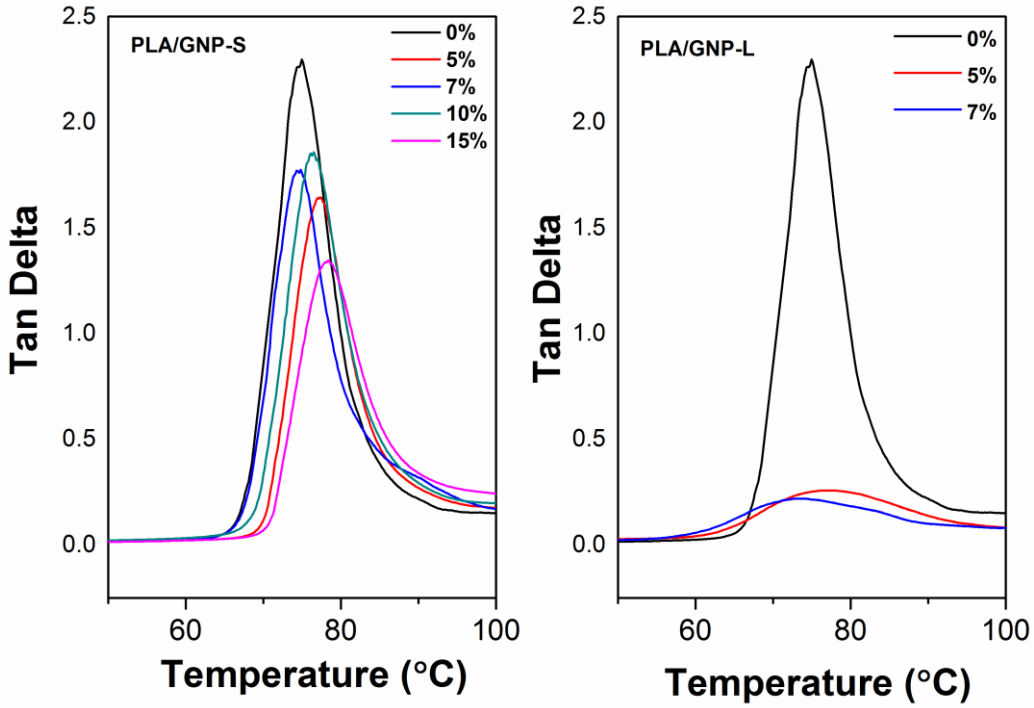

Figure 3.12. Tan δ as a function of temperature for neat PLA, (a) PLA/GNP-S and (b) PLA/GNP-L. Composites with 10 and 15 wt% GNP-L were not measured due to sample brittleness.

Table 3.4. T_g values for all PLA/GNP nanocomposites as obtained from DMA.

Sample	GNP content (wt%)	T_g (DMA) (°C)
PLA	0	75±2
PLA/GNP-S	5	77±1
	7	74±1
	10	76±2
	15	78±3
PLA/GNP-L	5	77±3
	7	74±4

3.3.5 Thermal properties

Differential scanning calorimetry

Nanofillers are known to act as nucleating agents in polymer matrices, altering the polymer crystallinity in nanocomposite systems. Since PLA is a semi-crystalline polymer, its mechanical properties will strongly depend on crystallinity and observed increases in mechanical properties may not be solely the result of mechanical reinforcement by the filler. In order to evaluate the influence of polymer crystallinity on the mechanical enhancement of the nanocomposites, DSC was employed to measure the crystallinity of the various PLA/GNP nanocomposites as well as that of the neat PLA polymer. Melting points of the neat PLA matrix and PLA/GNP nanocomposites are nearly the same. The crystallinity (X_c) in all samples was calculated as follows:

$$\mathrm{Xc}(\%) = \frac{\frac{\Delta \mathrm{Hm} - \Delta \mathrm{Hcc}}{\phi_{\mathrm{PLA}}}}{\Delta \mathrm{H}_{\mathrm{m}}^{\mathrm{o}}} \times 100\% \tag{3.4}$$

where $\Delta \mathrm{Hm}$ is the measured heat of fusion, $\Delta \mathrm{Hcc}$ is the heat of cold crystallization, ϕ_{PLA} is the PLA content in the composites and $\Delta \mathrm{H}_{\mathrm{m}}^{\mathrm{o}}$ is melting enthalpy of the 100 % crystalline PLA (93.6 J/g) [185]. DSC results of the different PLA/GNP nanocomposites, together with heat distortion temperatures (HDT) as obtained by DMA, are listed in Table 3.5 and compared with values for other PLA based nanocomposites from literature.

Table 3.5. The glass transition temperature (T_g), melting temperature (T_m), and crystallinity (X_c) of neat PLA, PLA/GNP-S and PLA/GNP-L composites obtained from DSC together with heat distortion temperatures (HDT) from DMA and literature data.

Sample	GNP (wt%)	T_g (°C)	T_m (°C)	X_c (%)	HDT (°C)
PLA	0	64±2	169±2	1.8±0.7	63±1
PLA/GNP-S	5	64±1	167±2	2.5±1.0	66±1
	7	64±1	167±1	2.0±0.3	71±2
	10	64±2	167±1	14.0±1.3	67±1
	15	65±1	168±2	9.3±2.5	72±2
PLA/GNP-L	5	65±1	167±1	6.3±0.5	69±1
	7	65±1	167±2	15.3±0.2	72±1
	10	--	168±1	21.6±2.7	77±1
	15	--	166±2	23.5±2.5	74±2
PLA/MWCNT **[280]**	0	62	--	42.5	77
	1	62	--	41.0	76
	3	62	--	39.9	76
	6	63	--	39.1	78
	13	62	--	40.2	88
PLA/GNP **[281]**	0	--	149	32.1	50
	5	--	153	33.4	51

Similar to the glass transition temperatures, the addition of GNP did not significantly change the melting temperatures of the PLA nanocomposites for both GNP-S and GNP-L fillers. However, it was noted that there is an increase in degree of crystallinity for both types of nanocomposites with the addition of GNP, which is in agreement with the XRD results shown earlier. More specifically, for PLA/GNP-S composites, *Xc* was increased by 0.2-12 % for different filler loadings, while this increase was more pronounced for PLA/GNP-L composites with an increase from 4-22 %. This might be explained by the difference in filler size. Compared to GNP-S, GNP-L may have a stronger effect on hindering the motion of polymer chains and reduce the amorphous portion of composites, leading to higher crystallinity [282].

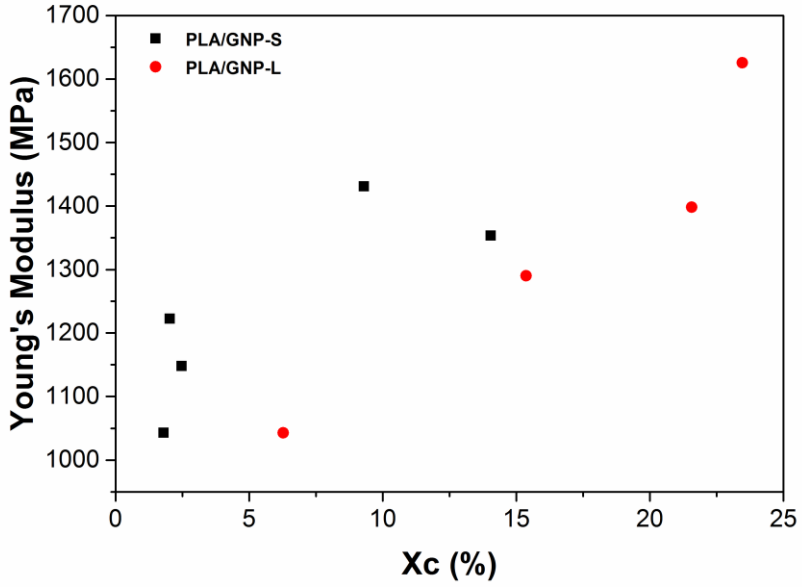

Figure 3.13. Young's modulus as a function of PLA crystallinity for PLA/GNP-S and PLA/GNP-L, showing a strong correlation between modulus and crystallinity for system based on GNP-L.

Figure 3.13 explores the relationship between mechanical properties and polymer crystallinity for systems based on GNP-L and reveals a correlation between Young's modulus and polymer crystallinity. Hence, it may be concluded that property improvements in terms of strength and stiffness for the PLA/GNP-L nanocomposites are not solely the result of filler reinforcement but also affected by changes in polymer crystallinity. On the contrary, such a clear relationship was not observed for the PLA/GNP-S system, indicating that small GNP fillers have little impact on the crystallinity of the PLA matrix. Chieng et al. [198] observed similar effects for their system based on PLA/PEG/GNP. They also observed a small increase in X_c with the addition of graphene at low loadings (≤ 1 wt%). For systems based on 1 wt% GNP-L they reported an increase in X_c by 5 %, which is in reasonable agreement with our data (an increase in X_c by 6 % for 5 wt% GNP-L).

Heat distortion temperature

The low heat distortion temperature (HDT) of PLA limits its application as an engineering plastic. Improved HDTs are often observed in PLA composites, often due to an increase in crystallinity [283,284].

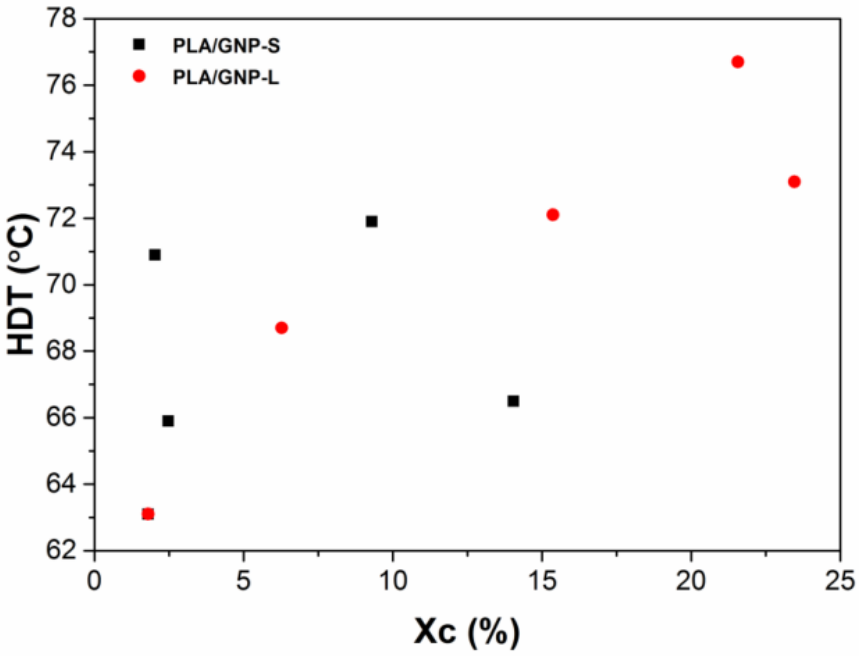

Figure 3.14. HDT as function of PLA crystallinity for PLA/GNP-S and PLA/GNP-L.

Also in the current graphene nanocomposites an increase in HDT with increasing GNP content in the PLA matrix was found for both types of GNP, with GNP-L exhibiting slightly superior HDT behaviour at the same filler loadings (see Table 3.5). More specifically, a linear relationship between HDT and crystallinity for PLA/GNP-L composites is shown in Figure 3.14, ending with a drop for PLA with 15% GNP-L due to filler agglomeration, while data for PLA/GNP-S are rather scattered. The maximum increase in HDT of nearly 14 °C for GNP-L at 10 wt% is among the highest reported for a PLA nanocomposite system. Sobkowicz et al. [198], for example, reported that the HDT of PLA increased by 11 °C with the addition of 14 wt% MWCNT, while Han et al. [281] reported only an increase of around 1 °C in HDT with 5 wt% GNP. Nanocomposites with a relatively high graphene loading (7-10 wt%) exhibited a HDT of 76 °C which is higher than that of Nylon 6 (~60 °C), PET (~65 °C) and PP (~70 °C) [285]. Even so the brittleness of these PLA/GNP nanocomposites (see Figure 3.8) may still inhibit their application in engineering applications and methods to further enhance toughness are important for future success of these materials.

3.4. Conclusions

This study investigated the influence of GNP particle size, aspect ratio and dispersion on the mechanical, thermal and electrical properties of PLA composites. Both high aspect ratio xGNP-M15 and low aspect ratio xGNP-C750 nanofillers were effective in achieving improved mechanical properties of PLA/GNP nanocomposites, with the larger nanoplatelets (GNP-L) displaying the highest mechanical reinforcement. An optimum loading for reinforcement was identified at about 5 wt% GNP for both grades. The reported maximum reinforcement of 24 % in Young's modulus for PLA composites incorporating 5 wt% GNP-L is among the highest reported for isotropic PLA/GNP nanocomposites. Composites based on GNP-L showed embrittlement, while polymer yield was not inhibited for composites based on GNP-S, with ductility of the PLA being fully preserved for systems incorporating 5 wt% small GNP-S.

Percolation thresholds for electrical conduction were lowest for the high aspect ratio GNP-L nanofiller (~7 wt% for GNP-L and ~13 wt% for GNP-S, respectively). However, upon annealing PLA/GNP-S systems showed improved electrical conductivity and a greatly reduced percolation threshold from 13 to around 6 wt%. PLA/GNP-L systems on the other hand did not show such a change in electrical properties after annealing.

The heat distortion temperature (HDT) of both GNP-S and GNP-L based systems increased with filler content, with composites based on larger GNP-L particles exhibiting a slightly superior thermal stability. HDT increased from 63 °C for neat PLA to 76 °C for 10 wt% GNP-L nanocomposites, which is among the highest HDT values reported for a PLA/GNP system.

Chapter 4 - Synergistic effects of filler size on thermal annealing induced percolation in PLA/GNP nanocomposites

4.1 Introduction

In Chapter 3, it was noted that polymer composites with different filler size exhibited varied electrical behaviour after annealing, therefor this chapter will provide further study of this phenomenon.

Annealing of polymer nanocomposites at temperatures above their glass transition temperature (T_g) is known to affect a variety of physical properties [286], most notably the electrical conductivities of composites based on conductive nanocarbons [263,266,287–291]. Annealing has been shown to increase the electrical conductivity at room temperature (RT) of conductive polymer composites by several orders of magnitude [291]. Systematic effects on electrical conductivity have been observed as a function of annealing temperature and annealing time and these relationships can be described using an Arrhenius equation related to polymer mobility [264,269]. When a nanoparticle filled polymeric material is annealed at a temperature sufficiently above its T_g for a sufficient amount of time, the nanoparticles can reorganise themselves in the melt and their connectivity thereby increases. This increase in

connectivity due to network formation of nanoparticles under annealing manifests itself also in the rheological characteristics of a polymer melt, resulting in a more elastic behaviour [264].

This phenomenon, as opposed to traditional statistical percolation, is known as dynamic percolation (DP). It means that, for the same concentration of nanofiller, a polymer composite can show very different conductivity levels as a result of different processing/thermal histories. Dynamic percolation has been observed for one-dimensional (1D) carbon nanofillers like carbon nanotubes (CNT) [262,265–268] and zero-dimensional (0D) carbon black [269,270] filled polymer composites. Deng et al. [270] reported a near five-times reduction in percolation threshold for oriented CNT/polypropylene (PP) tapes after annealing, while Zhang et al. [270] found that the electrical conductivity of annealed films based on CNT/thermoplastic polyurethane (TPU) was up to eight orders of magnitude higher than that of the as-extruded compound. Cipriano et al. [270] studied multiwalled carbon nanotube (MWNT)/polystyrene (PS) and carbon nanofibre (CNF)/PS systems and observed an increase in conductivity with annealing times and temperatures.

The effect of thermal annealing on the electrical properties of GNP/polymer composites and the influence of GNP size on network formation during annealing is however relatively unexplored. Li et al. [234] examined the difference between diffusion displacement of small and large graphene fillers over a short time scale (2 min) in poly (methyl methacrylate) (PMMA) during multilayer coextrusion but no further study on long-term annealing was reported. Kim et al. dispersed small functionalised graphene sheets and larger sized graphite in polycarbonate (PC) [111] and poly (ethylene-2, 6-naphthalate) (PEN) [111] matrices and reported improved conductivity for annealed samples. However, different sample geometries were used in this study thus an unequivocal conclusion on particle size effects in dynamic percolation could not be given.

Apart from annealing, the addition of a secondary conductive or even non-conductive filler to nanocarbon-based conductive polymer composites was also reported to enhance the conductivity of these hybridized nanocomposites. Zhang et al. [152] investigated the dynamic percolation in highly oriented conductive networks formed with different carbon nanofillers upon annealing and concluded that the addition of carbon black was able to accelerate the dynamic percolation process. Bilotti et al. [153] reported controlled dynamic percolation of CNT/TPU composites by adding an insulating needle-like nanoclay (sepiolite) and found

altered percolating networks of CNTs in TPU and a reduced percolation threshold. Despite significant interest in hybrid nanofiller systems, to the best of our knowledge, again no annealing studies have been reported for hybrid GNP based systems.

This chapter studied the influence of graphite nanoplatelet (GNP) size on electrical and rheological properties of PLA nanocomposites upon thermal annealing through the use of two types of xGNPs from XG Sciences, Inc. of different sizes. Small xGNP-C750 particles, large xGNP-M15 particles and hybrids of both fillers were melt-compounded with polylactide (PLA) and resulting nanocomposite properties and behaviour were evaluated before and after thermal annealing in the melt. Such multi-functional materials may be of interest for a variety of applications, most notably sensors [153].

4.2 Experimental

4.2.1 Materials

Polylactide (PLA) (2002D - NatureWorks Co. Ltd., USA), xGNP-C750 and xGNP-M15 were used as-received as described in Chapter 3. For simplicity and clarity xGNP-C750 is referred to as GNP-S (small) and xGNP-M15 as GNP-L (large) in this study.

4.2.2 Sample preparation

Nanocomposites with a total filler loading of 5 wt% but with varying GNP-S/GNP-L ratios (0.5/4.5, 1.5/3.5/, 2.5/2.5, 3.5/1.5, 4.5/0.5) were processed using the same methodology as described in Chapter 3. Here, samples are denoted as PLA/GNP-S_x/GNP-L_{5-x}, where x is the GNP-S loading in these hybrid filler based nanocomposites.

4.2.3 Characterization

The electrical conductivity of all hot pressed samples was measured at room temperature (RT) by a two-point probe station using a Keithley 6485 picoammeter (Textronics, USA) and an Agilet 6614C DC voltage source (Hewlett Packard, USA). Compression moulded disks were

made as described in Chapter 3. From these disks, samples with dimensions 20 mm x 5 mm x 2 mm were cut and silver paste coating was used to ensure good contact with the electrodes of the electrometer. Annealed samples were taken from the oven and left to cool to RT before testing. Specimens with a resistivity exceeding 10^9 Ohm were considered as 'non-conductive' as the electrical resistivity is here no longer measurable using the current experimental set-up.

Real-time dynamic percolation tests were conducted on the same rectangular samples as described above. Samples were heated on a hot plate from RT to a target temperature of 200 °C, with heating being discontinued after 2 hrs. Samples typically reached a temperature of around 180 °C, with conductivity, time, and sample temperature being monitored simultaneously.

Rheology was conducted on an AR 2000 Advanced Rheometer (TA Instruments, UK) connected to an environmental chamber with a 25 mm parallel plate setup. Hot pressed disk shaped samples were measured at 180 °C using a frequency sweep ranging from 0.01 to 100 Hz and a strain of 0.1 %, which is within the linear elastic region of the material.

4.3 Results and discussion

4.3.1 Electrical conductivity of nanocomposites

Figure 4.1 presents the electrical conductivity at RT for all nanocomposites before and after thermal annealing at 200 °C in an oven. Before annealing, both the addition of GNP-S and GNP-L nanofillers resulted in a significantly improved electrical conductivity of PLA at higher filler loadings. In the case of PLA/GNP-L nanocomposites, electrical conductivity increased already significantly for filler loadings of 7 wt%, while the low aspect ratio GNP-S based systems showed no electrical conductivity up to the relatively high filler loading of 10 wt%, indicating a much lower percolation threshold for GNP-L. As reviewed in Chapter 2, Li et al. [116] proposed Equation (2.13) to predict the percolation threshold of polymer nanocomposites containing 3D randomly distributed disc-shaped nanoparticles. Considering that the diameters of both small and large GNPs (1.2 and 14 µm) are two to three orders of

magnitude higher than the required D_{IP} of 10 nm, meaning that the influence of D_{IP} can be neglected and the equation can be further simplified as:

$$V_{f\_3D} = \frac{27\pi t}{4D} = \frac{27\pi}{4A_f} \quad (4.1)$$

where A_f is the aspect ratio of GNP (A_f=D/t).

From Equation (4.1) it can be concluded that larger aspect ratio conductive fillers give lower percolation thresholds, which is in agreement with our experimental data with the larger GNP-L based systems exhibiting a lower percolation threshold than systems based on GNP-S after compounding.

Interestingly, the effects of particle size on electrical conductivity after annealing are very different. Upon annealing, GNP-S based nanocomposites showed a significant increase in conductivity for systems with medium GNP-S loadings (7 to 10 wt%) while the percolation threshold shifts from around 13 wt% GNP-S to values of around 7 wt%. Both 5 and 15 wt% based systems remain unchanged as non-conductive and highly conductive, respectively. In contrast, the PLA/GNP-L system showed hardly any change in conductivity for all concentrations upon annealing, resulting in an unchanged percolation threshold. This suggests that smaller GNP-S flakes have greater mobility in the PLA melt, leading to increased migration and network formation by reagglomeration during annealing than the larger GNP-L flakes. It should be noted that it is not actually the nanoparticle that moves but the polymer molecules that diffuse/relax around the nanoparticle, only indirectly causing “motion” or rather reorganisation of the nanoparticle’s (relative) position, a reduction of inter-particle distance and an increase in electrical conductivity. Although electrical properties remain unaffected for both the 5 wt% and 15 wt% based composites, the reasons behind these unaltered electrical properties with annealing are very different for both systems.

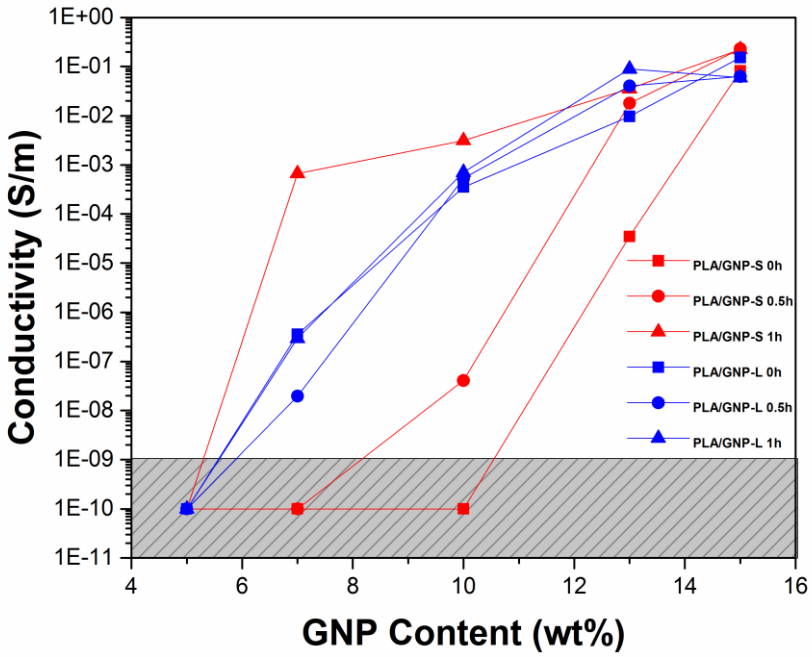

Figure 4.1. Electrical conductivity of PLA/GNP nanocomposites as a function of GNP loading after different thermal annealing times at 200 °C in an oven; Red: PLA/GNP-S, Blue: PLA/GNP-L. No changes in conductivity are observed for all PLA/GNP-L composites with annealing, while an increase in conductivity is observed for 7, 10, and 13 wt% PLA/GNP-S composites. Non-measurable data below 10-9 S/m are plotted as 10 -10 S/m in the shaded grey area for simplicity of drawing.

Composites with too low filler loadings are not able to form conductive networks even after prolonged annealing times as a minimum amount of filler is required to create such a network. On the contrary, high filler loadings result in an initial rigid network that hinders motion of individual nanofillers, leading to a network which is unaffected by annealing. This explains why 15 wt% PLA/GNP-S systems showed little change in conductivity upon annealing. Similarly, only a small increase in electrical conductivity was observed for 13 wt% PLA/GNP-S after 0.5 h annealing. In short, whenever an initial network is present, the system becomes rigid and demonstrates less nanoparticle migration, meaning a limited effect of annealing on electrical properties.

To further investigate the importance of filler size on dynamic percolation, hybrid filler systems based on a fixed total amount of GNP (5 wt%) but with a variable GNP-S/GNP-L ratio

were melt compounded and their conductivity after annealing was measured and is plotted in Figure 4.2.

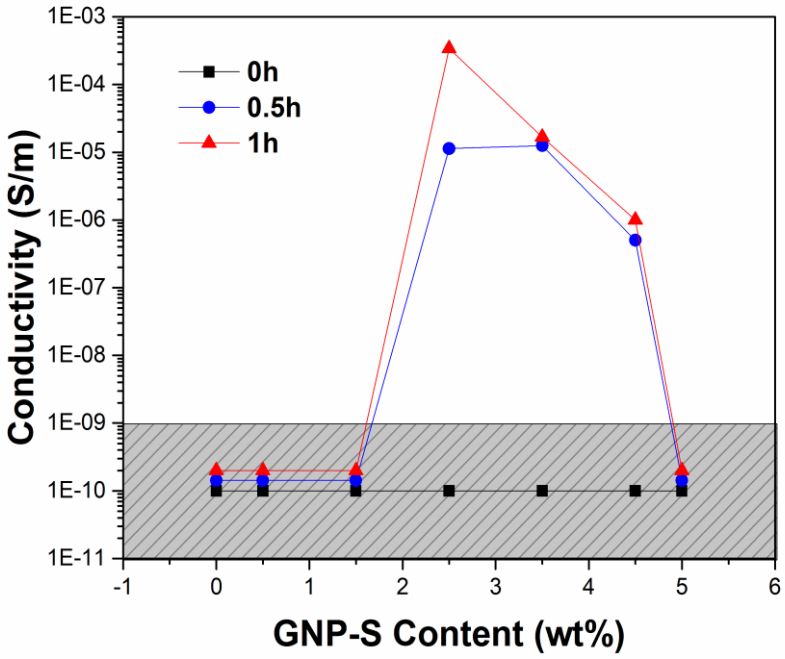

Figure 4.2. The electrical conductivity of PLA nanocomposites with GNP-S_x/GNP-L_{5-x} hybrid fillers as a function of GNP-S content. Total filler content was maintained at 5 wt%. Composites with a 50/50 GNP-$S_{2.5}$/GNP-$L_{2.5}$ hybrid filler ratio showed synergistic effects with the greatest improvement in conductivity after thermal annealing, while composites with a low GNP-S filler content showed no change in conductivity. Black: after 0 h annealing; Blue: after 0.5 h annealing; Red: after 1 h annealing; Shaded grey area represents the non-measurable conductivity range.

Hybrid nanocomposites with 0, 0.5 and 1.5 wt% of GNP-S were non-conductive even after 1 h of annealing. However, when the content of GNP-S reached 2.5 wt% (50/50 hybrid filler ratio), conductivity increased dramatically by five orders of magnitude after 0.5 h of annealing and increased further by nearly two orders of magnitude after another 0.5 h annealing. Smaller increments were observed for nanocomposites containing 3.5 and 4.5 wt% GNP-S, while composites became non-conductive again when the entire filler content (5 wt%) was made up of GNP-S. Such changes from insulator to conductor to again insulator with increasing GNP-S content is indicative of significant synergistic effects between small and large nanofillers and suggests that GNP-S is mainly responsible for creating the conductive network through

dynamic percolation while a minimum GNP-L content is required for the initial filler framework through which a conductive network can form after annealing. Meaning that, while a critical amount of GNP-S is needed for dynamic percolation, a small amount of GNP-L is still required to reduce the inter-particle distances further to form a conductive network. This also explains why the system based solely on 5 wt% GNP-S remains non-conductive even after 1 h annealing.

4.3.2 Real-time monitoring of conductivity

To further investigate the dynamic percolation behaviour of PLA/GNP composites based on either 5 wt% GNP-S, 5 wt% GNP-L and 5 wt% 50/50 hybrids, real-time measurements of conductivity were conducted on selected samples and results are presented in Figure 4.3. All three PLA nanocomposite samples start to show an increase in conductivity at around the glass transition temperature of PLA (T_g = 76 °C), and follow the same linear temperature dependent electrical conductivity trend until a temperature of around 140 °C (close to T_m = 167 °C). However, above this temperature, the GNP-$S_{2.5}$/GNP-$L_{2.5}$ hybrid nanofiller system showed a strong additional increase in conductivity, reaching a high constant conductivity value in the melt at a temperature of around 180 °C.

The two distinct stages in the temperature dependence of the electrical conductivity of the hybrid nanofiller based composite suggests that in this system a secondary conduction mechanism is active, which results in a strong increase in conductivity of this nanocomposite system. During heating from RT to just below T_m, the measured electrical conductivity is solely dependent on the temperature dependence of the electrical conductivity [63,292] for all three nanocomposite systems. However, close to or above the PLA melting temperature, the GNP-S in the hybrid system gains mobility and reorganises itself into a reagglomerated network, leading to an increase in electrical conductivity for the PLA/GNP-$S_{2.5}$/GNP-$L_{2.5}$ hybrid system as a result of dynamic percolation. On the other hand, nanoparticle migration is less obvious for GNP-L as these nanoparticles exhibit less mobility and as a result conductivity changes little for PLA/GNP-L_5 for the same annealing time. Similarly, composites based solely on GNP-S also did not show a secondary increase in conductivity above T_m but here the absence of dynamic percolation is due to the low aspect ratio of GNP-S, preventing this system from forming a conductive network.

After heating is removed, conductivity of all three nanocomposites decreases instantaneously. Interestingly, both the PLA/GNP-S_5 and PLA/GNP-L_5 systems lose nearly all their conductivity after cooling to RT, while the hybrid PLA/GNP-$S_{2.5}$/GNP-$L_{2.5}$ system maintains a high level of conductivity even after cooling. These differences are a strong indication that the increase in conductivity for the hybrid nanofiller system during heating is the result of a reorganization of the nanofiller network, which remains present after cooling to RT and results in sustained high electrical properties. Nanocomposites solely based on either small- or large GNP nanofillers did not show this dynamic network formation and temperature dependent conductivity is lost upon cooling to RT. Please note that heating conditions for PLA/GNP-S_5 in Figure 4.2 are different from those in Figure 4.3 so the data are not directly comparable.

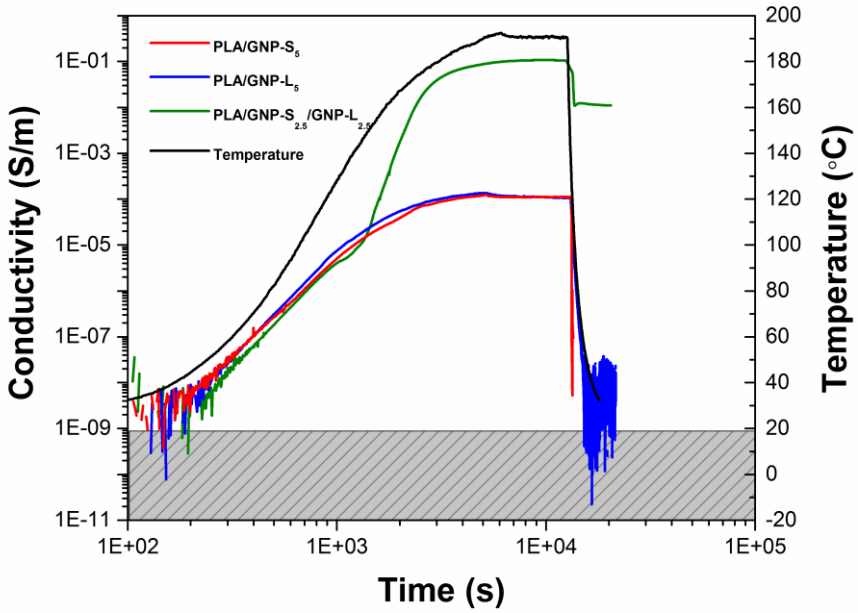

Figure 4.3. Real-time electrical conductivity measurements, showing the time dependence of the electrical properties of PLA/GNP composites when subjected to a temperature scan. Nanocomposites based on hybrid small- and large GNPs showed a secondary increase in electrical conductivity around the polymer melting temperature, indicating a dynamic network formation and electrical properties which are mostly maintained after cooling to RT. Red: PLA/GNP-S_5, Blue: PLA/GNP-L_5, Green: PLA/GNP-$S_{2.5}$/GNP-$L_{2.5}$, Black: Temperature scan. Shaded grey area represents the non-measureable conductivity range.

4.3.3 Mechanisms of conductivity change during annealing

Here we introduce a simple model to explain the conductivity change at different heating stages for the PLA/GNP composites. The overall conductivity of the PLA/GNP composites, $\sigma(f)$, can be expressed as:

$$\sigma\,(f) = \sigma(T) + \sigma\,(reaggr) \tag{4.2}$$

Where $\sigma(T)$ is the temperature-dependent conductivity of the composites and $\sigma\,(reaggr)$ is the agglomeration-induced network controlled conductivity of the composites. The electrical conductivity of most materials changes with temperature. If the temperature T does not vary too much, a linear approximation is typically expected:

$$\sigma(T) \propto \ (\mathrm{T} - \mathrm{T}_0) \tag{4.3}$$

In the first heating stage from RT to around 140 °C (below T_m = 167 °C), the temperature induced conductivity is dominant for all three composites as the polymer is still in the solid state and no major reorganization of GNPs in the polymer matrix can occur. This explains the initial linear increase in conductivity with time during heating as seen in Figure 4.3. However, after reaching the PLA melting temperature, the small nanoparticles in particular start to migrate and rearrange themselves, creating new conductive pathways. The driving force for such reconnection is the thermodynamic processes that minimize free energy. For a given volume of GNPs in the matrix, well dispersed GNPs will have a much higher surface/volume ratio compared to that of GNP agglomerations. During annealing, small GNPs gain mobility through heating and reconnects to each other to minimize the overall surface area. This phenomenon results in an additional contribution of this reagglomerated network to the overall electrical conductivity and is observed through a change in slope of the conductivity versus time curve for the PLA/GNP-$S_{2.5}$/GNP-$L_{2.5}$ hybrid composites as shown in Figure 4.3. On the other hand, temperature-induced conductivity remains dominant for both PLA/GNP-S_5 and PLA/GNP-L_5 composites as here the nanofillers display little connectivity due to either their limited aspect ratio or their inability to migrate with no additional contribution of the reagglomerated network to the total conductivity. When heating is removed, both PLA/GNP-S_5 and PLA/GNP-L_5 composites become non-conductive again after cooling down to RT. This observation supports our hypothesis that the measured increase in conductivity during

heating of this system is entirely the result of temperature dependent conductivity. Alternatively, the hybrid system maintains a high level of conductivity after cooling to RT. This is a clear indication that the overall conductivity level measured during heating of this system can be attributed to a combined temperature dependent electrical conductivity component together with a network component.

4.3.4 Morphology of composites before and after annealing

To further investigate the potential mechanism for increased conductivity after annealing, SEM images were taken for composites before and after annealing as in Figure 4.4. For PLA/GNP-S, little information was revealed regarding the change of the distance between GNPs, possibly due to the size of GNP-S is relatively small thus the movement of GNP-S could not be observed under SEM. For PLA/GNP-S/GNP-L, the distance between GNP-L hardly changed after annealing under SEM as well. Thus the increased connectivity in the hybrid system could be only attributed to subtle movement of GNP-S, which could not be observed under SEM as well as in the case of PLA/GNP-S.

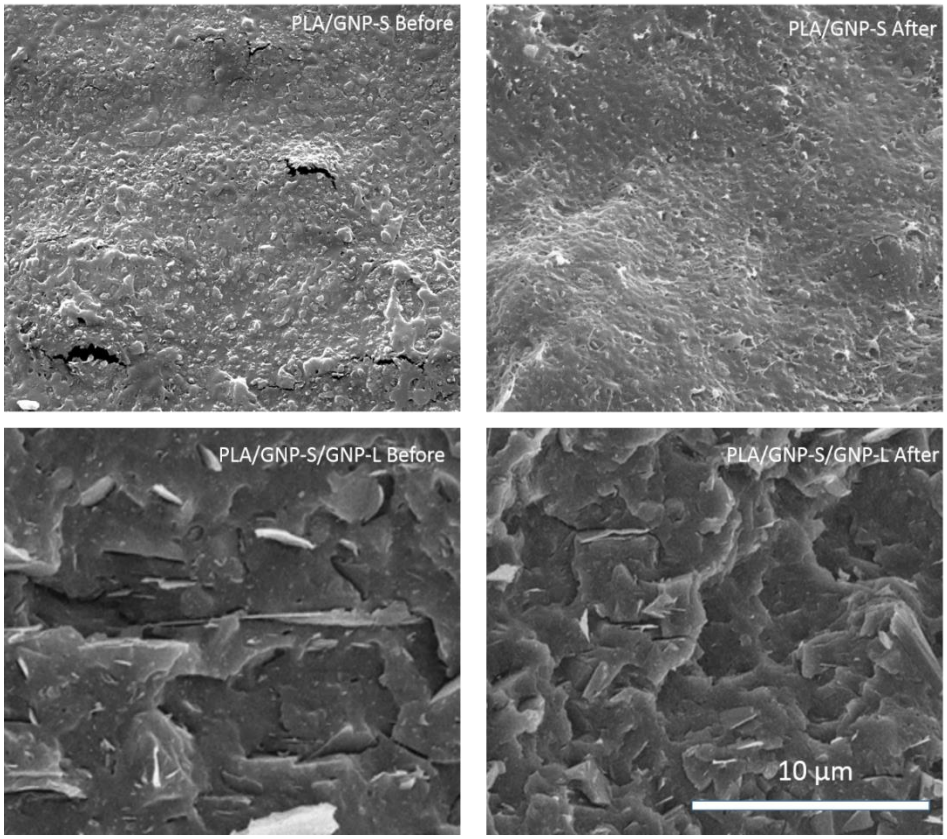

Figure 4.4. SEM images of PLA/GNP-S/GNP-L composites along the measured electrical conductivity direction before and after annealing.

4.3.5 Rheology of nanofiller networks

It is believed that the recovery of conductivity in GNP based nanocomposites after annealing is due to the re-establishment of connections between nanoparticles that were initially lost during shear mixing. Dynamic rheology of samples before and after annealing is a powerful tool to establish a link between electrical conductivity and composite morphology. Measurements of the in-phase shear modulus G' as a function of frequency is a sensitive tool to characterize the formation of a network by nanoparticles in a polymer melt. The presence of such a network manifests itself as a plateau in the G' at low frequencies, of which the magnitude of this G' plateau is known to correlate with the number of connections in the network (the network density) [293].

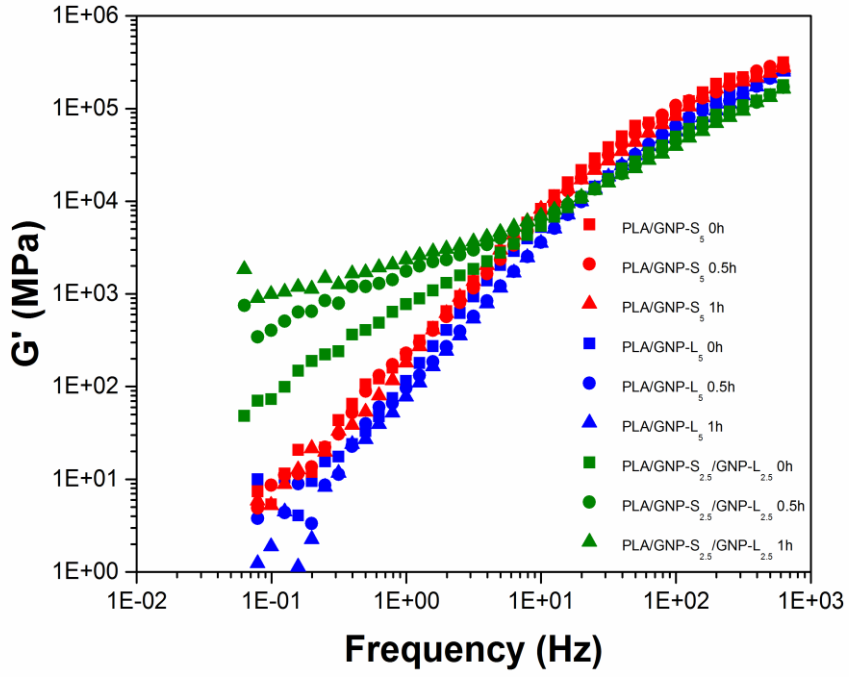

Figure 4.5. G' as a function of frequency for PLA/GNP-S (Red), PLA/GNP-L (Blue) and hybrid nanofiller systems (Green) after 0 h (Square), 0.5 h (Circle) and 1 h (Triangle) of thermal annealing. A clear plateau for G' was only observed for the hybrid filler system after 1 h of annealing, indicating the presence of a filler network.

Figure 4.5 shows frequency sweeps at 180 °C for selected PLA/GNP samples before and after annealing for different periods of time. The results are particularly notable for the PLA/GNP-$S_{2.5}$/GNP-$L_{2.5}$ hybrid samples. For these systems, G' levels off significantly at low frequency finally reaching a plateau value at low frequencies after 1 h annealing, suggesting typical solid-

like behaviour of the nanocomposite melt as a result of the established network of filler–filler contacts. This indicates that a particulate network was formed for this nanocomposite system after 1 h of annealing. This further supports our hypothesis that GNP-L acts as the backbone of the network, while GNP-S acts as mobile branches filling the voids, leading to a higher network density. PLA/GNP-S_5 and PLA/GNP-L_5, on the other hand, did not show a low-frequency plateau in its G'. In fact, G' hardly changed after 0.5 h and 1 h annealing for both systems. This is in agreement with our previous discussion and indicates that the network connectivity in these formulations remains unchanged and explains why annealing did not alter the conductivity for this system. Notably, Figure 4.5 suggest a stronger rheological network when GNP of different size are used particularly after annealing. But this is not necessarily the consequence of a better distribution. A better particle distribution would be evidenced by a decrease in electrical properties, which is the opposite of what shown in Figure 4.1, for instance.

4.3.6 Nanofiller mobility and influence of filler size

It is worth considering how or why annealing can re-organise nanoparticles into an interconnected state. Randomization of nano-scale hard disks can be governed by either Brownian motions of particles [294], or non-Brownian interactions [295–298]. First, we will consider Brownian motion of particles. Rotational diffusivity D_r of a circular Brownian disk with a diameter d in a medium with a viscosity η at temperature T can be expressed as [299,300]:

$$D_r = \frac{3kT}{4\eta d^3} \tag{4.4}$$

Given the same temperature, at dilute or semi-dilute concentrations, the ratio of displacement between small and large GNPs can be derived as

$$\frac{D_L}{D_S} \sim \frac{d_S^3}{d_L^3} \tag{4.5}$$

Based on this consideration, small GNP-S (d_s = *1.2 µm*) are expected to display nearly 1600 times larger displacements than large GNP-L (d_L = *14 µm*) under the same conditions. Such a huge difference in GNP mobility explains why annealing is much more effective for small GNPs than for large GNPs. Next, we may also consider non-Brownian interactions. Apart from limited translational and rotational diffusion dominated by Brownian motions, particles may

still be able to reorient, even under non-Brownian conditions due to the viscoelastic nature of the polymer matrix following Arrhenius like-behaviour [301]:

$$\eta_0 = c\ exp\ (\frac{\Delta E}{RT}) \tag{4.6}$$

Where T is temperature, R is the ideal gas constant, ΔE is an activation energy, and c is a constant. ΔE implies a fillers resistance to reorientation and can be obtained by fitting the data at different temperatures using Equation (4.6). It has been reported that longer carbon nanotubes tend to have a higher ΔE thus requiring more energy to reorient [301]. In other words, they need higher annealing temperatures and/or longer annealing times. This also explains why PLA composites incorporating small GNP-S fillers are more affected by annealing as a lower activation energy is required for dynamic percolation in this system. Further experiments to quantify this effect will be designed in the future to validate such a hypothesis.

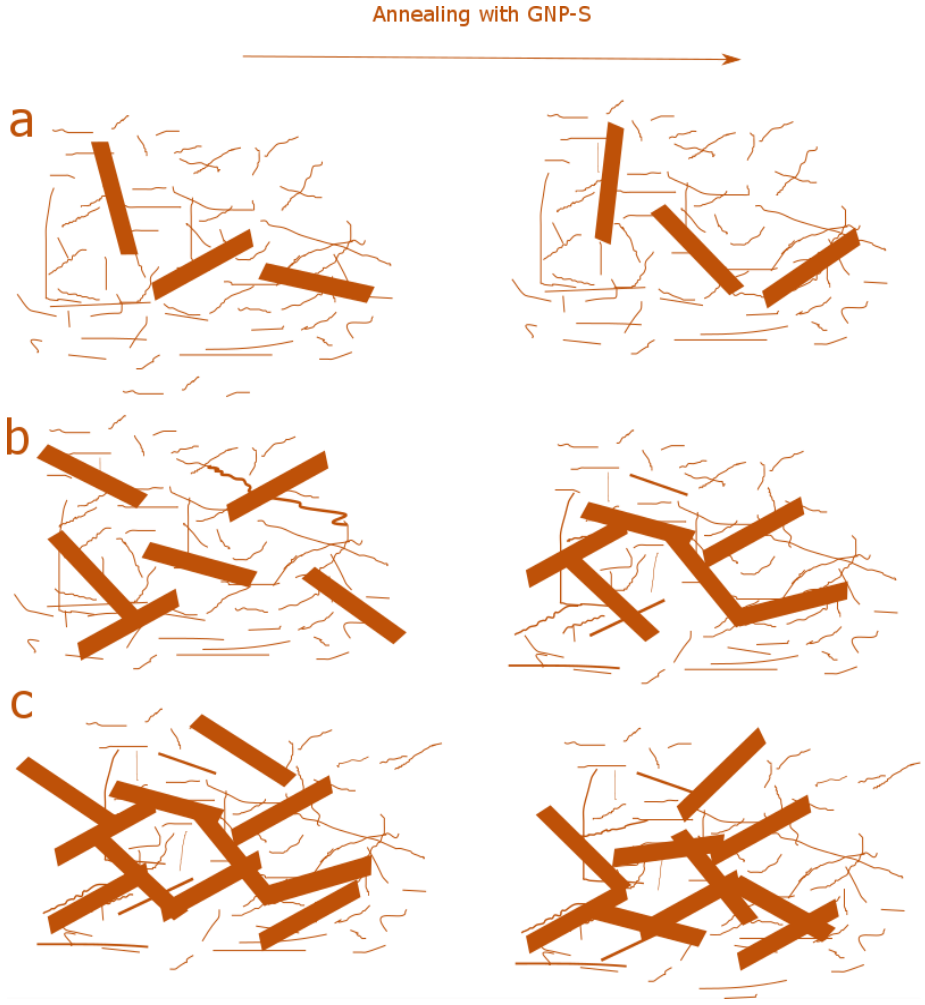

Figure 4.6. Reorientation mechanisms during annealing for GNP-S in a: (a) dilute (5 wt%), (b) semi-dilute (7-10 wt%) and (c) concentrated regime (15 wt%). Increased connectivity through annealing can only be achieved within the semi-dilute regime.

It should be noted that our data (Figure 4.1 and Figure 4.2) indicates that only systems with semi-dilute GNP-S filler concentrations show dynamic percolation and filler network formation after annealing. Similar differences caused by filler concentration were also observed by Kim et al. [111] and are schematically depicted in Figure 4.6. At very dilute concentrations, even complete randomization of GNP-S will not result in particle-particle contacts since their spheres of rotation do not intersect as indicated in Figure 4.6 (a). This explains the unchanged conductivity for composites incorporating 5 wt% GNP-S as shown in Figure 4.1, as the number of particles is not high enough to create a percolating network. When the particle loading increases (Figure 4.6 (b)), platelets will be sufficiently close to each other and can more easily form a conductive network after rotational relaxation via direct particle-particle contacts or electron hopping conduction. Here annealing leads to the creation of a nanofiller network, which gives rise to the increased in-phase shear modulus G' and electrical conductivity for PLA/GNP-S composites with intermediate filler loadings (7 wt% and 10 wt% GNP-S). However, in the concentrated regime (Figure 4.6 (c)), isotropic (re)orientation cannot take place due to excluded volume interactions between particles, hence leading to limited changes in conductivity upon annealing. This is illustrated by the fact that electrical conductivity of composited based on 15 wt% GNP-S remains unchanged even after 1 h of annealing.

4.4 Conclusions

In this study, we have shown that smaller GNP nanoparticles exhibit a much greater ability to form a conductive filler network by dynamic percolation during thermal annealing than larger nanoparticles.

This network forming ability of small GNPs in a polymer melt could be particularly exploited when hybridized with large GNPs, leading to significant synergistic effects in electrical properties of the resulting PLA nanocomposites. Electrical conductivity of hybrid nanocomposites incorporating both GNP-S and GNP-L nanofillers was greatly improved by thermal annealing at elevated temperatures, while those of composites solely based on similar amounts of GNP-S and particular GNP-L remained largely unchanged under the same annealing conditions.

Similarly, rheological properties, specifically the in-plane shear modulus G' at low frequencies, increased with annealing for nanocomposites incorporating hybrid nanofillers suggesting network formation. The microstructural basis for these observations is that initially filler-filler contacts are lost due to the high shear forces during compounding and that these can be re-established, albeit through a different network morphology, during thermal annealing in the melt, leading to greatly improved electrical properties as a result of dynamic percolation.

The results presented in this study have significant practical relevance for the large-scale manufacture of conductive polymer nanocomposites as it provides guidelines of how to achieve good electrical properties at low filler loadings.

Chapter 5 - Multilayer coextrusion of PLA/GNP nanocomposites with enhanced structural organization and properties

5.1 Introduction

Traditional man-made nanocomposites, as produced by melt-mixing, solution casting or in-situ polymerization, have generally a relatively low reinforcing efficiency because of the difficulty to create nanocomposites which display homogeneous dispersions of nanoparticles, good interfacial interactions between particles and matrix, and finally high levels of structural organisation of 1D or 2D nanoparticles within the matrix [2]. On the contrary, bio-composites such as bones, teeth, or nacre are also composed of mineral 1D or 2D particles together with a protein matrix but show superior strength and toughness. Common features in such bio-composites are their complex architectures and hierarchical organisation at different length scales, involving the arrangement and orientation of high aspect ratio particles with the smallest building blocks often being at the nanoscale [1,302,303].

Recently, highly organized nanocomposites mimicking the structure of nacre have been reported [304], using a large number of technologies including layer-by-layer (LBL) assembly [305,306] , LBL spraying [275,307], vacuum or solution casting [308–310], and freeze-casting [311,312]. Although many of these techniques have been extremely successful in terms of introducing structural control in composites based on 2D nanoplatelets, all these techniques are based on solution- or colloidal type processes rather than melt-processing as used preferably by the polymer industry.

Santagiuliana et al. [313] recently showed that a melt-process inspired by the art of croissant making using the Baker's transformation [314] results in layered polymer nanocomposites with controllable and quantifiable dispersions of GNPs and efficient mechanical reinforcement effects. In their work the Baker's transformation was performed manually using a repetitive pressing and folding process, which limits its applicability in an industrial environment. Static mixers or multipliers on the other hand have been used for industrial-scale multilayer co-extrusion of different polymers using the Baker's transformation principle [219,220,222,315,316] as reviewed in Chapter 2.

In this chapter we will use forced assembled multilayer co-extrusion as a processing methodology to disperse and orient GNPs in multi-layered PLA nanocomposite films. In order to avoid layer break-up, symmetric as well as asymmetric alternating layers were used. The study provides as further understanding of nanoplatelet reinforcing mechanisms through quantification of the GNP alignment directly through imaging, while indirect methods are used to further quantify the effect of filler orientation in the films including mechanical property characterization and water vapour permeability.

5.2 Experimental

5.2.1 Materials

Poly(lactide acid) (PLA) 2002D and 4032D from NatureWorks Co. Ltd. (USA) were purchased from Resinex, UK. Both semi-crystalline PLAs are extrusion grades with different D-lactic monomer contents, ~4% for 2002D and ~2% for 4032D respectively [317–320], and weight average molecular weights, 212 and 207 kDa respectively [321]. They have similar properties including glass transition temperature of ~60 and 61 °C, crystallinity of ~1% and 2% and tensile

modulus of ~3.5 GPa respectively [317,318,322]. Graphite nanoplatelets (xGNP-M15) were used as described in previous chapters. All materials were dried overnight in an oven at 80 °C before processing.

5.2.2 Sample preparation

PLA/GNP masterbatch

Both polymer and GNPs were dried in the oven at 90 °C overnight before compounding. A twin-screw extruder (Dr. Collin Laboratory Twin-Screw Kneader ZK 25 x 40, Germany) was used to create a 20 wt% xGNP-M15/PLA-2003D masterbatch using the following temperature profile (from Zone 1 to Zone 6: 185, 210, 200, 190, 185, 180 ℃). A screw speed of 140 rpm was used to disperse the GNPs in the polymer matrix. This masterbatch was further diluted to 5 wt% with neat PLA -4032D using the same processing conditions.

Multilayer PLA/GNP films

Multilayer co-extrusion involves a primary polymer melt A (PLA) and a secondary polymer melt B (PLA + 5 wt% GNP), which were extruded from two single-screw extruders (Dr. Collin TEACH-LINE® E 20T, Germany) respectively, combined in a bi-layer (AB) co-extrusion feed block. In this study, the throughput was controlled by varying the speed of the individual extruders A and B to produced layered structures with different B:A (filled:unfilled) layer distributions (50%:50%; 20%:80%; 10%:90%). Thus the final total concentration of graphene in the films was diluted to 2.5, 1 and 0.5 wt% for samples marked as 50:50, 20:80 and 10:90. Neat PLA and monolayer composites of PLA + 5 wt% GNPs were also produced using the same single-screw extruders for comparison, marked as PLA and Mono respectively. The double layer co-extrusion feed block is connected to a series of static mixing elements or multipliers that use a process of vertical slicing, biaxial stretching and recombining as schematically depicted in Figure 5.1 to produce 2^{n+1} layers (n being the number of static mixing elements). In this study, 6 mixing elements were used, giving a total of 128 layers. This melt is then extruded through a flat film die onto chill rolls with a temperature of 60 °C. The two single-screw extruders, static mixing elements and die were all set at a temperature of 190 °C. This resulted in multilayer films made up of alternating layers of neat PLA and PLA + 5 wt% GNP.

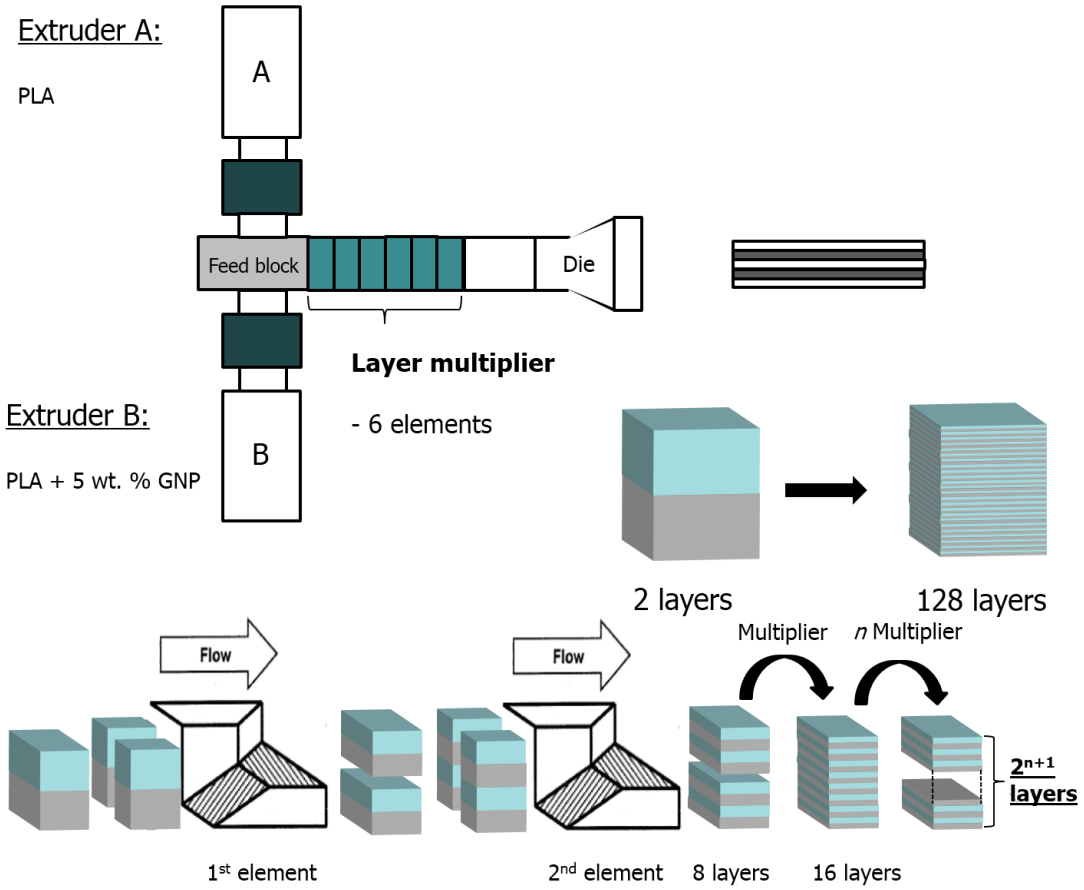

Figure 5.1. Schematic of the forced assembly multilayer co-extrusion process for the production of multi-layered polymer films with alternating layers of PLA and PLA + GNP. Adapted from [219].

5.2.3 Characterization

Transmission optical microscopy (OM) was performed using an Olympus BH2 microscope, equipped with a digital camera allowing the capturing of images that were processed using Image J analysis software (National Institutes of Health, USA). Samples were prepared using a Leica RM 2225 microtome and were cut perpendicular to the extrusion direction.

The dispersion and morphological features of the nanocomposites were characterized using a FEI Inspect-F scanning electron microscope (SEM) at an accelerating voltage of 10 kV. All specimens were prepared by cryogenic fracturing the composite films using liquid nitrogen. Fracture surfaces were gold sputtered before analysis.

X-ray diffraction (XRD) analysis was performed on a Siemens D5000 Diffractometer using Cu (Kα) radiation (wavelength: 1.54 Å) at room temperature (RT) in the range of 2θ = 5° to 40° at a scanning rate of 20 min^{-1}.

Tensile tests were performed using an Instron 5586 at RT, equipped with a 1 kN load cell. Samples were cut in dumbbell shapes according to ASTM 638, Type V and tested and tested at a rate of 10 mm/min according to ASTM 638 procedures. Reported values were calculated as averages over five specimens.

Dynamic mechanical analysis (DMA) spectra were obtained with a TA Instruments DMA Q800. Samples were tested in film tension mode. A frequency of 1 Hz with a temperature ramp of 3 °C/min from RT to 150 °C was employed. Results were averaged over three test samples.

Differential scanning calorimetry (DSC) was performed using a Mettler-Toledo 822e to investigate the thermal properties of the nanocomposites. All samples were heated to 200 °C at a rate of 10 °C/min. Crystallinity was determined using the heat of fusion of 100% crystalline PLA taken as 93.6 J/g [185].

The water vapour permeability of the multilayer films was investigated, in accordance with the ASTM E96 and DIN 53122 gravimetric method, using Elcometer 5100 Payne Permeability Cups (Part Number K0005100M201, Elcometer Ltd.). Distilled water was placed inside the round cup to expose the film, with an exposed area of 10 cm^2, to the environment. Once the films were secured, each cup was placed in an oven at 40 °C. The cups were weighed periodically using a precision scale (± 0.0001 g).

5.3 Results and Discussion

5.3.1 Nanofiller dispersion

Optical microscopy

Multilayer co-extrusion was used to produce polymer composite films with 128 alternating layers. A reduction in thickness of the nanocomposite layers should provide the geometric constraints to align 2D fillers like GNPs. Micro-scale characterization of the morphology of the multilayer films was carried out using optical microscopy and the dispersion of the GNPs in films with different filled:unfilled ratios are compared in *Figure 5.2*. A random distribution of GNPs in a PLA matrix is visible in the mono-extruded composite film with 5 wt% GNP and a layered structure is not present. On the contrary, boundaries between the pure PLA layers and the PLA/GNP layers were evident for the 50:50, 20:80, and 10:90 systems. This demonstrated that multilayer films with alternating filled and unfilled PLA layers were produced. Notably, some agglomerations of GNPs is visible for all compositions. This may be cause by the fact that the 5 wt% GNP loading used in this study is rather high compared to most studies although this phenomenon was also reported by Li et al. for PMMA/GNP films of 1024 layers and 0.5wt% GNP [234].

To quantify the dispersion of the GNPs, the fraction R of the total agglomerates with diameter > 5 µm (area > 19.6 μm^2) over the total area of the sample was calculated following the work of Alig et al. [323] and results are summarized in Table 5.1. It is observed that the fraction R of large agglomerates decreases significantly with a decrease of the filled PLA/GNP layer thickness. However, R values were generally greater than those obtained by Li et al. [234], possibly due to the use of fewer multiplier dies and the significantly higher filler content used.

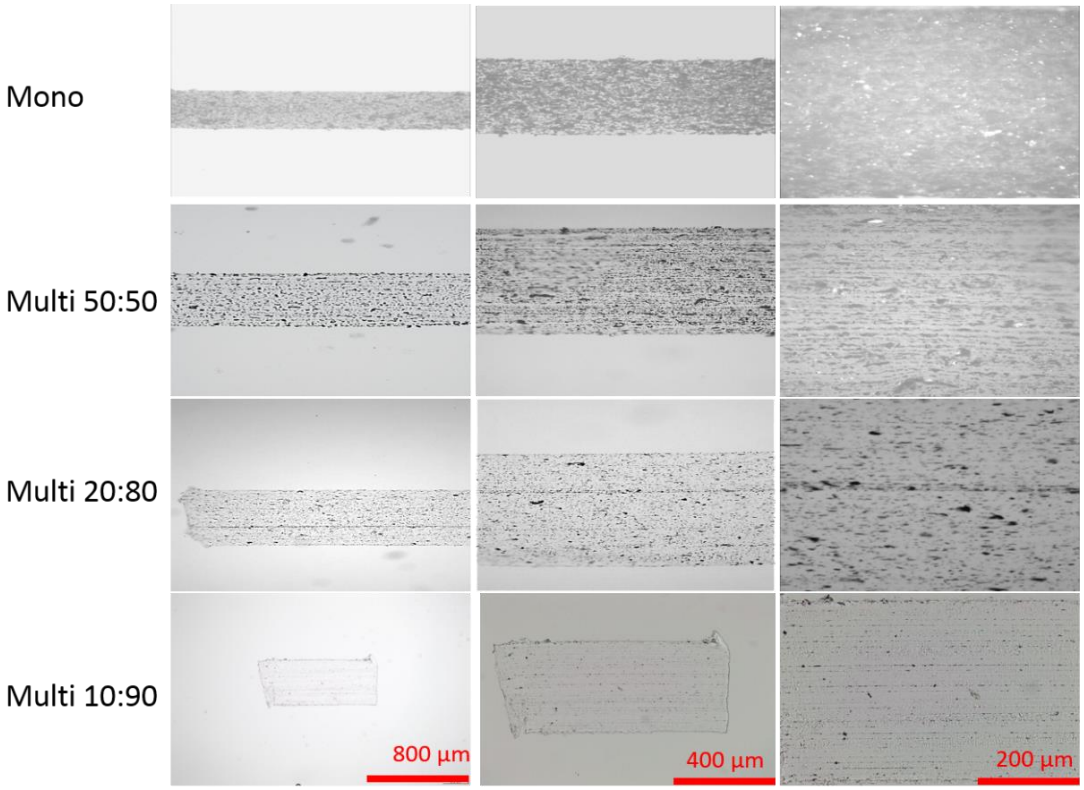

Figure 5.2. Cross-sections of mono- and multilayer PLA/GNP composite films with different filled:unfilled ratios along the extrusion direction under optical microscopy and different magnification. The total GNP content in the films is 5, 2.5, 1 and 0.5 wt%, respectively.

Table 5.1. Fraction (R) of large agglomerates calculated for the different nanocomposite films.

	Mono	**Multi 50:50**	**Multi 20:80**	**Multi 10:90**
GNP (wt%)	5	2.5	1	0.5
Filled layer (%)	100	50	20	10
Unfilled layer (%)	0	50	80	90
R (%)	48	24	15	7

Scanning electron microscopy

SEM was used to further investigate the dispersion and orientation of the GNP fillers in the multilayer films as shown in *Figure 5.3*. For the monolayer PLA film incorporating 5 wt% GNP, many platelets displayed a random distribution in the polymer matrix, with distortion

and agglomeration seen for most flakes. Although a significant fraction of GNP flakes were oriented as a result of flow during the extrusion process, some randomized orientation of large GNP flakes could still be observed. On the contrary, for all multilayer systems, the GNP filled layers were well confined by the neighbouring neat PLA layers with most of the graphene flakes showing planar orientation in these GNP filled layers. In addition, most GNPs appeared to be much thinner, potentially indicating improved dispersion or even exfoliation during multiplying. The degree of alignment and thickness reduction of the GNPs will be further evaluated more quantitatively through image processing and XRD analysis in the next section.

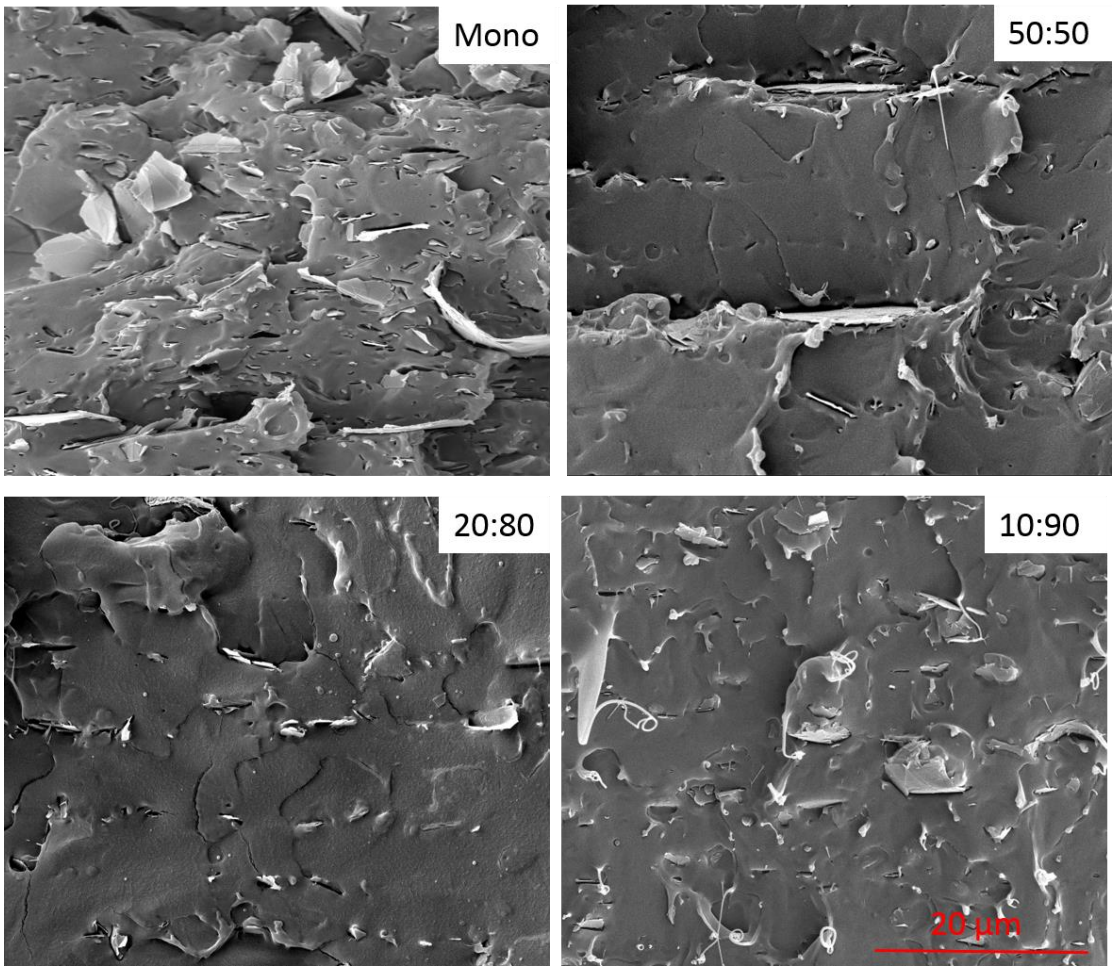

Figure 5.3. SEM images of cross sections of mono- and multilayer PLA/GNP composite films with different filled:unfilled ratios. The total GNP content in the films was 5, 2.5, 1 and 0.5 wt%, respectively.

Nanofiller alignment and dimensions

To quantify the degree of alignment or orientation, the SEM images from *Figure 5.3* were analysed using Image J software and histograms of GNP orientation and average platelet lengths were obtained from at least 100 flakes (Figure 5.4). Orientation of GNPs in the monolayer extruded film revealed a wider distribution while multilayer films showed a more narrow distribution of GNP orientations, implying preferential alignment of the platelets. Moreover, multilayer films with thinner PLA/GNP layers showed better nanofiller alignment, suggesting that these thinner layers induce more constraints on the orientation of the GNPs than thicker layers.

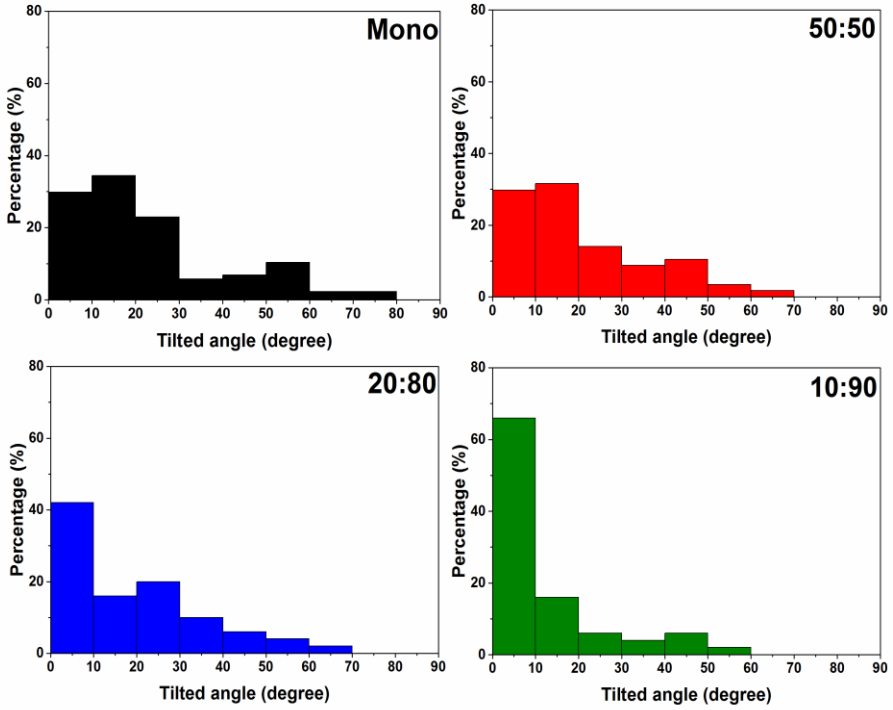

Figure 5.4. Histograms of nanoplatelet orientation in mono- and multilayer PLA/GNP composite films with different filled:unfilled ratios.

Average diameters (d) of GNPs were analysed using Image J software and summarized in Table 5.2. The average platelet diameter (or length) was reduced from 4.1 µm for monolayer films and 50:50 multilayer films to 3.0 and 2.5 µm for 20:80 and 10:90 multilayer films. At the same time the platelets became more uniform in size as indicated by the reduced spread of data.

This agrees with our previous findings in Chapter 3 that GNPs become thinner as well as smaller after extrusion compounding processes [324].

X-ray diffraction

To obtain more quantitative information concerning the size and orientation of the nanoplatelets X-ray diffraction (XRD) was performed. XRD can provide information with regards to the stacking thickness of the GNP crystallites and here the average out-of-plane crystallite thickness of the GNPs (t) was estimated using the Scherrer equation in Chapter 3 and results were summarized in Table 5.2.

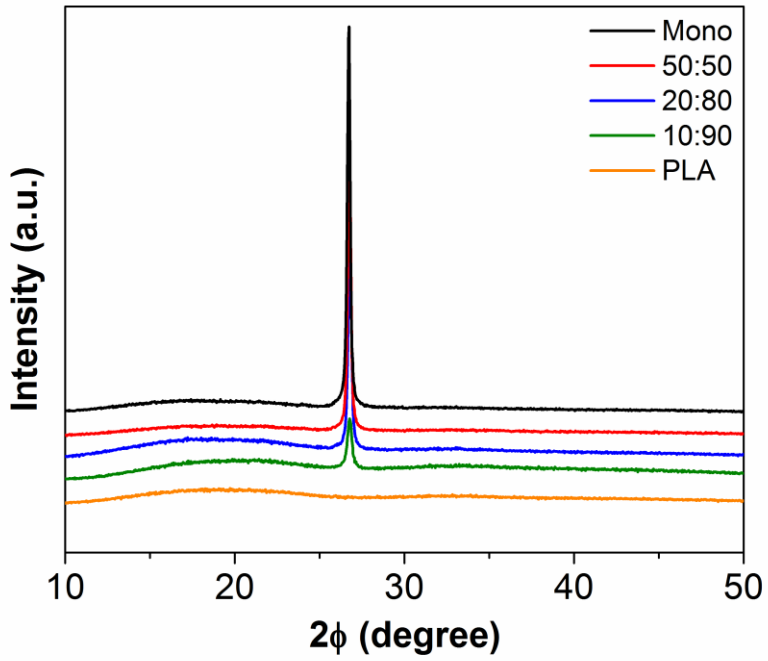

Figure 5.5. X-ray diffraction (XRD) patterns of mono- and multilayer PLA/GNP composite films with different filled:unfilled ratios, showing structural changes in the composites with different filler ratios.

Table 5.2. Average platelet diameter (d) from SEM and thickness (t) from XRD together with calculated aspect ratios (AR), Young's modulus of composites film (E_c) and filled layer (E_{filled}) from tensile tests together with back-calculated platelet orientation factor (η_0).

	PLA	Mono	Multi 50:50	Multi 20:80	Multi 10:90
GNP (wt%)	0	5	2.5	1	0.5
d (µm)	N/A	4.1 ± 2.1	4.1 ± 2.3	3.0 ± 1.8	2.5 ± 1.4
t (nm)	N/A	40.3	34.5	34.5	20.1
AR (-)	N/A	50-155	50-185	35-140	50-195
E_c (MPa)	2551 ± 80	3215 ± 98	2860 ± 32	3100 ± 72	2890 ± 15
E_{filled} (MPa)	N/A	3215	3229	5160	5680
η_0	N/A	0.16	0.18	0.72	0.86

In the monolayer extruded PLA/GNP films, the average thickness of the GNPs was approximately 40 nm, which is in accordance with our previous reported data for PLA nanocomposites incorporating 5 wt% GNP through micro-compounding [324], but significantly larger than the values provided by the manufacturer (t ≈ 7 nm). However, GNP layer thickness decreased to around 35 nm in the 50:50 and 20:80 multilayer nanocomposite films, which could be attributed to delamination of the GNP during the slicing and stretching process by the static mixers. This value was further reduced to 20 nm in the 10:90 multilayer films. This indicated that multilayer co-extrusion has an additional benefit of reducing the filler thickness during processing. Based on the SEM and XRD data, the aspect ratios (AR = diameter/thickness) of the GNPs were estimated and listed in Table 5.2. In the next section these values of aspect ratio will be used to estimate the filler orientation factor. The aspect ratio of the fillers remained in the 50 to 200 region for all composite systems, which is an indication that besides delamination also fracture of the platelets takes place.

5.3.2 Mechanical properties

From the SEM images we can see that the forced assembly co-extrusion method to some extent succeeds in aligning the GNPs in the plane of the layers. Therefore, we may expect to see an increase in effective mechanical reinforcement for these nanocomposites. Table 5.2 gives a summary of basic mechanical properties of the composite films (E_c). In case of equal effective reinforcement by the GNPs one would expect to see a gradual decrease in Young's modulus of the composite films with decreasing filler content. Interestingly, the 20:80

multilayer composite films exhibited a similar modulus to the monolayer composites but at a five times lower overall GNP loading, demonstrating improved reinforcing efficiency for GNPs embedded in thinner and more confined nanocomposite layers. This is in agreement with SEM observations that showed better alignment for the 20:80 system compared to monolayers. Multilayer nanocomposite films with a 10:90 composition have a slightly lower modulus than monolayer PLA/GNP films as they contain only 1/10 of filler loading. However, also here the relatively high mechanical properties of these films are indicative of a high GNP reinforcing efficiency in these films.

The effective reinforcement (E_c/E_m) of the various composite films is presented in Figure 5.6 along with data from literature. For the monolayer PLA/GNP film, a reinforcement of 126% is presented, similar to previous results (123%) for micro-compounded PLA/GNP composites as reported in Chapter 3. For the multilayer systems, the results reveal a modest reinforcement of 107% for the 50:50 films, 120% for the 20:80 films and again 107% for the 10:90 films (see Figure 5.6). A mechanical reinforcement of 120% at 1 wt% GNP is among the highest reported for PLA/GNP composites through melt extrusion, and close to that of PLA/exfoliated graphite composites reported by Kim et al. [74].

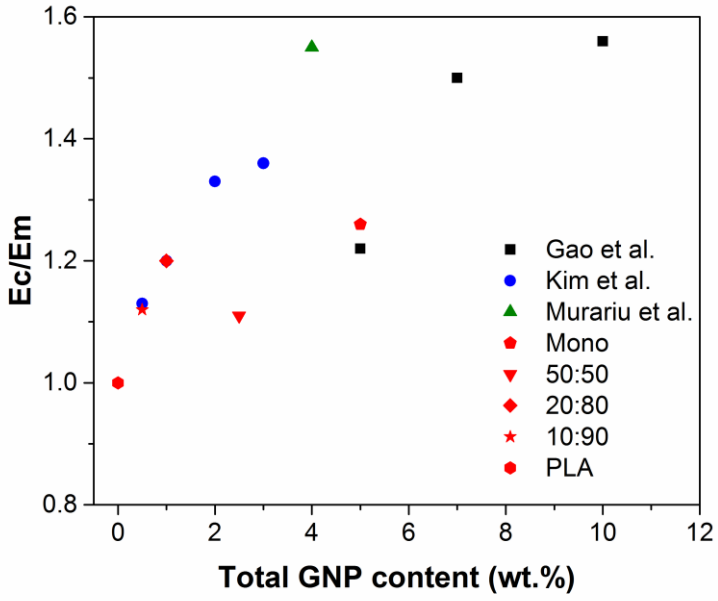

Figure 5.6. Effective composite reinforcement (E_c/E_m) as a function of GNP loading measured by tensile tests along the extrusion flow direction as a function of overall GNP content, together with literature data. Red: data from this research, Black: Gao et al. [324], Blue: Kim et al. [74], Green: Murariu et al. [196].

Reinforcing efficiency in a single layer

For a more detailed analysis of the reinforcing efficiency of the GNPs we analysed the mechanical data on the basis of properties of the graphene-filled layers only. Examination of the reinforcement by GNP in a single PLA/GNP layer, and a comparison with micromechanical predictions assuming full alignment of the nanoplatelets, provides us with insight into the ability of the forced assembly co-extrusion method to orient GNPs. This is particularly relevant if one could eventually make multilayer nanocomposite systems in which all layers are of nanometer thickness and reinforced by graphene. The tensile modulus (E_{filled}) of a single layer of graphene filled PLA can be estimated using Equation (5.1) which corresponds to the Voigt upper bound rule of mixture [325],

$$E_{filled} = \frac{E - V_{unfilled} E_m}{V_{unfilled}} \tag{5.1}$$

where $V_{unfilled}$ and V_{filled} are the volume fractions of the unfilled PLA layers and GNP filled PLA layers, respectively.

Mechanical properties of GNP filled layers based on Equation (5.1) are presented in Table 5.2. For the case of 5 wt% GNP in an individual layer, the degree of apparent reinforcement is 120% for 10:90 systems, 91% for 20:80 systems and 13% for 50:50 systems. The 120% increase is similar to the reinforcement reported by Li et al., who reported a 118% increase in modulus in 2049 layers (filled layer thickness of 35 nm) of PMMA/PS/GNP systems with 2 wt% GNP in the filled layers [234]. As this reinforcement was achieved at a filler content of 2 wt% instead of 5 wt% in the current study, the multilayer films produced by Li et al. exhibited an even greater reinforcing efficiency. Less agglomerations and further improved alignment can be expected in their films because of the use of 2049 layers, compared to 128 layers in our study, resulting in much thinner filled layers and even greater confinement of the nanoplatelets.

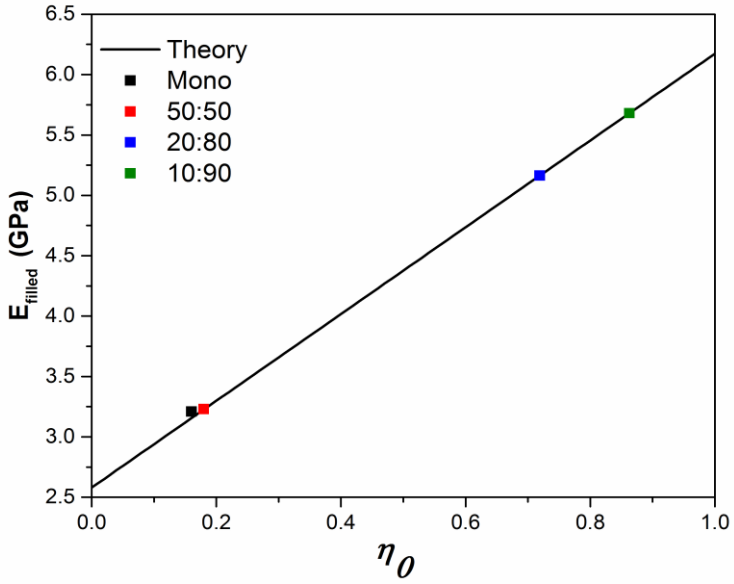

Figure 5.7. Experimental Young's modulus of PLA/GNP composite films as a function of platelet orientation parameter, η_0. Black line: Model prediction using Equation (5.2). Coloured squares: Experimental data.

In order to relate the degree of reinforcement to the degree of orientation, we followed the method developed by Jan et al. [326] using the following equation:

$$E_{filled} = \frac{\eta_o E_f V_f}{\frac{E_f}{\frac{E_m}{\frac{2L}{t}} + 1}} + E_m \qquad (5.2)$$

Where E_m, E_f and E_{filled} are the modulus of the polymer matrix, filler and composites, V_f is the volume fraction of the filler and L/t is the platelet aspect ratio (AR). η_o is the orientation parameter, which lies between 0 and 1, with η_o = 0 representing the case where the platelets are aligned perpendicular to the applied load and η_o = 1 representing the case where the platelets are aligned parallel to the applied load [327,328].

Using E_f= 750 GPa and E_m=2.5 GPa a good fit was found when L/t=30, which is around the lower boundary of the observed aspect ratios as listed in Table 5.2 from SEM and XRD. This results in an orientation parameter of 0.16, 0.18, 0.72 and 0.86 for mono, 50:50, 20:80 and 10:90 multilayer films, respectively and is in agreement with the orientation histograms in Figure 5.4. These results support our hypothesis that the increased effective reinforcement in

20:80 and 10:90 multilayer films is attributed to improved orientation of the GNP fillers. However, it should be noted that the value of 0.16 for monolayer PLA/GNP composites and 0.18 for 50:50 multilayer composites are in fact lower than the 3D random orientation factor of 0.36 as reported by Jan et al. [326]. This might be caused due to GNP agglomerations present in these films as indicated by SEM images (*Figure 5.2*), effectively lowering the reinforcing efficiency of the GNPs in these composites.

5.3.3 Thermal properties

Incorporation of nanofillers in semi-crystalline polymers like PLA can induce both changes in glass transition (T_g) temperature of the amorphous phase as well as an increase in crystallinity due to nucleation effects. Differences in T_g are however rather small for the current PLA/GNP multilayer systems. These results confirm previous findings [324] which also indicated that the addition of GNPs did not significantly alter the T_g of the PLA matrix.

Table 5.3. Glass transition temperatures (T_g) for all PLA/GNP composites as obtained from DMA together with melting temperatures (T_m) and crystallinity (X_c) from DSC and water vapour transmission rate (WVTR) from permeability tests.

Sample	**T_g (°C)**	**T_m (°C)**	**X_c (%)**	**Permeability ($mg*mm/(m^2*d)$)**
PLA	-	166±1	2.0±0.4	8.9±0.4
Mono	78.4	166±1	49.6±1.4	4.8±0.2
Multi 50:50	79.5	167±1	45.8±2.5	4.9±0.3
Multi 20:80	77.8	168±2	46.6±1.7	4.3±0.2
Multi 10:90	-	170±1	46.4±0.3	4.2±0.4

Nanofillers are known to act as nucleating agents in polymer matrices, altering polymer crystallinity in the nanocomposite system and resulting in altered properties [329,330]. Since PLA is a semi-crystalline polymer, its mechanical properties will strongly depend on crystallinity and any observed increase in mechanical properties may therefore not be solely the result of mechanical reinforcement by the nanofillers. In order to evaluate the influence

of polymer crystallinity on mechanical property enhancement of the nanocomposites, DSC was employed to measure the crystallinity of the various PLA/GNP composites as well as that of the neat PLA polymer. DSC results for the different PLA/GNP composites are listed in Table 5.3. The incorporation of 5 wt% GNPs in the monolayer composite films did lead to a significant increase in crystallinity (X_c) from 2% to 47%, which is a common results of the incorporation of GNPs into a PLA matrix [198,331–333]. Interestingly, all multilayer composite films showed similar levels of crystallinity (45% for 50:50, 47% for 20:80 and 46.4% for 10:90) as monolayers films incorporating 5 wt% GNP. Hence, it can be concluded that differences in mechanical performance of the multilayer films originate from improved alignment and hence efficiency of the GNPs rather than an increase in polymer crystallinity as observed in many other studies [276,334,335].

5.3.4 Barrier properties

Average water vapour permeability was calculated using the following equation:

$$P=(\Delta m/T)*t \tag{5.3}$$

Where Δm/T is the steady-state slope obtained from the regression analysis of weight loss (Δm) data vs. time (T), t is the average film thickness. Results from literature on the water vapour permeability of PLA nanocomposites together with data for the current mono- and multilayer composite films are summarised in Table 5.4.

For each study, the maximum % reduction in water vapour permeability (or water vapour transmission rate) compared to the unfilled reference system is recorded, together with the nanofiller concentration. Multi-layered 10:90 films showed among the highest reductions in permeability for any of the investigated nanocomposite systems with a reduction in permeability of 53%, but at only 1/10 of the filler loading necessary for PLA nanocomposites based on nanoclays (see Table 5.4). These results again highlight the potential of the multilayer co-extrusion technology to improve the efficiency of 2D nanofillers in polymer composites.

Table 5.4. Summary of studies on water permeability of PLA nanocomposites from literature, together with the current mono- and multilayer PLA/GNP composite films.

Filler	Max. % reduction in permeability	Ref
Montmorillonite	50% @ 5 wt%	[209]
Cloisite 30B	5% @ 5 wt%	[211]
Cloisite 20A	36% @ 5 wt%	[211]
Cloisite 30B	60% @ 5 wt%	[212]
Montmorillonite	58% @ 5 wt%	[210]
Cloisite 30B	43% @ 6 wt%	[132]
Cellulose	10% @ 1 wt%	[215]
Mono	46% @ 5 wt%	This Research
Multi 50:50	46% @ 2.5 wt%	This Research
Multi 20:80	38% @ 1 wt%	This Research
Multi 10:90	53% @ 0.5 wt%	This Research

Average permeability obtained by monitoring the weight loss as a function of crystallinity and graphene orientation factor are displayed in Figure 5.8 and corresponding data are shown in Table 5.3. The "tortuous path" equation developed by Nielsen [131] is widely used to explain permeability in filled polymer systems. It is believed that a more tortuous diffusion path for gas or water molecules is created when fillers are incorporated in a polymer matrix and the filler concentration, orientation, and aspect ratio have an impact on the efficiency of the filler on permeation. Assuming that the filler platelets are aligned perpendicular to the diffusion direction, the Nielsen model is given by Equation (5.4) below:

$$\frac{P_c}{P_m} = \frac{1 - V_f}{1 + \frac{L}{2t}.V_f} \tag{5.4}$$

where P_c is the permeability of the polymer composite, P_m is the permeability of the unfilled polymer matrix, V_f is the volume fraction of filler, and L/t is the length over thickness or aspect ratio (AR) of the filler.

This model has been used to account for the observed improvements in barrier properties (to both water vapour and gases) of polymer nanocomposites. For example, Choudalakis and Gotsis [336] reviewed a large number of studies on the gas permeability of polymer nanocomposites and discussed a number of models proposed to predict permeability. It was concluded that assuming that the aspect ratio and orientation of the nanofiller particles are known, then the tortuous path model, which is the simplest, is reasonably successful in predicting permeability. More specifically, the Nielsen equation has been recently used to successfully model the water vapour permeability through PLA nanocomposite films in which the aspect ratio of the nanoclay filler was measured at 50 [132].

With the assumption that the PLA crystallites are impermeable filler particles with an aspect ratio of 1 and crystallinity is the filler concentration, the Nielsen equation can be rewritten as in Equation (5.5) in which P is the permeability of the semi-crystalline polymer, P_0 is the permeability of the amorphous polymer, and X_c is the fractional degree of crystallinity.

$$\frac{P}{P_0} = \frac{1 - X_c}{1 + \frac{X_c}{2}} \tag{5.5}$$

Equation (5.5) has been fitted to the experimental data as shown in Figure 5.8 (a). There is a good fit when P_0=10. It should be noted that the influence of the GNP is not taken into consideration in this equation.

The relationship between barrier properties and orientation factor of the nanoplatelets is plotted in Figure 5.8 (b). Interestingly, a linear but rather weak correlation between permeability and filler orientation was found for all composites featuring similar levels of crystallinity. The 10:90 multilayer films containing the lowest amount of GNPs (0.5 wt%) but the highest (planar) filler orientation exhibited the lowest permeability, which can only be explained by improved alignment of the GNPs. However, when compared to the high permeability of the neat PLA films, all nanocomposites showed rather similar levels of permeability irrespective of filler orientation. This suggests that the large increase in polymer crystallinity as observed for all nanocomposite films is the primary reason for the improved

water vapour barrier properties of the films while the filler orientation factor plays only a secondary role.

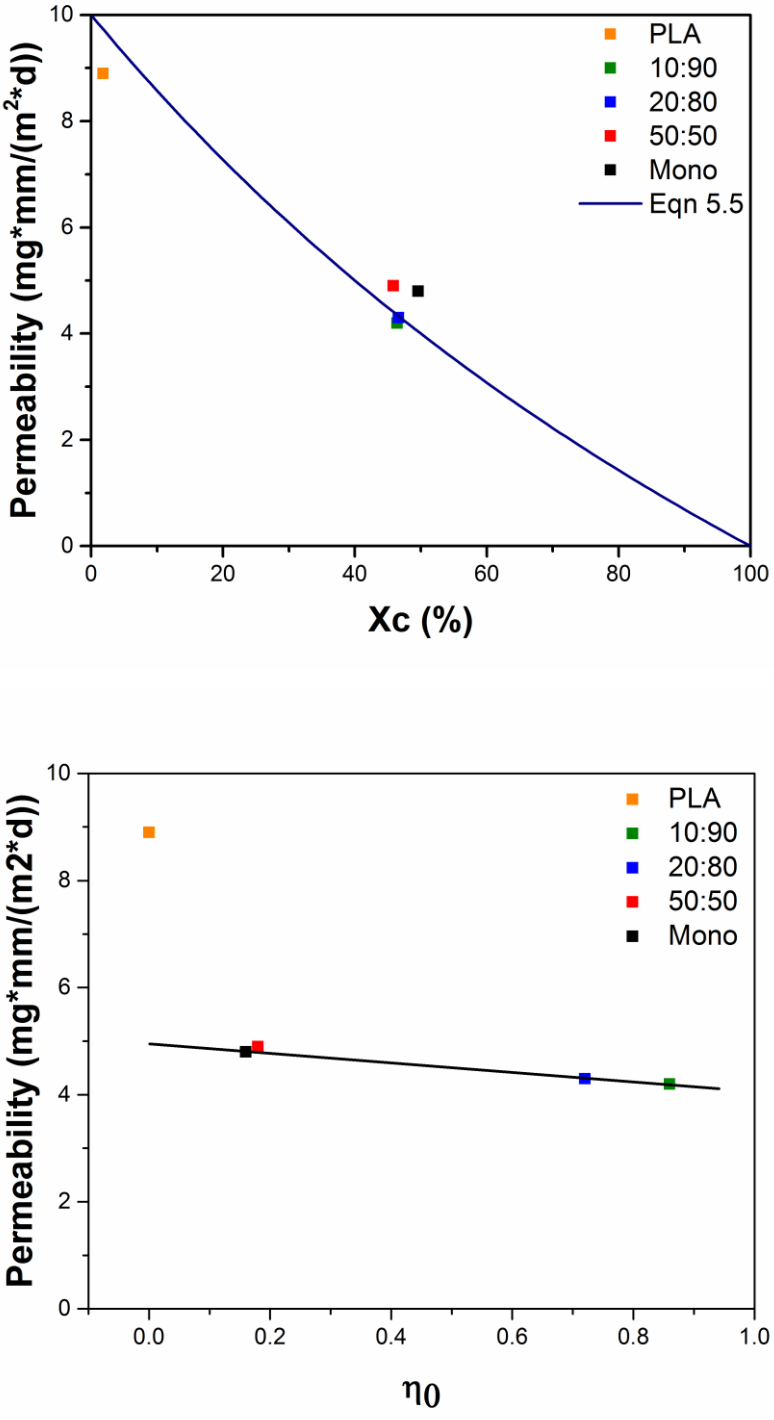

Figure 5.8. Water vapour permeability as a function of (a) polymer crystallinity and (b) filler orientation factor.

5.4 Conclusions

Multilayer co-extrusion was used to organise and align graphite nanoplatelets (GNP) in a PLA matrix. Multilayer structures made of alternating layers of neat PLA and PLA containing GNPs was evidenced by optical microscopy and SEM. Multilayer composite films were produced using the forced assembly co-extrusion technology with different ratios of filled and unfilled layer thicknesses. SEM images revealed further information regarding nanofiller size and alignment in the multilayer films. XRD studies confirmed a reduction in thickness of the GNPs with reduced filled layer thickness, indicating improved dispersion and possible exfoliation for these systems as a result of the multi-layering. Mechanical testing revealed similar Young's moduli for multilayer films as for mono-extruded films but at only 1/10 of the GNP loading, demonstrating increased GNP reinforcing efficiency in multilayer composites as a result of improved filler dispersion, aspect ratio and alignment. A significant mechanical reinforcement (Ec/Em) of 120% in individual filled layers of these multilayer films was achieved, confirming the potential of multilayer extrusion to align nanoplatelets through confinement. DMA confirmed that the glass transition temperature was not affected by the multi-layering or by the addition of GNP, while DSC confirmed that crystallinity (X_c) greatly increased for all nanocomposite films. Because crystallinity was similar for all composite films, these findings supported the hypothesis that improvements in reinforcing efficiency originated from improved GNP alignment in multilayer films, rather than from changes in crystallinity. The effect of improved filler efficiency in multi-layered PLA/GNP composites was further investigated by water vapour permeability tests. Results showed that multilayer films with the lowest filled layer thickness exhibited the best barrier properties as a result of a high polymer crystallinity together with a high filler orientation factor due to confinement. These PLA/GNP multilayer films offered similar barrier properties as PLA/nanoclay monolayer films but at only 1/10 of the filler loading. Force assembled multilayer films can be made using industrially-scalable extrusion technology, opening up the possibilities for lightweight and strong packaging materials for food and industrial applications

Chapter 6 - Summary and future work

6.1 Summary

In this thesis, we first reviewed recent advances in polymer/graphene composites, with a specific focus on its mechanical and electrical properties and related theory. The manufacturing and properties of multilayer composites were also reviewed;

A comparison between large (GNP-L) and small (GNP-S) graphene nanoplatelets was investigated in Chapter 3. An optimum loading for effective reinforcement was identified at about 5 wt% GNP for both grades. The reported maximum reinforcement (Ec/Em) of 24% for PLA composites incorporating 5 wt% GNP-L is among the highest reported for isotropic PLA/GNP nanocomposites.

Percolation thresholds for electrical conduction were studied in Chapter 4 and were the lowest for the high aspect ratio GNP-L nanofillers (~7 wt% for GNP-L and ~13 wt% for GNP-S, respectively). However, upon annealing the PLA/GNP-S systems showed improved electrical conductivity and a greatly reduced percolation threshold from 13 to around 6 wt%. PLA/GNP-L systems on the other hand did not show such a change in electrical properties after annealing. The mechanisms that accounted for the differences in electrical performance were further investigated using real-time dynamic percolation studies. It was shown that smaller GNP nanoparticles exhibited a much greater ability to form a conductive filler network by dynamic percolation during thermal annealing than larger nanoparticles. Hybrid nanocomposites incorporating both GNP-S and GNP-L nanofillers showed overall the best electrical properties, due to dynamic network formation of the small GNP-s in a static framework of large GNP-L during thermal annealing.

Highly structured PLA/GNP composites with controlled orientation and organisation of GNPs were evaluated in Chapter 5. Multilayer structures made of alternating layers of neat PLA and PLA containing GNPs was evidenced by optical microscopy and SEM. A significant mechanical reinforcement (Ec/Em) of 120% in individual filled layers of these multilayer films was achieved, confirming the potential of multilayer extrusion to align nanoplatelets through layer confinement. Because crystallinity was similar for all composite films, these findings supported the hypothesis that improvements in reinforcing efficiency originated from improved GNP alignment in these multilayer films, rather than from changes in crystallinity. These PLA/GNP multilayer films offered similar barrier properties as PLA/nanoclay monolayer films but at only 1/10 of the filler loading. These hierarchically engineered nanocomposite systems were produced using industrially-scalable forced assembly multilayer coextrusion technology, opening up the possibilities for lightweight and strong packaging materials for food and industrial applications.

6.2 Future work

In Chapter 6, only GNP-L was used for the production of multilayer films. However, it was already shown in Chapter 3 that smaller GNP-S can improve the toughness of PLA nanocomposites. Hence, it would be interesting to see the effect of GNP-S on the mechanical properties of multilayer films and check if similar improvements in toughness can be obtained. In fact, potentially even greater improvements could be envisaged due to improved nanofiller alignment. Moreover, hybrid filler systems could also be used, either with mixtures of GNP-S and GNP-L within a single layer or with PLA/GNP-S in layer A and PLA/GNP-L in layer B and improved electrical properties are to be expected, especially after thermal annealing. In fact, it would also be interesting to combine GNPs with other fillers such as CNTs, nanoclays, BN, MoS_2 though multilayer extrusion. Apart from adding secondary fillers, multilayer coextrusion could also be conducted with novel structures such as foams [337] or novel processing such as fibre extrusion [338]. Post processing such as biaxial stretching and annealing of multilayer films may also help with regards to further alignment of the fillers and improved mechanical, electrical and barrier properties.

In terms of conductivity, considering that PLA/GNP-S becomes highly conductive after thermal annealing, it would be interesting to see the effect of annealing on the electrical behaviour of multilayer PLA/GNP-S or PLA/GNP-L/GNP-S composites.

Although a certain degree of exfoliation is achieved as evidenced through a decrease in GNP thickness (Chapter 5), exfoliating multilayer graphene fully into mono- or few-layer graphene sheets with desired lateral dimensions seems still challenging. This might be realised by increasing the number of multiplier dies during the coextrusion process. Apart from that, further work still need to be done to improve the interfacial interactions between the carbon nanofillers and the PLA matrix to obtain the optimized mechanical reinforcement, possibly through coating and/or chemical modification of GNPs.

Despite these challenges, the multi-functionality of graphene based polymeric materials has attracted already industry and commercial graphene products such as tennis racquets are already available [339]. Taking this into account, the commercial impact of graphene nanocomposites is quite likely to increase in the future and graphene is likely to transform from a material ideal for fundamental studies by scientists leading to new physics, to an engineering material offering important solutions for industrial and consumer needs.

References

[1] B. Ji, H. Gao, Mechanical properties of nanostructure of biological materials, Journal of the Mechanics and Physics of Solids. 52 (9) 1963–1990. doi:10.1016/j.jmps.2004.03.006.

[2] P. Ciselli, Z. Wang, T. Peijs, Reinforcing potential of carbon nanotubes in oriented polymer fibres, Materials Technology. 22 (2007) 10–21.

[3] A.K. Geim, K.S. Novoselov, The rise of graphene., Nat. Mater. 6 (2007) 183–191. doi:10.1038/nmat1849.

[4] R.J. Young, I.A. Kinloch, L. Gong, K.S. Novoselov, The mechanics of graphene nanocomposites: A review, Composites Science and Technology. 72 (2012) 1459–1476. doi:10.1016/j.compscitech.2012.05.005.

[5] K. Kalaitzidou, H. Fukushima, L.T. Drzal, A new compounding method for exfoliated graphite–polypropylene nanocomposites with enhanced flexural properties and lower percolation threshold, Composites Science and Technology. 67 (2007) 2045–2051. doi:10.1016/j.compscitech.2006.11.014.

[6] C.D. Scott, S. Arepalli, P. Nikolaev, R.E. Smalley, Growth mechanisms for single-wall carbon nanotubes in a laser-ablation process:, Applied Physics A Materials Science & Processing. 72 (2001) 573–580. doi:10.1007/s003390100761.

[7] T. Nozaki, K. Okazaki, Carbon Nanotube Synthesis in Atmospheric Pressure Glow Discharge: A Review, Plasma Processes and Polymers. 5 (2008) 300–321. doi:10.1002/ppap.200700141.

[8] C.H. See, A.T. Harris, A Review of Carbon Nanotube Synthesis via Fluidized-Bed Chemical Vapor Deposition, Industrial & Engineering Chemistry Research. 46 (2007) 997–1012. doi:10.1021/ie060955b.

[9] L.M. Viculis, J.J. Mack, O.M. Mayer, H.T. Hahn, R.B. Kaner, Intercalation and exfoliation routes to graphite nanoplatelets., J. Mater. Chem. 15 (2005) 974–978. doi:10.1039/b413029d.

[10] D. Cho, S. Lee, G. Yang, H. Fukushima, L.T. Drzal, Dynamic Mechanical and Thermal Properties of Phenylethynyl-Terminated Polyimide Composites Reinforced With Expanded Graphite Nanoplatelets, Macromolecular Materials and Engineering. 290 (2005) 179–187. doi:10.1002/mame.200400281.

[11] Y. Zhan, Y. Lei, F. Meng, J. Zhong, R. Zhao, X. Liu, Electrical, thermal, and mechanical properties of polyarylene ether nitriles/graphite nanosheets nanocomposites prepared by masterbatch route, Journal of Materials Science. 46 (2011) 824–831. doi:10.1007/s10853-010-4823-7.

[12] X. Wu, S. Qi, J. He, G. Duan, High conductivity and low percolation threshold in polyaniline/graphite nanosheets composites, Journal of Materials Science. 45 (2010) 483–489. doi:10.1007/s10853-009-3965-y.

[13] J. Jacob George, A. Bandyopadhyay, A.K. Bhowmick, New generation layered nanocomposites derived from ethylene-co-vinyl acetate and naturally occurring graphite, Journal of Applied Polymer Science. 108 (2008) 1603–1616. doi:10.1002/app.25067.

[14] W. Lu, D. Wu, C. Wu, G. Chen, Nonlinear DC response in high-density polyethylene/graphite nanosheets composites, Journal of Materials Science. 41 (2006) 1785–1790. doi:10.1007/s10853-006-3946-3.

[15] B.Z. Jang, A. Zhamu, Processing of nanographene platelets (NGPs) and NGP nanocomposites: a review, Journal of Materials Science. 43 (2008) 5092–5101. doi:10.1007/s10853-008-2755-2.

[16] S. Park, R.S. Ruoff, Chemical methods for the production of graphenes., Nat. Nanotechnol. 4 (2009) 217–224. doi:10.1038/nnano.2009.58.

[17] H. Kim, A.A. Abdala, C.W. Macosko, Graphene/Polymer Nanocomposites, Macromolecules. 43 (2010) 6515–6530. doi:10.1021/ma100572e.

[18] S. Stankovich, D.A. Dikin, R.D. Piner, K.A. Kohlhaas, A. Kleinhammes, Y. Jia, Y. Wu, S.T. Nguyen, R.S. Ruoff, Synthesis of graphene-based nanosheets via chemical reduction of exfoliated graphite oxide, Carbon. 45 (2007) 1558–1565. doi:10.1016/j.carbon.2007.02.034.

[19] S. Gilje, S. Han, M. Wang, K.L. Wang, R.B. Kaner, A Chemical Route to Graphene for Device Applications, Nano Letters. 7 (2007) 3394–3398. doi:10.1021/nl0717715.

[20] M.J. McAllister, J.-L. Li, D.H. Adamson, H.C. Schniepp, A.A. Abdala, J. Liu, M. Herrera-Alonso, D.L. Milius, R. Car, R.K. Prud'homme, I.A. Aksay, Single Sheet Functionalized Graphene by Oxidation and Thermal Expansion of Graphite., Chem. Mater. 19 (2007) 4396–4404. doi:10.1021/cm0630800.

[21] M. Lotya, Y. Hernandez, P.J. King, R.J. Smith, V. Nicolosi, L.S. Karlsson, F.M. Blighe, S. De, Z. Wang, I.T. McGovern, G.S. Duesberg, J.N. Coleman, Liquid Phase Production of Graphene by Exfoliation of Graphite in Surfactant/Water Solutions, Journal of the American Chemical Society. 131 (2009) 3611–3620. doi:10.1021/ja807449u.

[22] S. Bhaviripudi, X. Jia, M.S. Dresselhaus, J. Kong, Role of Kinetic Factors in Chemical Vapor Deposition Synthesis of Uniform Large Area Graphene Using Copper Catalyst, Nano Letters. 10 (2010) 4128–4133. doi:10.1021/nl102355e.

[23] S. Stankovich, D.A. Dikin, G.H.B. Dommett, K.M. Kohlhaas, E.J. Zimney, E.A. Stach, R.D. Piner, S.T. Nguyen, R.S. Ruoff, Graphene-based composite materials., Nature (London, U. K.). 442 (2006) 282–286. doi:10.1038/nature04969.

[24] T. Kuilla, S. Bhadra, D. Yao, N.H. Kim, S. Bose, J.H. Lee, Recent advances in graphene based polymer composites, Progress in Polymer Science (Oxford). 35 (2010) 1350–1375. doi:10.1016/j.progpolymsci.2010.07.005.

[25] T.B. Rouf, J.L. Kokini, Biodegradable biopolymer–graphene nanocomposites, J Mater Sci. 51 (2016) 9915–9945. doi:10.1007/s10853-016-0238-4.

[26] B. Li, W.-H. Zhong, Review on polymer/graphite nanoplatelet nanocomposites, J Mater Sci. 46 (2011) 5595–5614. doi:10.1007/s10853-011-5572-y.

[27] C. Lee, X. Wei, J.W. Kysar, J. Hone, Measurement of the Elastic Properties and Intrinsic Strength of Monolayer Graphene., Science (Washington, DC, U. S.). 321 (2008) 385–388. doi:10.1126/science.1157996.

[28] F. Liu, P. Ming, J. Li, Ab initio calculation of ideal strength and phonon instability of graphene under tension, Physical Review B - Condensed Matter and Materials Physics. 76 (2007). doi:10.1103/PhysRevB.76.064120.

[29] O.L. Blakslee, D.G. Proctor, E.J. Seldin, G.B. Spence, T. Weng, Elastic constants of compression-annealed pyrolytic graphite, Journal of Applied Physics. 41 (1970) 3373–3382. doi:10.1063/1.1659428.

[30] R. Verdejo, M.M. Bernal, L.J. Romasanta, M.A. Lopez-Manchado, Graphene filled polymer nanocomposites, Journal of Materials Chemistry. 21 (2011) 3301–3310. doi:10.1039/c0jm02708a.

[31] M.C. Andrews, R.J. Young, Analysis of the deformation of aramid fibres and composites using Raman spectroscopy, Journal of Raman Spectroscopy. 24 (1993).

[32] P. Kannan, S.J. Eichhorn, R.J. Young, Deformation of isolated single-wall carbon nanotubes in electrospun polymer nanofibres, Nanotechnology. 18 (2007). doi:10.1088/0957-4484/18/23/235707.

[33] C.A. Cooper, R.J. Young, M. Halsall, Investigation into the deformation of carbon nanotubes and their composites through the use of Raman spectroscopy, Composites Part A: Applied Science and Manufacturing. 32 (2001) 401–411. doi:10.1016/S1359-835X(00)00107-X.

[34] O. Frank, G. Tsoukleri, I. Riaz, K. Papagelis, J. Parthenios, A.C. Ferrari, A.K. Geim, K.S. Novoselov, C. Galiotis, Development of a universal stress sensor for graphene and carbon fibres, Nature Communications. 2 (2011). doi:10.1038/ncomms1247.

[35] Z.H. Ni, T. Yu, Y.H. Lu, Y.Y. Wang, Y.P. Feng, Z.X. Shen, Uniaxial strain on graphene: Raman spectroscopy study and band-gap opening, ACS Nano. 2 (2008) 2301–2305. doi:10.1021/nn800459e.

[36] T. Yu, Z. Ni, C. Du, Y. You, Y. Wang, Z. Shen, Raman mapping investigation of graphene on transparent flexible substrate: The strain effect, Journal of Physical Chemistry C. 112 (2008) 12602–12605. doi:10.1021/jp806045u.

[37] M. Huang, H. Yan, C. Chen, D. Song, T.F. Heinz, J. Hone, Phonon softening and crystallographic orientation of strained graphene studied by Raman spectroscopy, Proceedings of the National Academy of Sciences of the United States of America. 106 (2009) 7304–7308. doi:10.1073/pnas.0811754106.

[38] T.M.G. Mohiuddin, A. Lombardo, R.R. Nair, A. Bonetti, G. Savini, R. Jalil, N. Bonini, D.M. Basko, C. Galiotis, N. Marzari, K.S. Novoselov, A.K. Geim, A.C. Ferrari, Uniaxial strain in graphene by Raman spectroscopy: G peak splitting, Grüneisen parameters, and sample orientation, Physical Review B - Condensed Matter and Materials Physics. 79 (2009). doi:10.1103/PhysRevB.79.205433.

[39] G. Tsoukleri, J. Parthenios, K. Papagelis, R. Jalil, A.C. Ferrari, A.K. Geim, K.S. Novoselov, C. Galiotis, Subjecting a graphene monolayer to tension and compression, Small. 5 (2009) 2397–2402. doi:10.1002/smll.200900802.

[40] J.E. Proctor, E. Gregoryanz, K.S. Novoselov, M. Lotya, J.N. Coleman, M.P. Halsall, High-pressure Raman spectroscopy of graphene, Physical Review B - Condensed Matter and Materials Physics. 80 (2009). doi:10.1103/PhysRevB.80.073408.

[41] C. Metzger, S. Rémi, M. Liu, S.V. Kusminskiy, A.H. Castro Neto, A.K. Swan, B.B. Goldberg, Biaxial strain in graphene adhered to shallow depressions, Nano Letters. 10 (2010) 6–10. doi:10.1021/nl901625v.

[42] L. Gong, I.A. Kinloch, R.J. Young, I. Riaz, R. Jalil, K.S. Novoselov, Interfacial stress transfer in a graphene monolayer nanocomposite, Advanced Materials. 22 (2010) 2694–2697. doi:10.1002/adma.200904264.

[43] M. Huang, H. Yan, T.F. Heinz, J. Hone, Probing strain-induced electronic structure change in graphene by Raman spectroscopy, Nano Letters. 10 (2010) 4074–4079. doi:10.1021/nl102123c.

[44] M. Mohr, J. Maultzsch, C. Thomsen, Splitting of the Raman 2D band of graphene subjected to strain, Physical Review B - Condensed Matter and Materials Physics. 82 (2010). doi:10.1103/PhysRevB.82.201409.

[45] F. Ding, H. Ji, Y. Chen, A. Herklotz, K. Dörr, Y. Mei, A. Rastelli, O.G. Schmidt, Stretchable graphene: A close look at fundamental parameters through biaxial straining, Nano Letters. 10 (2010) 3453–3458. doi:10.1021/nl101533x.

[46] O. Frank, M. Mohr, J. Maultzsch, C. Thomsen, I. Riaz, R. Jalil, K.S. Novoselov, G. Tsoukleri, J. Parthenios, K. Papagelis, L. Kavan, C. Galiotis, Raman 2D-band splitting in graphene: Theory and experiment, ACS Nano. 5 (2011) 2231–2239. doi:10.1021/nn103493g.

[47] Y.C. Cheng, Z.Y. Zhu, G.S. Huang, U. Schwingenschlögl, Grüneisen parameter of the G mode of strained monolayer graphene, Physical Review B - Condensed Matter and Materials Physics. 83 (2011). doi:10.1103/PhysRevB.83.115449.

[48] P. Zhang, L. Ma, F. Fan, Z. Zeng, C. Peng, P.E. Loya, Z. Liu, Y. Gong, J. Zhang, X. Zhang, P.M. Ajayan, T. Zhu, J. Lou, Fracture toughness of graphene, Nature Communications. 5 (2014) ncomms4782. doi:10.1038/ncomms4782.

[49] P.N. Nirmalraj, T. Lutz, S. Kumar, G.S. Duesberg, J.J. Boland, Nanoscale mapping of electrical resistivity and connectivity in graphene strips and networks, Nano Letters. 11 (2011) 16–22. doi:10.1021/nl101469d.

[50] R.L. Powell, G.E. Childs, American Institute of Physics Handbook. (1972) 140–160.

[51] S. Pei, J. Zhao, J. Du, W. Ren, H.-M. Cheng, Direct reduction of graphene oxide films into highly conductive and flexible graphene films by hydrohalic acids, Carbon. 48 (2010) 4466–4474. doi:10.1016/j.carbon.2010.08.006.

[52] H. Chen, M.B. Müller, K.J. Gilmore, G.G. Wallace, D. Li, Mechanically strong, electrically conductive, and biocompatible graphene paper, Advanced Materials. 20 (2008) 3557–3561. doi:10.1002/adma.200800757.

[53] X. Zhao, C.M. Hayner, M.C. Kung, H.H. Kung, Flexible holey graphene paper electrodes with enhanced rate capability for energy storage applications, ACS Nano. 5 (2011) 8739–8749. doi:10.1021/nn202710s.

[54] X. Lin, X. Shen, Q. Zheng, N. Yousefi, L. Ye, Y.-W. Mai, J.-K. Kim, Fabrication of highly-aligned, conductive, and strong graphene papers using ultralarge graphene oxide sheets, ACS Nano. 6 (2012) 10708–10719. doi:10.1021/nn303904z.

[55] K.S. Novoselov, Electric Field Effect in Atomically Thin Carbon Films, Science. 306 (2004) 666–669. doi:10.1126/science.1102896.

[56] H.C. Schniepp, K.N. Kudin, J.-L. Li, R.K. Prud'homme, R. Car, D.A. Saville, I.A. Aksay, Bending Properties of Single Functionalized Graphene Sheets Probed by Atomic Force Microscopy., ACS Nano. 2 (2008) 2577–2584. doi:10.1021/nn800457s.

[57] K.A. Mkhoyan, A.W. Contryman, J. Silcox, D.A. Stewart, G. Eda, C. Mattevi, S. Miller, M. Chhowalla, Atomic and Electronic Structure of Graphene-Oxide., Nano Lett. 9 (2009) 1058–1063. doi:10.1021/nl8034256.

[58] H.C. Schniepp, J.-L. Li, M.J. McAllister, H. Sai, M. Herrera-Alonso, D.H. Adamson, R.K. Prud'homme, R. Car, D.A. Saville, I.A. Aksay, Functionalized Single Graphene Sheets Derived from Splitting Graphite Oxide., J. Phys. Chem. B. 110 (2006) 8535–8539. doi:10.1021/jp060936f.

[59] C.N.R. Rao, K. Biswas, K.S. Subrahmanyam, A. Govindaraj, Graphene, the new nanocarbon, Journal of Materials Chemistry. 19 (2009) 2457–2469. doi:10.1039/b815239j.

[60] H. Kim, S.-W. Kim, Y.-U. Park, H. Gwon, D.-H. Seo, Y. Kim, K. Kang, SnO2/graphene composite with high lithium storage capability for lithium rechargeable batteries, Nano Res. 3 (2010) 813–821. doi:10.1007/s12274-010-0050-4.

[61] H.-B. Zhang, W.-G. Zheng, Q. Yan, Y. Yang, J.-W. Wang, Z.-H. Lu, G.-Y. Ji, Z.-Z. Yu, Electrically conductive polyethylene terephthalate/graphene nanocomposites prepared by melt compounding, Polymer. 51 (2010) 1191–1196. doi:10.1016/j.polymer.2010.01.027.

[62] G. Heo, Y.S. Kim, S.-H. Chun, M.-J. Seong, Polarized Raman spectroscopy with differing angles of laser incidence on single-layer graphene, Nanoscale Research Letters. 10 (2015) 45. doi:10.1186/s11671-015-0743-4.

[63] Y. Liu, Z. Liu, W.S. Lew, Q.J. Wang, Temperature dependence of the electrical transport properties in few-layer graphene interconnects, Nanoscale Research Letters. 8 (2013) 335.

[64] H.L. Cox, The elasticity and strength of paper and other fibrous materials, British Journal of Applied Physics. 3 (1952) 72–79. doi:10.1088/0508-3443/3/3/302.

[65] S.P. Kotha, S. Kotha, N. Guzelsu, Shear-lag model to account for interaction effects between inclusions in composites reinforced with rectangular platelets, Composites Science and Technology. 60 (2000) 2147–2158. doi:10.1016/S0266-3538(00)00114-7.

[66] B. Chen, P.D. Wu, H. Gao, A characteristic length for stress transfer in the nanostructure of biological composites, Composites Science and Technology. 69 (2009) 1160–1164. doi:10.1016/j.compscitech.2009.02.012.

[67] J. Tsai, C.T. Sun, Effect of Platelet Dispersion on the Load Transfer Efficiency in Nanoclay Composites, Journal of Composite Materials. 38 (2004) 567–579. doi:10.1177/0021998304042397.

[68] R.J. Young, P.A. Lovell, Introduction to Polymers. (1991).

[69] L. Gong, R.J. Young, I.A. Kinloch, I. Riaz, R. Jalil, K.S. Novoselov, Optimizing the reinforcement of polymer-based nanocomposites by graphene, ACS Nano. 6 (2012) 2086–2095. doi:10.1021/nn203917d.

[70] J.C.H. Affdl, J.L. Kardos, The Halpin-Tsai equations: A review, Polymer Engineering & Science. 16 (1976) 344–352. doi:10.1002/pen.760160512.

[71] T. Mori, K. Tanaka, Average stress in matrix and average elastic energy of materials with misfitting inclusions, Acta Metallurgica. 21 (1973) 571–574. doi:10.1016/0001-6160(73)90064-3.

[72] G.P. Tandon, G.J. Weng, The effect of aspect ratio of inclusions on the elastic properties of unidirectionally aligned composites, Polymer Composites. 5 (1984) 327–333. doi:10.1002/pc.750050413.

[73] J. Halpin, R. Thomas, Ribbon Reinforcement of Composites, Journal of Composite Materials. 2 (1968).

[74] I.H. Kim, Y.G. Jeong, Polylactide/exfoliated graphite nanocomposites with enhanced thermal stability, mechanical modulus, and electrical conductivity, Journal of Polymer Science, Part B: Polymer Physics. 48 (2010) 850–858. doi:10.1002/polb.21956.

[75] W. Zheng, S.-C. Wong, Electrical conductivity and dielectric properties of PMMA/expanded graphite composites, Composites Science and Technology. 63 (2003) 225–235. doi:10.1016/S0266-3538(02)00201-4.

[76] T. Ramanathan, S. Stankovich, D.A. Dikin, H. Liu, H. Shen, S.T. Nguyen, L.C. Brinson, Graphitic nanofillers in PMMA nanocomposites - An investigation of particle size and dispersion and their influence on nanocomposite properties, Journal of Polymer Science, Part B: Polymer Physics. 45 (2007) 2097–2112. doi:10.1002/polb.21187.

[77] K. Kalaitzidou, H. Fukushima, L.T. Drzal, Mechanical properties and morphological characterization of exfoliated graphite-polypropylene nanocomposites, Composites Part A: Applied Science and Manufacturing. 38 (2007) 1675–1682. doi:10.1016/j.compositesa.2007.02.003.

[78] K. Wakabayashi, C. Pierre, D.A. Dikin, R.S. Ruoff, T. Ramanathan, L.C. Brinson, J.M. Torkelson, Polymer-graphite nanocomposites: effective dispersion and major

property enhancement via solid-state shear pulverization., Macromolecules (Washington, DC, U. S.). 41 (2008) 1905–1908. doi:10.1021/ma071687b.

[79] S. Kim, I. Do, L.T. Drzal, Multifunctional xGnP/LLDPE Nanocomposites Prepared by Solution Compounding Using Various Screw Rotating Systems, Macromolecular Materials and Engineering. 294 (2009) 196–205. doi:10.1002/mame.200800319.

[80] W. Zheng, X. Lu, S.-C. Wong, Electrical and mechanical properties of expanded graphite-reinforced high-density polyethylene, Journal of Applied Polymer Science. 91 (2004) 2781–2788. doi:10.1002/app.13460.

[81] Y.F. Zhao, M. Xiao, S.J. Wang, X.C. Ge, Y.Z. Meng, Preparation and properties of electrically conductive PPS/expanded graphite nanocomposites, Composites Science and Technology. 67 (2007) 2528–2534. doi:10.1016/j.compscitech.2006.12.009.

[82] J. Liang, Y. Huang, L. Zhang, Y. Wang, Y. Ma, T. Guo, Y. Chen, Molecular-level dispersion of graphene into poly(vinyl alcohol) and effective reinforcement of their nanocomposites., Adv. Funct. Mater. 19 (2009) 2297–2302. doi:10.1002/adfm.200801776.

[83] X. Zhao, Q. Zhang, D. Chen, P. Lu, Enhanced mechanical properties of graphene-based polyvinyl alcohol composites, Macromolecules. 43 (2010) 2357–2363. doi:10.1021/ma902862u.

[84] Y.R. Lee, A.V. Raghu, H.M. Jeong, B.K. Kim, Properties of Waterborne Polyurethane/Functionalized Graphene Sheet Nanocomposites Prepared by an in situ Method., Macromol. Chem. Phys. 210 (2009) 1247–1254. doi:10.1002/macp.200900157.

[85] X.S. Du, M. Xiao, Y.Z. Meng, Synthesis and characterization of polyaniline/graphite conducting nanocomposites, Journal of Polymer Science, Part B: Polymer Physics. 42 (2004) 1972–1978. doi:10.1002/polb.20102.

[86] J. Yang, M. Tian, Q.-X. Jia, J.-H. Shi, L.-Q. Zhang, S.-H. Lim, Z.-Z. Yu, Y.-W. Mai, Improved mechanical and functional properties of elastomer/graphite nanocomposites prepared by latex compounding, Acta Materialia. 55 (2007) 6372–6382. doi:10.1016/j.actamat.2007.07.043.

[87] J. Lu, L.T. Drzal, R.M. Worden, I. Lee, Simple Fabrication of a Highly Sensitive Glucose Biosensor Using Enzymes Immobilized in Exfoliated Graphite Nanoplatelets Nafion Membrane, Chemistry of Materials. 19 (2007) 6240–6246. doi:10.1021/cm702133u.

[88] S. Jana, W.-H. Zhong, Graphite particles with a “puffed” structure and enhancement in mechanical performance of their epoxy composites, Materials Science and Engineering: A. 525 (2009) 138–146. doi:10.1016/j.msea.2009.06.052.

[89] K. Kalaitzidou, H. Fukushima, H. Miyagawa, L.T. Drzal, Flexural and tensile moduli of polypropylene nanocomposites and comparison of experimental data to Halpin-Tsai and Tandon-Weng models, Polymer Engineering & Science. 47 (2007) 1796–1803. doi:10.1002/pen.20879.

[90] S. Kim, J. Seo, L.T. Drzal, Improvement of electric conductivity of LLDPE based nanocomposite by paraffin coating on exfoliated graphite nanoplatelets, Composites

Part A: Applied Science and Manufacturing. 41 (2010) 581–587. doi:10.1016/j.compositesa.2009.05.002.

[91] X. Jiang, L.T. Drzal, Multifunctional high density polyethylene nanocomposites produced by incorporation of exfoliated graphite nanoplatelets 1: Morphology and mechanical properties, Polym Compos. 31 (2010) 1091–1098. doi:10.1002/pc.20896.

[92] J. Li, L. Vaisman, G. Marom, J.-K. Kim, Br treated graphite nanoplatelets for improved electrical conductivity of polymer composites, Carbon. 45 (2007) 744–750. doi:10.1016/j.carbon.2006.11.031.

[93] D. Chen, J. Yang, G. Chen, The physical properties of polyurethane/graphite nanosheets/carbon black foaming conducting nanocomposites, Composites Part A: Applied Science and Manufacturing. 41 (2010) 1636–1638. doi:10.1016/j.compositesa.2010.07.013.

[94] Y.-C. Li, G.-H. Chen, HDPE/expanded graphite nanocomposites prepared via masterbatch process, Polymer Engineering & Science. 47 (2007) 882–888. doi:10.1002/pen.20772.

[95] C. Min, D. Yu, Simultaneously improved toughness and dielectric properties of epoxy/graphite nanosheet composites, Polymer Engineering & Science. 50 (2010) 1734–1742. doi:10.1002/pen.21698.

[96] L. Wang, J. Hong, G. Chen, Comparison study of graphite nanosheets and carbon black as fillers for high density polyethylene, Polymer Engineering & Science. 50 (2010) 2176–2181. doi:10.1002/pen.21751.

[97] H. Hu, G. Chen, Electrochemically modified graphite nanosheets and their nanocomposite films with poly(vinyl alcohol), Polymer Composites. 31 (2010) 1770–1775. doi:10.1002/pc.20968.

[98] K.P. Pramoda, H. Hussain, H.M. Koh, H.R. Tan, C.B. He, Covalent bonded polymer-graphene nanocomposites, Journal of Polymer Science Part A: Polymer Chemistry. 48 (2010) 4262–4267. doi:10.1002/pola.24212.

[99] S. Gupta, P. Raju Mantena, A. Al-Ostaz, Dynamic Mechanical and Impact Property Correlation of Nanoclay and Graphite Platelet Reinforced Vinyl Ester Nanocomposites, Journal of Reinforced Plastics and Composites. 29 (2010) 2037–2047. doi:10.1177/0731684409341762.

[100] C.-W. Wang, G.-Q. Xin, Y.-I. Lee, J. Hao, J. Jiang, H.-G. Liu, Poly(9-vinylcarbazole)/silver composite nanotubes and networks formed at the air–water interface, Journal of Applied Polymer Science. 116 (2010) 252–257. doi:10.1002/app.31443.

[101] S. Chatterjee, F.A. Nüesch, B.T.T. Chu, Comparing carbon nanotubes and graphene nanoplatelets as reinforcements in polyamide 12 composites, Nanotechnology. 22 (2011). doi:10.1088/0957-4484/22/27/275714.

[102] K. Wakabayashi, P.J. Brunner, J. Masuda, S.A. Hewlett, J.M. Torkelson, Polypropylene-graphite nanocomposites made by solid-state shear pulverization: Effects of significantly exfoliated, unmodified graphite content on physical, mechanical and

electrical properties, Polymer. 51 (2010) 5525–5531. doi:10.1016/j.polymer.2010.09.007.

[103] A.N. Wilkinson, I.A. Kinloch, R.N. Othman, Low viscosity processing using hybrid CNT-coated silica particles to form electrically conductive epoxy resin composites, Polymer. 98 (2016) 32–38.

[104] W.G. Weng, G.H. Chen, D.J. Wu, W.L. Yan, HDPE/expanded graphite electrically conducting composite, Composite Interfaces. 11 (2004) 131–143. doi:10.1163/156855404322971404.

[105] G.H. Chen, D.J. Wu, W.G. Weng, W.L. Yan, Preparation of polymer/graphite conducting nanocomposite by intercalation polymerization, Journal of Applied Polymer Science. 82 (2001) 2506–2513. doi:10.1002/app.2101.

[106] J. Li, M. Sham, J. Kim, G. Marom, Morphology and properties of UV/ozone treated graphite nanoplatelet/epoxy nanocomposites, Composites Science and Technology. 67 (2007) 296–305. doi:10.1016/j.compscitech.2006.08.009.

[107] J. Li, J.-K. Kim, M. Lung Sham, Conductive graphite nanoplatelet/epoxy nanocomposites: Effects of exfoliation and UV/ozone treatment of graphite, Scripta Materialia. 53 (2005) 235–240. doi:10.1016/j.scriptamat.2005.03.034.

[108] B.A. Alshammari, A. Wilkinson, Impact of carbon nanotubes addition on electrical, thermal, morphological, and tensile properties of poly (ethylene terephthalate), Applied Petrochemical Research. (2016) 1–11.

[109] B. Alshammari, A. Wilkinson, Comparison Study of Graphite, Graphite Nano-Platelets and Multiwall Carbon Nanotubes as Conductive Fillers of Polyethylene Terephthalate Matrix, in: Proceedings of the Eighth Saudi Students Conference in the UK, World Scientific, 2015: p. 453. http://books.google.com/books?hl=en&lr=&id=pH_FCwAAQBAJ&oi=fnd&pg=PA453&dq=info:TrE-NayhG-UJ:scholar.google.com&ots=_BU-P076Y-&sig=Z0owacbdbDzYOT_ThYcZlQ_tlSw.

[110] V.K.S. Shante, S. Kirkpatrick, An introduction to percolation theory, Adv. Phys. 20 (1971).

[111] H. Kim, C.W. Macosko, Processing-property relationships of polycarbonate/graphene composites., Polymer. 50 (2009) 3797–3809. doi:10.1016/j.polymer.2009.05.038.

[112] S. Kirkpatrick, Percolation and Conduction, Rev. Mod. Phys. 45 (1973) 574–588. doi:10.1103/RevModPhys.45.574.

[113] I. Balberg, Tunneling and nonuniversal conductivity in composite materials, Phys. Rev. Lett. 59 (1987) 1305–1308. doi:10.1103/PhysRevLett.59.1305.

[114] C.-W. Nan, Y. Shen, J. Ma, Physical properties of composites near percolation, 2010. doi:10.1146/annurev-matsci-070909-104529.

[115] R.N. Othman, I.A. Kinloch, A.N. Wilkinson, Synthesis and characterisation of silica–carbon nanotube hybrid microparticles and their effect on the electrical properties of poly (vinyl alcohol) composites, Carbon. 60 (2013) 461–470.

[116] J. Li, J.K. Kim, Percolation threshold of conducting polymer composites containing 3D randomly distributed graphite nanoplatelets, Composites Science and Technology. 67 (2007) 2114–2120. doi:10.1016/j.compscitech.2006.11.010.

[117] G.R. Ruschau, S. Yoshikawa, R.E. Newnham, Resistivities of conductive composites, Journal of Applied Physics. 72 (1992) 953–959. doi:10.1063/1.352350.

[118] A. Celzard, E. McRae, C. Deleuze, M. Dufort, G. Furdin, J.F. Mareche, Critical concentration in percolating systems containing a high-aspect-ratio filler., Phys. Rev. B: Condens. Matter. 53 (1996) 6209–14.

[119] C. Lu, Y.-W. Mai, Influence of aspect ratio on barrier properties of polymer-clay nanocomposites, Physical Review Letters. 95 (2005). doi:10.1103/PhysRevLett.95.088303.

[120] M.H. Al-Saleh, U. Sundararaj, A review of vapor grown carbon nanofiber/polymer conductive composites, Carbon. 47 (2009) 2–22. doi:10.1016/j.carbon.2008.09.039.

[121] Y. She, G. Chen, D. Wu, Fabrication of polyethylene/graphite nanocomposite from modified expanded graphite, Polymer International. 56 (2007) 679–685. doi:10.1002/pi.2191.

[122] Y.C. Li, S.C. Tjong, R.K.Y. Li, Electrical conductivity and dielectric response of poly(vinylidene fluoride)–graphite nanoplatelet composites, Synthetic Metals. 160 (2010) 1912–1919. doi:10.1016/j.synthmet.2010.07.009.

[123] C. Yu, B. Li, Preparation and characterization of carboxymethyl polyvinyl alcohol-graphite nanosheet composites, Polymer Composites. 29 (2008) 998–1005. doi:10.1002/pc.20478.

[124] W.-P. Wang, C.-Y. Pan, Preparation and characterization of poly(methyl methacrylate)-intercalated graphite oxide/poly(methyl methacrylate) nanocomposite., Polym. Eng. Sci. 44 (2004) 2335–2339. doi:10.1002/pen.20261.

[125] M. Green, G. Marom, J. Li, J. Kim, The Electrical Conductivity of Graphite Nanoplatelet Filled Conjugated Polyacrylonitrile, Macromolecular Rapid Communications. 29 (2008) 1254–1258. doi:10.1002/marc.200800146.

[126] H. Kim, C.W. Macosko, Morphology and properties of polyester/exfoliated graphite nanocomposites., Macromolecules (Washington, DC, U. S.). 41 (2008) 3317–3327. doi:10.1021/ma702385h.

[127] W. Weng, G. Chen, D. Wu, X. Chen, J. Lu, P. Wang, Fabrication and characterization of nylon 6/foliated graphite electrically conducting nanocomposite, Journal of Polymer Science, Part B: Polymer Physics. 42 (2004) 2844–2856. doi:10.1002/polb.20140.

[128] X.S. Du, M. Xiao, Y.Z. Meng, A.S. Hay, Synthesis and properties of poly(4,4'-oxybis(benzene)disulfide)/graphite nanocomposites via in situ ring-opening polymerization of macrocyclic oligomers, Polymer. 45 (2004) 6713–6718. doi:10.1016/j.polymer.2004.07.026.

[129] O.C. Compton, S. Kim, C. Pierre, J.M. Torkelson, S.T. Nguyen, Crumpled graphene nanosheets as highly effective barrier property enhancers, Advanced Materials. 22 (2010) 4759–4763. doi:10.1002/adma.201000960.

[130] B. Tan, N.L. Thomas, A review of the water barrier properties of polymer/clay and polymer/graphene nanocomposites, Journal of Membrane Science. 514 (2016) 595–612. doi:10.1016/j.memsci.2016.05.026.

[131] L.E. Nielsen, Models for the Permeability of Filled Polymer Systems, Journal of Macromolecular Science: Part A - Chemistry. 1 (1967) 929–942. doi:10.1080/10601326708053745.

[132] Z. Duan, N.L. Thomas, W. Huang, Water vapour permeability of poly(lactic acid) nanocomposites, Journal of Membrane Science. 445 (2013) 112–118. doi:10.1016/j.memsci.2013.06.008.

[133] J. Jin, R. Rafiq, Y.Q. Gill, M. Song, Preparation and characterization of high performance of graphene/nylon nanocomposites, European Polymer Journal. 49 (2013) 2617–2626. doi:10.1016/j.eurpolymj.2013.06.004.

[134] I.-H. Tseng, Y.-F. Liao, J.-C. Chiang, M.-H. Tsai, Transparent polyimide/graphene oxide nanocomposite with improved moisture barrier property, Materials Chemistry and Physics. 136 (2012) 247–253. doi:10.1016/j.matchemphys.2012.06.061.

[135] M.-H. Tsai, C.-J. Chang, H.-H. Lu, Y.-F. Liao, I.-H. Tseng, Properties of magnetron-sputtered moisture barrier layer on transparent polyimide/graphene nanocomposite film, Thin Solid Films. 544 (2013) 324–330. doi:10.1016/j.tsf.2013.02.105.

[136] I.-H. Tseng, M.-H. Tsai, C.-W. Chung, Flexible and transparent polyimide films containing two-dimensional alumina nanosheets templated by graphene oxide for improved barrier property, ACS Applied Materials and Interfaces. 6 (2014) 13098–13105. doi:10.1021/am502962b.

[137] C.-H. Chang, T.-C. Huang, C.-W. Peng, T.-C. Yeh, H.-I. Lu, W.-I. Hung, C.-J. Weng, T.-I. Yang, J.-M. Yeh, Novel anticorrosion coatings prepared from polyaniline/graphene composites, Carbon. 50 (2012) 5044–5051. doi:10.1016/j.carbon.2012.06.043.

[138] N. Yousefi, M.M. Gudarzi, Q. Zheng, X. Lin, X. Shen, J. Jia, F. Sharif, J.-K. Kim, Highly aligned, ultralarge-size reduced graphene oxide/polyurethane nanocomposites: Mechanical properties and moisture permeability, Composites Part A: Applied Science and Manufacturing. 49 (2013) 42–50. doi:10.1016/j.compositesa.2013.02.005.

[139] H. Kwon, D. Kim, J. Seo, H. Han, Enhanced moisture barrier films based on EVOH/exfoliated graphite (EGn) nanocomposite films by solution blending, Macromolecular Research. 21 (2013) 987–994. doi:10.1007/s13233-013-1124-4.

[140] H.-D. Huang, P.-G. Ren, J. Chen, W.-Q. Zhang, X. Ji, Z.-M. Li, High barrier graphene oxide nanosheet/poly(vinyl alcohol) nanocomposite films, Journal of Membrane Science. 409–410 (2012) 156–163. doi:10.1016/j.memsci.2012.03.051.

[141] V. Loryuenyong, C. Saewong, C. Aranchaiya, A. Buasri, The Improvement in Mechanical and Barrier Properties of Poly(Vinyl Alcohol)/Graphene Oxide Packaging Films, Packaging Technology and Science. 28 (2015) 939–947. doi:10.1002/pts.2149.

[142] R. Kabiri, H. Namazi, Nanocrystalline cellulose acetate (NCCA)/graphene oxide (GO) nanocomposites with enhanced mechanical properties and barrier against water vapor, (2014). doi:10.1007/s10570-014-0366-4.

[143] K. Yano, A. Usuki, A. Okada, Synthesis and properties of polyimide-clay hybrid films, Journal of Polymer Science, Part A: Polymer Chemistry. 35 (1997) 2289–2294.

[144] A.N. Wilkinson, M.L. Clemens, V.M. Harding, The effects of SEBS-g-maleic anhydride reaction on the morphology and properties of polypropylene/PA6/SEBS ternary blends, Polymer. 45 (2004) 5239–5249.

[145] A.N. Wilkinson, L. Laugel, M.L. Clemens, V.M. Harding, M. Marin, Phase structure in polypropylene/PA6/SEBS blends, Polymer. 40 (1999) 4971–4975.

[146] A. Yu, P. Ramesh, X. Sun, E. Bekyarova, M.E. Itkis, R.C. Haddon, Enhanced thermal conductivity in a hybrid graphite nanoplatelet - carbon nanotube filler for epoxy composites., Adv. Mater. (Weinheim, Ger.). 20 (2008) 4740–4744. doi:10.1002/adma.200800401.

[147] K.T.S. Kong, M. Mariatti, A.A. Rashid, J.J.C. Busfield, Enhanced conductivity behavior of polydimethylsiloxane (PDMS) hybrid composites containing exfoliated graphite nanoplatelets and carbon nanotubes, Composites Part B: Engineering. 58 (2014) 457–462. doi:10.1016/j.compositesb.2013.10.039.

[148] T. Wei, L. Song, C. Zheng, K. Wang, J. Yan, B. Shao, Z.-J. Fan, The synergy of a three filler combination in the conductivity of epoxy composites, Materials Letters. 64 (2010) 2376–2379. doi:10.1016/j.matlet.2010.07.061.

[149] K.E. Prasad, B. Das, U. Maitra, U. Ramamurty, C.N.R. Rao, Extraordinary synergy in the mechanical properties of polymer matrix composites reinforced with 2 nanocarbons., Proc. Natl. Acad. Sci. U. S. A. 106 (2009) 13186–13189, S13186/1–S13186/3. doi:10.1073/pnas.0905844106.

[150] J. Li, P.-S. Wong, J.-K. Kim, Hybrid nanocomposites containing carbon nanotubes and graphite nanoplatelets, Materials Science and Engineering: A. 483–484 (2008) 660–663. doi:10.1016/j.msea.2006.08.145.

[151] S. Kumar, L.L. Sun, S. Caceres, B. Li, W. Wood, A. Perugini, R.G. Maguire, W.H. Zhong, Dynamic synergy of graphitic nanoplatelets and multi-walled carbon nanotubes in polyetherimide nanocomposites, Nanotechnology. 21 (2010) 105702. doi:10.1088/0957-4484/21/10/105702.

[152] S. Zhang, L. Lin, H. Deng, X. Gao, E. Bilotti, T. Peijs, Q. Zhang, Q. Fu, Dynamic percolation in highly oriented conductive networks formed with different carbon nanofillers, Colloid and Polymer Science. 290 (2012) 1393–1401.

[153] E. Bilotti, H. Zhang, H. Deng, R. Zhang, Q. Fu, T. Peijs, Controlling the dynamic percolation of carbon nanotube based conductive polymer composites by addition of

secondary nanofillers: the effect on electrical conductivity and tuneable sensing behaviour, Composites Science and Technology. 74 (2013) 85–90.

[154] W. Zhang, R.S. Blackburn, A.A. Dehghani-Sanij, Effect of silica concentration on electrical conductivity of epoxy resin–carbon black–silica nanocomposites, Scripta Materialia. 56 (2007) 581–584. doi:10.1016/j.scriptamat.2006.12.039.

[155] S. Nam, H. Woo Cho, T. Kim, D. Kim, B. June Sung, S. Lim, H. Kim, Effects of silica particles on the electrical percolation threshold and thermomechanical properties of epoxy/silver nanocomposites, Applied Physics Letters. 99 (2011) 043104.

[156] H.-D. Bao, Z.-X. Guo, J. Yu, Effect of electrically inert particulate filler on electrical resistivity of polymer/multi-walled carbon nanotube composites, Polymer. 49 (2008) 3826–3831. doi:10.1016/j.polymer.2008.06.024.

[157] B.E. Kilbride, J.N. Coleman, J. Fraysse, P. Fournet, M. Cadek, A. Drury, S. Hutzler, S. Roth, W.J. Blau, Experimental observation of scaling laws for alternating current and direct current conductivity in polymer-carbon nanotube composite thin films, Journal of Applied Physics. 92 (2002) 4024–4030. doi:10.1063/1.1506397.

[158] J. Zhang, M. Mine, D. Zhu, M. Matsuo, Electrical and dielectric behaviors and their origins in the three-dimensional polyvinyl alcohol/MWCNT composites with low percolation threshold, Carbon. 47 (2009) 1311–1320. doi:10.1016/j.carbon.2009.01.014.

[159] M.S. Shaffer, A.H. Windle, Fabrication and characterization of carbon nanotube/poly (vinyl alcohol) composites, Advanced Materials. 11 (1999) 937–941.

[160] D.L. Kaplan, Introduction to biopolymers from renewable resources, Biopolymers from Renewable Resources. (1998) 1–29.

[161] R.S. Blackburn, Biodegradable and sustainable fibres, Taylor & Francis US, 2005.

[162] G. Schmack, B. Tändler, R. Vogel, R. Beyreuther, S. Jacobsen, H.-G. Fritz, Biodegradable fibers of poly(L-lactide) produced by high-speed melt spinning and spin drawing, J. Appl. Polym. Sci. 73 (1999) 2785–2797. doi:10.1002/(SICI)1097-4628(19990929)73:14<2785::AID-APP1>3.0.CO;2-L.

[163] O. Avinc, A. Khoddami, Overview of Poly(lactic acid) (PLA) Fibre, Fibre Chem. 41 (2009) 391–401. doi:10.1007/s10692-010-9213-z.

[164] H. Tsuji, Y. Ikada, Properties and morphologies of poly (L-lactide): 1. Annealing condition effects on properties and morphologies of poly (L-lactide), Polymer. 36 (1995) 2709–2716.

[165] S. Brochu, R.E. Prud'Homme, I. Barakat, R. Jerome, Stereocomplexation and morphology of polylactides, Macromolecules. 28 (1995) 5230–5239.

[166] K.A. Thakur, R.T. Kean, J.M. Zupfer, N.U. Buehler, M.A. Doscotch, E.J. Munson, Solid state 13C CP-MAS NMR studies of the crystallinity and morphology of poly (L-lactide), Macromolecules. 29 (1996) 8844–8851.

[167] P. De Santis, A.J. Kovacs, Molecular conformation of poly (S-lactic acid), Biopolymers. 6 (1968) 299–306.

[168] W. Hoogsteen, A.R. Postema, A.J. Pennings, G. Ten Brinke, P. Zugenmaier, Crystal structure, conformation and morphology of solution-spun poly (L-lactide) fibers, Macromolecules. 23 (1990) 634–642.

[169] J. Kobayashi, T. Asahi, M. Ichiki, A. Oikawa, H. Suzuki, T. Watanabe, E. Fukada, Y. Shikinami, Structural and optical properties of poly lactic acids, Journal of Applied Physics. 77 (1995) 2957–2973.

[170] B. Eling, S. Gogolewski, A.J. Pennings, Biodegradable materials of poly (l-lactic acid): 1. Melt-spun and solution-spun fibres, Polymer. 23 (1982) 1587–1593.

[171] J. Puiggali, Y. Ikada, H. Tsuji, L. Cartier, T. Okihara, B. Lotz, The frustrated structure of poly (l-lactide), Polymer. 41 (2000) 8921–8930.

[172] D. Sawai, K. Takahashi, A. Sasashige, T. Kanamoto, S.-H. Hyon, Preparation of oriented β-form poly (L-lactic acid) by solid-state coextrusion: effect of extrusion variables, Macromolecules. 36 (2003) 3601–3605.

[173] D. Brizzolara, H.-J. Cantow, K. Diederichs, E. Keller, A.J. Domb, Mechanism of the stereocomplex formation between enantiomeric poly (lactide) s, Macromolecules. 29 (1996) 191–197.

[174] L. Cartier, T. Okihara, Y. Ikada, H. Tsuji, J. Puiggali, B. Lotz, Epitaxial crystallization and crystalline polymorphism of polylactides, Polymer. 41 (2000) 8909–8919.

[175] P. Pan, W. Kai, B. Zhu, T. Dong, Y. Inoue, Polymorphous crystallization and multiple melting behavior of poly (L-lactide): molecular weight dependence, Macromolecules. 40 (2007) 6898–6905.

[176] J. Zhang, Y. Duan, H. Sato, H. Tsuji, I. Noda, S. Yan, Y. Ozaki, Crystal modifications and thermal behavior of poly (L-lactic acid) revealed by infrared spectroscopy, Macromolecules. 38 (2005) 8012–8021.

[177] T. Kawai, N. Rahman, G. Matsuba, K. Nishida, T. Kanaya, M. Nakano, H. Okamoto, J. Kawada, A. Usuki, N. Honma, others, Crystallization and melting behavior of poly (L-lactic acid), Macromolecules. 40 (2007) 9463–9469.

[178] J. Zhang, K. Tashiro, H. Tsuji, A.J. Domb, Disorder-to-order phase transition and multiple melting behavior of poly (L-lactide) investigated by simultaneous measurements of WAXD and DSC, Macromolecules. 41 (2008) 1352–1357.

[179] J. Zhang, K. Tashiro, A.J. Domb, H. Tsuji, Confirmation of Disorder α Form of Poly (L-lactic acid) by the X-ray Fiber Pattern and Polarized IR/Raman Spectra Measured for Uniaxially-Oriented Samples, in: Macromolecular Symposia, Wiley Online Library, 2006: pp. 274–278. http://onlinelibrary.wiley.com/doi/10.1002/masy.200651038/full.

[180] P. Pan, B. Zhu, W. Kai, T. Dong, Y. Inoue, Polymorphic Transition in Disordered Poly(l-lactide) Crystals Induced by Annealing at Elevated Temperatures, Macromolecules. 41 (2008) 4296–4304. doi:10.1021/ma800343g.

[181] G. Perego, G.D. Cella, C. Bastioli, Effect of molecular weight and crystallinity on poly (lactic acid) mechanical properties, Journal of Applied Polymer Science. 59 (1996) 37–43.

[182] D.M. Bigg, Polylactide copolymers: Effect of copolymer ratio and end capping on their properties, Adv. Polym. Technol. 24 (2005) 69–82. doi:10.1002/adv.20032.

[183] J.E. Mark, Polymer Data Handbook. (1999).

[184] Y. Cheng, S. Deng, P. Chen, R. Ruan, Polylactic acid (PLA) synthesis and modifications: A review, Frontiers of Chemistry in China. 4 (2009) 259–264. doi:10.1007/s11458-009-0092-x.

[185] D. Garlotta, A literature review of poly(lactic acid), Journal of Polymers and the Environment. 9 (2001) 63–84.

[186] W. Jia, H. Gong, A. Wilkinson, P. Hogg, A STUDY OF POLY (LACTIC ACID) SELF-REINFORCED BIODEGRADABLE COMPOSITES, in: Texcomp-11, Leuven, Belgium. 16-20 September 2013, 2013. https://www.escholar.manchester.ac.uk/uk-ac-man-scw:233446.

[187] J.M. Raquez, Y. Habibi, M. Murariu, P. Dubois, Polylactide (PLA)-based nanocomposites, Progress in Polymer Science. 38 (2013) 1504–1542. doi:10.1016/j.progpolymsci.2013.05.014.

[188] D. Galpaya, M. Wang, M. Liu, N. Motta, E. Waclawik, C. Yan, Recent advances in fabrication and characterization of graphene-polymer nanocomposites, Graphene. 1 (2012) 30–49.

[189] H. Norazlina, Y. Kamal, Graphene modifications in polylactic acid nanocomposites: a review, Polym. Bull. 72 (2015) 931–961. doi:10.1007/s00289-015-1308-5.

[190] S. Singh, S.S. Ray, Polylactide Based Nanostructured Biomaterials and Their Applications, Journal of Nanoscience and Nanotechnology. 7 (2007) 2596–2615. doi:10.1166/jnn.2007.909.

[191] M. Alexandre, P. Dubois, Polymer-layered silicate nanocomposites: Preparation, properties and uses of a new class of materials, Materials Science and Engineering R: Reports. 28 (2000) 1–63. doi:10.1016/S0927-796X(00)00012-7.

[192] P. Bordes, E. Pollet, L. Avérous, Nano-biocomposites: Biodegradable polyester/nanoclay systems, Progress in Polymer Science. 34 (2009) 125–155. doi:10.1016/j.progpolymsci.2008.10.002.

[193] S. Faghihi, M. Gheysour, A. Karimi, R. Salarian, Fabrication and mechanical characterization of graphene oxide-reinforced poly (acrylic acid)/gelatin composite hydrogels, Journal of Applied Physics. 115 (2014). doi:10.1063/1.4864153.

[194] W. Li, Z. Xu, L. Chen, M. Shan, X. Tian, C. Yang, H. Lv, X. Qian, A facile method to produce graphene oxide-g-poly(L-lactic acid) as an promising reinforcement for PLLA nanocomposites, Chemical Engineering Journal. 237 (2014) 291–299. doi:10.1016/j.cej.2013.10.034.

[195] Y. Cao, J. Feng, P. Wu, Preparation of organically dispersible graphene nanosheet powders through a lyophilization method and their poly(lactic acid) composites, Carbon. 48 (2010) 3834–3839. doi:10.1016/j.carbon.2010.06.048.

[196] M. Murariu, A.L. Dechief, L. Bonnaud, Y. Paint, A. Gallos, G. Fontaine, S. Bourbigot, P. Dubois, The production and properties of polylactide composites filled with expanded graphite, Polymer Degradation and Stability. 95 (2010) 889–900. doi:10.1016/j.polymdegradstab.2009.12.019.

[197] B.W. Chieng, N.A. Ibrahim, W.M.Z.W. Yunus, M.Z. Hussein, Y.Y. Then, Y.Y. Loo, Effects of graphene nanoplatelets and reduced graphene oxide on poly(lactic acid) and plasticized poly(lactic acid): A comparative study, Polymers. 6 (2014) 2232–2246. doi:10.3390/polym6082232.

[198] B.W. Chieng, N.A. Ibrahim, W.M.Z.W. Yunus, M.Z. Hussein, Poly(lactic acid)/poly(ethylene glycol) polymer nanocomposites: Effects of graphene nanoplatelets, Polymers. 6 (2014) 93–104. doi:10.3390/polym6010093.

[199] J.S.F. Barrett, A.A. Abdala, F. Srienc, Poly(hydroxyalkanoate) elastomers and their graphene nanocomposites, Macromolecules. 47 (2014) 3926–3941. doi:10.1021/ma500022x.

[200] M.-X. Li, S.-H. Kim, S.-W. Choi, K. Goda, W.-I. Lee, Effect of reinforcing particles on hydrolytic degradation behavior of poly (lactic acid) composites, Composites Part B: Engineering. 96 (2016) 248–254. doi:10.1016/j.compositesb.2016.04.029.

[201] X.-Z. Tong, F. Song, M.-Q. Li, X.-L. Wang, I.-J. Chin, Y.-Z. Wang, Fabrication of graphene/polylactide nanocomposites with improved properties, Composites Science and Technology. 88 (2013) 33–38. doi:10.1016/j.compscitech.2013.08.028.

[202] F. Mai, Y. Habibi, J.-M. Raquez, P. Dubois, J.-F. Feller, T. Peijs, E. Bilotti, Poly (lactic acid)/carbon nanotube nanocomposites with integrated degradation sensing, Polymer. 54 (2013) 6818–6823.

[203] E.M. Sullivan, Y.J. Oh, R.A. Gerhardt, B. Wang, K. Kalaitzidou, Understanding the effect of polymer crystallinity on the electrical conductivity of exfoliated graphite nanoplatelet/polylactic acid composite films, Journal of Polymer Research. 21 (2014). doi:10.1007/s10965-014-0563-8.

[204] M. Sabzi, L. Jiang, F. Liu, I. Ghasemi, M. Atai, Graphene nanoplatelets as poly(lactic acid) modifier: linear rheological behavior and electrical conductivity, Journal of Materials Chemistry A. 1 (2013) 8253–8261. doi:10.1039/C3TA11021D.

[205] C. Nethravathi, M. Rajamathi, Chemically modified graphene sheets produced by the solvothermal reduction of colloidal dispersions of graphite oxide., Carbon. 46 (2008) 1994–1998. doi:10.1016/j.carbon.2008.08.013.

[206] C. Bao, L. Song, W. Xing, B. Yuan, C. A. Wilkie, J. Huang, Y. Guo, Y. Hu, Preparation of graphene by pressurized oxidation and multiplex reduction and its polymer nanocomposites by masterbatch-based melt blending, Journal of Materials Chemistry. 22 (2012) 6088–6096. doi:10.1039/C2JM16203B.

[207] C. Hu, Z. Li, Y. Wang, J. Gao, K. Dai, G. Zheng, C. Liu, C. Shen, H. Song, Z. Guo, Comparative assessment of the strain-sensing behaviors of polylactic acid nanocomposites: reduced graphene oxide or carbon nanotubes, Journal of Materials Chemistry C. 5 (2017) 2318–2328. doi:10.1039/C6TC05261D.

[208] Z. Duan, N.L. Thomas, Water vapour permeability of poly(lactic acid): Crystallinity and the tortuous path model, Journal of Applied Physics. 115 (2014). doi:10.1063/1.4865168.

[209] C. Thellen, C. Orroth, D. Froio, D. Ziegler, J. Lucciarini, R. Farrell, N.A. D'Souza, J.A. Ratto, Influence of montmorillonite layered silicate on plasticized poly(l-lactide) blown films, Polymer. 46 (2005) 11716–11727. doi:10.1016/j.polymer.2005.09.057.

[210] G. Gorrasi, L. Tammaro, V. Vittoria, M.-A. Paul, M. Alexandre, P. Dubois, Transport properties of water vapor in polylactide/montmorillonite nanocomposites, Journal of Macromolecular Science - Physics. 43 B (2004) 565–575. doi:10.1081/MB-120030006.

[211] J.-W. Rhim, S.-I. Hong, C.-S. Ha, Tensile, water vapor barrier and antimicrobial properties of PLA/nanoclay composite films, LWT - Food Science and Technology. 42 (2009) 612–617. doi:10.1016/j.lwt.2008.02.015.

[212] M. Zenkiewicz, J. Richert, Permeability of polylactide nanocomposite films for water vapour, oxygen and carbon dioxide, Polymer Testing. 27 (2008) 835–840. doi:10.1016/j.polymertesting.2008.06.005.

[213] M. Zenkiewicz, J. Richert, A. Rózański, Effect of blow moulding ratio on barrier properties of polylactide nanocomposite films, Polymer Testing. 29 (2010) 251–257. doi:10.1016/j.polymertesting.2009.11.008.

[214] N. Tenn, N. Follain, J. Soulestin, R. Crétois, S. Bourbigot, S. Marais, Effect of nanoclay hydration on barrier properties of PLA/montmorillonite based nanocomposites, Journal of Physical Chemistry C. 117 (2013) 12117–12135. doi:10.1021/jp401546t.

[215] M.D. Sanchez-Garcia, E. Gimenez, J.M. Lagaron, Morphology and barrier properties of solvent cast composites of thermoplastic biopolymers and purified cellulose fibers, Carbohydrate Polymers. 71 (2008) 235–244. doi:10.1016/j.carbpol.2007.05.041.

[216] B. Tan, N.L. Thomas, Tortuosity model to predict the combined effects of crystallinity and nano-sized clay mineral on the water vapour barrier properties of polylactic acid, Applied Clay Science. 141 (2017) 46–54. doi:10.1016/j.clay.2017.02.014.

[217] G. Gorrasi, R. Pantani, M. Murariu, P. Dubois, PLA/halloysite nanocomposite films: Water vapor barrier properties and specific key characteristics, Macromolecular Materials and Engineering. 299 (2014) 104–115. doi:10.1002/mame.201200424.

[218] J.E. Tollar, Interfacial surface generator, US3239197 A, 1966. http://www.google.com/patents/US3239197 (accessed May 15, 2017).

[219] C.D. Mueller, S. Nazarenko, T. Ebeling, T.L. Schuman, A. Hiltner, E. Baer, Novel structures by microlayer coextrusion - Talc-filled PP, PC/SAN, and HDPE/LLDPE, Polymer Engineering and Science. 37 (1997) 355–362. doi:10.1002/pen.11678.

[220] D. Jarus, A. Hiltner, E. Baer, Microlayer coextrusion as a route to innovative blend structures, Polymer Engineering and Science. 41 (2001) 2162.

[221] M. Ponting, A. Hiltner, E. Baer, Polymer nanostructures by forced assembly: process, structure, and properties, in: Macromolecular Symposia, Wiley Online Library, 2010: pp. 19–32. http://onlinelibrary.wiley.com/doi/10.1002/masy.201050803/full (accessed May 13, 2017).

[222] H. Wang, J.K. Keum, A. Hiltner, E. Baer, B. Freeman, A. Rozanski, A. Galeski, Confined crystallization of polyethylene oxide in nanolayer assemblies, Science. 323 (2009) 757–760.

[223] M. Gupta, Y. Lin, T. Deans, E. Baer, A. Hiltner, D.A. Schiraldi, Structure and gas barrier properties of poly(propylene- graft -maleic anhydride)/phosphate glass composites prepared by microlayer coextrusion, Macromolecules. 43 (2010) 4230–4239. doi:10.1021/ma100391u.

[224] D.J. Sekelik, E.V. Stepanov, S. Nazarenko, D. Schiraldi, A. Hiltner, E. Baer, Oxygen barrier properties of crystallized and talc-filled poly(ethylene terephthalate), Journal of Polymer Science, Part B: Polymer Physics. 37 (1999) 847–857. doi:10.1002/(SICI)1099-0488(19990415)37:8<847::AID-POLB10>3.0.CO;2-3.

[225] R.Y.F. Liu, Y. Jin, A. Hiltner, E. Baer, Probing Nanoscale Polymer Interactions by Forced-Assembly, Macromolecular Rapid Communications. 24 (2003) 943–948. doi:10.1002/marc.200300051.

[226] W. Gao, Y. Zheng, J. Shen, S. Guo, Electrical properties of polypropylene-based composites controlled by multilayered distribution of conductive particles, ACS Applied Materials & Interfaces. 7 (2015) 1541–1549.

[227] M. Wen, X. Sun, L. Su, J. Shen, J. Li, S. Guo, The electrical conductivity of carbon nanotube/carbon black/polypropylene composites prepared through multistage stretching extrusion, Polymer. 53 (2012) 1602–1610. doi:10.1016/j.polymer.2012.02.003.

[228] S. Xu, M. Wen, J. Li, S. Guo, M. Wang, Q. Du, J. Shen, Y. Zhang, S. Jiang, Structure and properties of electrically conducting composites consisting of alternating layers of pure polypropylene and polypropylene with a carbon black filler, Polymer. 49 (2008) 4861–4870.

[229] C.-Y. Lai, A. Hiltner, E. Baer, L.T. Korley, Deformation of Confined Poly (ethylene oxide) in Multilayer Films, ACS Applied Materials & Interfaces. 4 (2012) 2218–2227.

[230] T.M. Burt, J. Keum, A. Hiltner, E. Baer, L.T. Korley, Confinement of elastomeric block copolymers via forced assembly coextrusion, ACS Applied Materials & Interfaces. 3 (2011) 4804–4811.

[231] F. Qiu, M. Wang, Y. Hao, S. Guo, The effect of talc orientation and transcrystallization on mechanical properties and thermal stability of the polypropylene/talc composites, Composites Part A: Applied Science and Manufacturing. 58 (2014) 7–15.

[232] E.M. Ivan'kova, M. Krumova, G.H. Michler, P.P. Koets, Morphology and toughness of coextruded PS/PMMA multilayers, Colloid and Polymer Science. 282 (2004) 203–208. doi:10.1007/s00396-003-0906-1.

[233] G. Miquelard-Garnier, A. Guinault, D. Fromonteil, S. Delalande, C. Sollogoub, Dispersion of carbon nanotubes in polypropylene via multilayer coextrusion: Influence on the mechanical properties, Polymer (United Kingdom). 54 (2013) 4290–4297. doi:10.1016/j.polymer.2013.06.007.

[234] X. Li, G.B. McKenna, G. Miquelard-Garnier, A. Guinault, C. Sollogoub, G. Regnier, A. Rozanski, Forced assembly by multilayer coextrusion to create oriented graphene reinforced polymer nanocomposites, Polymer. 55 (2014) 248–257. doi:10.1016/j.polymer.2013.11.025.

[235] L. Xia, H. Wu, S. Guo, X. Sun, W. Liang, Enhanced sound insulation and mechanical properties of LDPE/mica composites through multilayered distribution and orientation of the mica, Composites Part A: Applied Science and Manufacturing. 81 (2016) 225–233. doi:10.1016/j.compositesa.2015.11.023.

[236] S. Luo, L. Yi, Y. Zheng, J. Shen, S. Guo, Crystallization of polypropylene in multilayered spaces: Controllable morphologies and properties, European Polymer Journal. 89 (2017) 138–149. doi:10.1016/j.eurpolymj.2017.02.013.

[237] G. He, J. Li, F. Zhang, C. Wang, S. Guo, Effect of multistage tensile extrusion induced fiber orientation on fracture characteristics of high density polyethylene/short glass fiber composites, Composites Science and Technology. 100 (2014) 1–9.

[238] F. Zhang, M. Guo, K. Xu, G. He, H. Wu, S. Guo, Multilayered damping composites with damping layer/constraining layer prepared by a novel method, Composites Science and Technology. 101 (2014) 167–172.

[239] L. Shen, L. Xia, T. Han, H. Wu, S. Guo, Improvement of hardness and compression set properties of EPDM seals with alternating multilayered structure for PEM fuel cells, International Journal of Hydrogen Energy. 41 (2016) 23164–23172. doi:10.1016/j.ijhydene.2016.11.006.

[240] W. Cheng, N. Gomopoulos, G. Fytas, T. Gorishnyy, J. Walish, E.L. Thomas, A. Hiltner, E. Baer, Phonon dispersion and nanomechanical properties of periodic 1D multilayer polymer films, Nano Letters. 8 (2008) 1423–1428.

[241] J.-K. Tseng, S. Tang, Z. Zhou, M. Mackey, J.M. Carr, R. Mu, L. Flandin, D.E. Schuele, E. Baer, L. Zhu, Interfacial polarization and layer thickness effect on electrical insulation in multilayered polysulfone/poly (vinylidene fluoride) films, Polymer. 55 (2014) 8–14.

[242] C.-Y. Lai, M.T. Ponting, E. Baer, Influence of interdiffusion on multilayered gradient refractive index (GRIN) lens materials, Polymer. 53 (2012) 1393–1403.

[243] K.D. Singer, T. Kazmierczak, J. Lott, H. Song, Y. Wu, J. Andrews, E. Baer, A. Hiltner, C. Weder, Melt-processed all-polymer distributed Bragg reflector laser, Optics Express. 16 (2008) 10358–10363.

[244] J. Lott, C. Ryan, B. Valle, J.R. Johnson, D.A. Schiraldi, J. Shan, K.D. Singer, C. Weder, Two-Photon 3D Optical Data Storage via Aggregate Switching of Excimer-Forming Dyes, Advanced Materials. 23 (2011) 2425–2429.

[245] G. Zhang, P.C. Lee, S. Jenkins, J. Dooley, E. Baer, The effect of confined crystallization on high-density poly (ethylene) lamellar morphology, Polymer. 55 (2014) 663–672.

[246] C. Ryan, C.W. Christenson, B. Valle, A. Saini, J. Lott, J. Johnson, D. Schiraldi, C. Weder, E. Baer, K.D. Singer, J. Shan, Roll-to-roll fabrication of multilayer films for high capacity optical data storage, Adv. Mater. Weinheim. 24 (2012) 5222–5226, 5146. doi:10.1002/adma.201200669.

[247] B. Chen, W. Gao, J. Shen, S. Guo, The multilayered distribution of intumescent flame retardants and its influence on the fire and mechanical properties of polypropylene, Composites Science and Technology. 93 (2014) 54–60.

[248] Y. Lin, A. Hiltner, E. Baer, A new method for achieving nanoscale reinforcement of biaxially oriented polypropylene film, Polymer. 51 (2010) 4218–4224. doi:10.1016/j.polymer.2010.06.059.

[249] T.D. Fornes, D.R. Paul, Modeling properties of nylon 6/clay nanocomposites using composite theories., Polymer. 44 (2003) 4993–5013. doi:10.1016/S0032-3861(03)00471-3.

[250] R.A. Vaia, J.F. Maguire, Polymer Nanocomposites with Prescribed Morphology: Going beyond Nanoparticle-Filled Polymers., Chem. Mater. 19 (2007) 2736–2751. doi:10.1021/cm062693+.

[251] C.G. A.M. Pinto I.C. Gonçalves, F.D. Magalhães, Effect of biodegradation on PLA/graphene-nanoplatelets composites mechanical properties and biocompatibility, in: 2015.

[252] L.G. Cançado, A. Jorio, E.M. Ferreira, F. Stavale, C. Achete, R. Capaz, M. Moutinho, A. Lombardo, T. Kulmala, A. Ferrari, Quantifying defects in graphene via Raman spectroscopy at different excitation energies, Nano Letters. 11 (2011) 3190–3196.

[253] A. Das, B. Chakraborty, A.K. Sood, Raman spectroscopy of graphene on different substrates and influence of defects, Bulletin of Materials Science. 31 (2008) 579–584. doi:10.1007/s12034-008-0090-5.

[254] B. Andonovic, A. Ademi, A. Grozdanov, P. Paunović, A.T. Dimitrov, Enhanced model for determining the number of graphene layers and their distribution from X-ray diffraction data, Beilstein J Nanotechnol. 6 (2015) 2113–2122. doi:10.3762/bjnano.6.216.

[255] V. Kumar, T. Hanel, L. Giannini, M. Galimberti, U. Giese, Graphene reinforced synthetic isoprene rubber nanocomposites, KGK-KAUTSCHUK GUMMI KUNSTSTOFFE. 67 (2014) 38–46.

[256] F. Wang, L.T. Drzal, Y. Qin, Z. Huang, Mechanical properties and thermal conductivity of graphene nanoplatelet/epoxy composites, Journal of Materials Science. 50 (2014) 1082–1093. doi:10.1007/s10853-014-8665-6.

[257] C. McClory, T. McNally, M. Baxendale, P. Pötschke, W. Blau, M. Ruether, Electrical and rheological percolation of PMMA/MWCNT nanocomposites as a function of CNT geometry and functionality, European Polymer Journal. 46 (2010) 854–868.

[258] S.H. Lee, M.W. Kim, S.H. Kim, J.R. Youn, Rheological and electrical properties of polypropylene/MWCNT composites prepared with MWCNT masterbatch chips, European Polymer Journal. 44 (2008) 1620–1630.

[259] H.H. So, J.W. Cho, N.G. Sahoo, Effect of carbon nanotubes on mechanical and electrical properties of polyimide/carbon nanotubes nanocomposites, European Polymer Journal. 43 (2007) 3750–3756.

[260] M. Lisunova, Y.P. Mamunya, N. Lebovka, A. Melezhyk, Percolation behaviour of ultrahigh molecular weight polyethylene/multi-walled carbon nanotubes composites, European Polymer Journal. 43 (2007) 949–958.

[261] W. Bauhofer, J.Z. Kovacs, A review and analysis of electrical percolation in carbon nanotube polymer composites, Composites Science and Technology. 69 (2009) 1486–1498.

[262] R. Zhang, A. Dowden, H. Deng, M. Baxendale, T. Peijs, Conductive network formation in the melt of carbon nanotube/thermoplastic polyurethane composite, Composites Science and Technology. 69 (2009) 1499–1504. doi:10.1016/j.compscitech.2008.11.039.

[263] H. Deng, R. Zhang, E. Bilotti, J. Loos, T. Peijs, Conductive Polymer Tape Containing Highly Oriented Carbon Nanofillers, Journal of Applied Polymer Science. 113 (2009) 742–751. doi:10.1002/app.29624.

[264] E. Bilotti, R. Zhang, H. Deng, M. Baxendale, T. Peijs, Fabrication and property prediction of conductive and strain sensing TPU/CNT nanocomposite fibres, Journal of Materials Chemistry. 20 (2010) 9449–9455.

[265] I. Alig, D. Lellinger, M. Engel, T. Skipa, P. Pötschke, Destruction and formation of a conductive carbon nanotube network in polymer melts: In-line experiments, Polymer. 49 (2008) 1902–1909. doi:10.1016/j.polymer.2008.01.073.

[266] H. Deng, T. Skipa, R. Zhang, D. Lellinger, E. Bilotti, I. Alig, T. Peijs, Effect of melting and crystallization on the conductive network in conductive polymer composites, Polymer. 50 (2009) 3747–3754. doi:10.1016/j.polymer.2009.05.016.

[267] G.R. Kasaliwal, S. Pegel, A. Göldel, P. Pötschke Petra, G. Heinrich, Analysis of agglomerate dispersion mechanisms of multiwalled carbon nanotubes during melt mixing in polycarbonate, Polymer. 51 (2010) 2708–2720. doi:10.1016/j.polymer.2010.02.048.

[268] T. Villmow, P. Pötschke, S. Pegel, L. Häussler, B. Kretzschmar, Influence of twin-screw extrusion conditions on the dispersion of multi-walled carbon nanotubes in a poly(lactic acid) matrix, Polymer. 49 (2008) 3500–3509. doi:10.1016/j.polymer.2008.06.010.

[269] B.H. Cipriano, A.K. Kota, A.L. Gershon, C.J. Laskowski, T. Kashiwagi, H.A. Bruck, S.R. Raghavan, Conductivity enhancement of carbon nanotube and nanofiber-based

polymer nanocomposites by melt annealing., Polymer. 49 (2008) 4846–4851. doi:10.1016/j.polymer.2008.08.057.

[270] G.Z. Wu, S. Asai, C. Zhang, T. Miura, M. Sumita, A delay of percolation time in carbon-black-filled conductive polymer composites, Journal of Applied Physics. 88 (2000) 1480–1487. doi:10.1063/1.373843.

[271] H. Deng, E. Bilotti, R. Zhang, J. Loos, T. Peijs, Effect of thermal annealing on the electrical conductivity of high-strength bicomponent polymer tapes containing carbon nanofillers, Synthetic Metals. 160 (3) 337–344. doi:10.1016/j.synthmet.2009.11.001.

[272] M. Cadek, J. Coleman, V. Barron, K. Hedicke, W. Blau, Morphological and mechanical properties of carbon-nanotube-reinforced semicrystalline and amorphous polymer composites, Applied Physics Letters. 81 (2002) 5123–5125.

[273] D. Qian, E.C. Dickey, R. Andrews, T. Rantell, Load transfer and deformation mechanisms in carbon nanotube-polystyrene composites, Applied Physics Letters. 76 (2000) 2868–2870.

[274] M.A. Van Es, Polymer-clay nanocomposites: the importance of particle dimensions, TU Delft, Delft University of Technology, 2001.

[275] C. Sellam, Z. Zhai, H. Zahabi, O.T. Picot, H. Deng, Q. Fu, E. Bilotti, T. Peijs, High mechanical reinforcing efficiency of layered poly (vinyl alcohol)–graphene oxide nanocomposites, Nanocomposites. 1 (2015) 89–95.

[276] N.L. Batista, P. Olivier, G. Bernhart, M.C. Rezende, E.C. Botelho, Correlation between degree of crystallinity, morphology and mechanical properties of PPS/carbon fiber laminates, Materials Research-Ibero-American Journal of Materials. 19 (2016) 195–201. doi:10.1590/1980-5373-mr-2015-0453.

[277] X. Liu, M. Dever, N. Fair, R.S. Benson, Thermal and mechanical properties of poly (lactic acid) and poly (ethylene/butylene succinate) blends, Journal of Polymers and the Environment. 5 (1997) 225–235.

[278] K. Jamshidi, S.-H. Hyon, Y. Ikada, Thermal characterization of polylactides, Polymer. 29 (1988) 2229–2234. doi:10.1016/0032-3861(88)90116-4.

[279] V.S. Giita Silverajah, N.A. Ibrahim, W.M.Z.W. Yunus, H.A. Hassan, C.B. Woei, A Comparative Study on the Mechanical, Thermal and Morphological Characterization of Poly(lactic acid)/Epoxidized Palm Oil Blend, Int J Mol Sci. 13 (2012) 5878–5898. doi:10.3390/ijms13055878.

[280] M.J. Sobkowicz, R. Sosa, J.R. Dorgan, Supramolecular bionanocomposites, part 2: Effects of carbon nanoparticle surface functionality on polylactide crystallization, Journal of Applied Polymer Science. 121 (2011) 2029–2038.

[281] S.O. Han, M. Karevan, M.A. Bhuiyan, J.H. Park, K. Kalaitzidou, Effect of exfoliated graphite nanoplatelets on the mechanical and viscoelastic properties of poly (lactic acid) biocomposites reinforced with kenaf fibers, Journal of Materials Science. 47 (2012) 3535–3543.

[282] Y. Sun, C. He, Synthesis and Stereocomplex Crystallization of Poly(lactide)–Graphene Oxide Nanocomposites, ACS Macro Lett. 1 (2012) 709–713. doi:10.1021/mz300131u.

[283] Z. Tang, C. Zhang, X. Liu, J. Zhu, The crystallization behavior and mechanical properties of polylactic acid in the presence of a crystal nucleating agent, Journal of Applied Polymer Science. 125 (2012) 1108–1115.

[284] F. Mai, W. Tu, E. Bilotti, T. Peijs, Preparation and properties of self-reinforced poly(lactic acid) composites based on oriented tapes, Composites Part A: Applied Science and Manufacturing. 76 (2015) 145–153. doi:10.1016/j.compositesa.2015.05.030.

[285] Heat Deflection Temperature Testing of Plastics, (2014). Available from: http://www.matweb.com/reference/deflection-temperature.aspx.

[286] P. Russo, S. Cammarano, E. Bilotti, T. Peijs, P. Cerruti, D. Acierno, Physical properties of poly lactic acid/clay nanocomposite films: Effect of filler content and annealing treatment, J. Appl. Polym. Sci. 131 (2014) n/a-n/a. doi:10.1002/app.39798.

[287] Y. Xu, B. Higgins, W.J. Brittain, Bottom-up synthesis of PS-CNF nanocomposites, Polymer. 46 (2005) 799–810. doi:10.1016/j.polymer.2004.11.091.

[288] I. Alig, D. Lellinger, S.M. Dudkin, P. Pötschke, Conductivity spectroscopy on melt processed polypropylene-multiwalled carbon nanotube composites: Recovery after shear and crystallization, Polymer. 48 (2007) 1020–1029. doi:10.1016/j.polymer.2006.12.035.

[289] P. Miaudet, C. Bartholome, A. Derré, M. Maugey, G. Sigaud, C. Zakri, P. Poulin, Thermo-electrical properties of PVA-nanotube composite fibers, Polymer. 48 (2007) 4068–4074. doi:10.1016/j.polymer.2007.05.028.

[290] H. Deng, T. Skipa, E. Bilotti, R. Zhang, D. Lellinger, L. Mezzo, Q. Fu, I. Alig, T. Peijs, Preparation of High-Performance Conductive Polymer Fibers through Morphological Control of Networks Formed by Nanofillers, Advanced Functional Materials. 20 (2010) 1424–1432. doi:10.1002/adfm.200902207.

[291] H. Deng, R. Zhang, C.T. Reynolds, E. Bilotti, T. Peijs, A Novel Concept for Highly Oriented Carbon Nanotube Composite Tapes or Fibres with High Strength and Electrical Conductivity, Macromolecular Materials and Engineering. 294 (2009) 749–755. doi:10.1002/mame.200900151.

[292] A. Király, F. Ronkay, Temperature dependence of electrical properties in conductive polymer composites, Polymer Testing. 43 (2015) 154–162.

[293] B.H. Cipriano, Structure and Properties of Polymer Nanocomposites Containing Anisotropic Nanoparticles, University of Maryland, 2007.

[294] R.G. Larson, The structure and rheology of complex fluids, Oxford university press New York, 1999.

[295] A. Lele, M. Mackley, G. Galgali, C. Ramesh, In situ rheo-x-ray investigation of flow-induced orientation in layered silicate-syndiotactic polypropylene nanocomposite melt, Journal of Rheology. 46 (2002) 1091–1110. doi:10.1122/1.1498284.

[296] J. Ren, A.S. Silva, R. Krishnamoorti, Linear Viscoelasticity of Disordered Polystyrene-Polyisoprene Block Copolymer Based Layered-Silicate Nanocomposites., Macromolecules. 33 (2000) 3739–3746. doi:10.1021/ma992091u.

[297] G. Schmidt, A.I. Nakatani, P.D. Butler, A. Karim, C.C. Han, Shear orientation of viscoelastic polymer-clay solutions probed by flow birefringence and SANS, Macromolecules. 33 (2000) 7219–7222. doi:10.1021/ma9918811.

[298] M.J. Solomon, A.S. Almusallam, K.F. Seefeldt, A. Somwangthanaroj, P. Varadan, Rheology of polypropylene/clay hybrid materials, Macromolecules. 34 (2001) 1864–1872. doi:10.1021/ma001122e.

[299] R.G. Larson, The Structure and Rheology of Complex Fluids. (1999).

[300] J. Ren, B.F. Casanueva, C.A. Mitchell, R. Krishnamoorti, Disorientation Kinetics of Aligned Polymer Layered Silicate Nanocomposites., Macromolecules. 36 (2003) 4188–4194. doi:10.1021/ma025703a.

[301] B.H. Cipiriano, T. Kashiwagi, S.R. Raghavan, Y. Yang, E.A. Grulke, K. Yamamoto, J.R. Shields, J.F. Douglas, Effects of aspect ratio of MWNT on the flammability properties of polymer nanocomposites, Polymer. 48 (2007) 6086–6096. doi:10.1016/j.polymer.2007.07.070.

[302] J.Y. Rho, L. Kuhn-Spearing, P. Zioupos, Mechanical properties and the hierarchical structure of bone, Med Eng Phys. 20 (1998) 92–102.

[303] J. Sun, B. Bhushan, Hierarchical structure and mechanical properties of nacre: a review, RSC Adv. 2 (2012) 7617–7632. doi:10.1039/C2RA20218B.

[304] I. Corni, T.J. Harvey, J.A. Wharton, K.R. Stokes, F.C. Walsh, R.J.K. Wood, A review of experimental techniques to produce a nacre-like structure, Bioinspir Biomim. 7 (2012) 031001. doi:10.1088/1748-3182/7/3/031001.

[305] Z. Tang, N.A. Kotov, S. Magonov, B. Ozturk, Nanostructured artificial nacre, Nat Mater. 2 (2003) 413–418. doi:10.1038/nmat906.

[306] P. Podsiadlo, A.K. Kaushik, E.M. Arruda, A.M. Waas, B.S. Shim, J. Xu, H. Nandivada, B.G. Pumplin, J. Lahann, A. Ramamoorthy, N.A. Kotov, Ultrastrong and stiff layered polymer nanocomposites, Science. 318 (2007) 80–83. doi:10.1126/science.1143176.

[307] M. Dierendonck, S. De Koker, R. De Rycke, B.G. De Geest, Just spray it--LbL assembly enters a new age, Soft Matter. 10 (2014) 804–807. doi:10.1039/c3sm52202d.

[308] K. Shikinaka, K. Aizawa, N. Fujii, Y. Osada, M. Tokita, J. Watanabe, K. Shigehara, Flexible, transparent nanocomposite film with a large clay component and ordered structure obtained by a simple solution-casting method, Langmuir. 26 (2010) 12493–12495.

[309] J.J. Kochumalayil, S. Morimune, T. Nishino, O. Ikkala, A. Walther, L.A. Berglund, Nacre-mimetic clay/xyloglucan bionanocomposites: a chemical modification route for hygromechanical performance at high humidity, Biomacromolecules. 14 (2013) 3842–3849.

[310] K.W. Putz, O.C. Compton, M.J. Palmeri, S.T. Nguyen, L.C. Brinson, High-Nanofiller-Content Graphene Oxide–Polymer Nanocomposites via Vacuum-Assisted Self-Assembly, Advanced Functional Materials. 20 (2010) 3322–3329.

[311] E. Munch, M.E. Launey, D.H. Alsem, E. Saiz, A.P. Tomsia, R.O. Ritchie, Tough, bio-inspired hybrid materials, Science. 322 (2008) 1516–1520.

[312] O.T. Picot, V.G. Rocha, C. Ferraro, N. Ni, E. D'Elia, S. Meille, J. Chevalier, T. Saunders, T. Peijs, M.J. Reece, others, Using graphene networks to build bioinspired self-monitoring ceramics, Nature Communications. 8 (2017) 14425.

[313] G Santagiulianaa, OT Picot, L Rubinic, H Porwal, Y Li, H Zhang, NM Pugno, T Peijs, E Bilotti, The art of croissant-making to break the nanoparticle loading/ dispersion dichotomy in polymer nanocomposites, (2017) submited to Nature Materials.

[314] C. Luan, Baker's transformation and its irreversibility, Physics Letters A. 152 (1991) 6–10.

[315] D. Sekelik, E. Stepanov, S. Nazarenko, D. Schiraldi, A. Hiltner, E. Baer, Oxygen barrier properties of crystallized and talc-filled poly (ethylene terephthalate), Journal of Polymer Science Part B: Polymer Physics. 37 (1999) 847–857.

[316] R.M.A. l'Abee, A. Vissers, J.G.P. Goossens, A.B. Spoelstra, M. van Duin, Characterization of the morphology of co-extruded, thermoplastic/rubber multi-layer tapes, Analytica Chimica Acta. 654 (2009) 11–19.

[317] P.L.A. NatureworksŪ, polymer 2002D. Data Sheet. Natureworks LLC, 2005.

[318] P.L.A. NatureworksŪ, polymer 4032D. Data Sheet. Natureworks LLC, 2006.

[319] H. Li, M.A. Huneault, Effect of nucleation and plasticization on the crystallization of poly(lactic acid), Polymer. 48 (2007) 6855–6866. doi:10.1016/j.polymer.2007.09.020.

[320] H. Xiao, W. Lu, J.-T. Yeh, Effect of plasticizer on the crystallization behavior of poly(lactic acid), Journal of Applied Polymer Science. 113 (2009) 112–121. doi:10.1002/app.29955.

[321] F. Carrasco, P. Pagès, J. Gámez-Pérez, O.O. Santana, M.L. Maspoch, Processing of poly(lactic acid): Characterization of chemical structure, thermal stability and mechanical properties, Polymer Degradation and Stability. 95 (2010) 116–125. doi:10.1016/j.polymdegradstab.2009.11.045.

[322] J. Gámez-Pérez, J.C. Velazquez-Infante, E. Franco-Urquiza, F. Carrasco, O.O. Santana, M.L. Maspoch, others, Fracture behavior of quenched poly (lactic acid)., Express Polymer Letters. 5 (2011). http://www.expresspolymlett.com/articles/EPL-0001765_article.pdf (accessed September 24, 2017).

[323] I. Alig, P. Pötschke, D. Lellinger, T. Skipa, S. Pegel, G.R. Kasaliwal, T. Villmow, Establishment, morphology and properties of carbon nanotube networks in polymer melts, Polymer. 53 (2012) 4–28. doi:10.1016/j.polymer.2011.10.063.

[324] Y. Gao, O.T. Picot, E. Bilotti, T. Peijs, Influence of filler size on the properties of poly (lactic acid)(PLA)/graphene nanoplatelet (GNP) nanocomposites, European Polymer Journal. 86 (2017) 117–131.

[325] B. Liu, X. Feng, S.-M. Zhang, The effective Young's modulus of composites beyond the Voigt estimation due to the Poisson effect, Composites Science and Technology. 69 (2009) 2198–2204.

[326] R. Jan, P. May, A. P. Bell, A. Habib, U. Khan, J. N. Coleman, Enhancing the mechanical properties of BN nanosheet–polymer composites by uniaxial drawing, Nanoscale. 6 (2014) 4889–4895. doi:10.1039/C3NR06711D.

[327] F.M. Blighe, K. Young, J.J. Vilatela, A.H. Windle, I.A. Kinloch, L. Deng, R.J. Young, J.N. Coleman, The Effect of Nanotube Content and Orientation on the Mechanical Properties of Polymer–Nanotube Composite Fibers: Separating Intrinsic Reinforcement from Orientational Effects, Adv. Funct. Mater. 21 (2011) 364–371. doi:10.1002/adfm.201000940.

[328] K. Young, F.M. Blighe, J.J. Vilatela, A.H. Windle, I.A. Kinloch, L. Deng, R.J. Young, J.N. Coleman, Strong Dependence of Mechanical Properties on Fiber Diameter for Polymer−Nanotube Composite Fibers: Differentiating Defect from Orientation Effects, ACS Nano. 4 (2010) 6989–6997. doi:10.1021/nn102059c.

[329] M. Murariu, A.-L. Dechief, R. Ramy-Ratiarison, Y. Paint, J.-M. Raquez, P. Dubois, Recent advances in production of poly (lactic acid)(PLA) nanocomposites: a versatile method to tune crystallization properties of PLA, Nanocomposites. 1 (2015) 71–82.

[330] Y. Gao, O.T. Picot, H. Zhang, E. Bilotti, T. Peijs, Synergistic effects of filler size on thermal annealing-induced percolation in polylactic acid (PLA)/graphite nanoplatelet (GNP) nanocomposites, Nanocomposites. (2017) 1–9.

[331] S. Kashi, R.K. Gupta, T. Baum, N. Kao, S.N. Bhattacharya, Morphology, electromagnetic properties and electromagnetic interference shielding performance of poly lactide/graphene nanoplatelet nanocomposites, Materials & Design. 95 (2016) 119–126.

[332] Y.H. Chen, X.Y. Yao, Q. Gu, Z.J. Pan, Non-isothermal crystallization kinetics of poly (lactic acid)/graphene nanocomposites, Journal of Polymer Engineering. 33 (2013) 163–171. doi:10.1515/polyeng-2012-0124.

[333] R.B. Valapa, G. Pugazhenthi, V. Katiyar, Effect of graphene content on the properties of poly(lactic acid) nanocomposites, Rsc Advances. 5 (2015) 28410–28423. doi:10.1039/c4ra15669b.

[334] Z.Y. Song, X.X. Hou, L.Q. Zhang, S.Z. Wu, Enhancing Crystallinity and Orientation by Hot-Stretching to Improve the Mechanical Properties of Electrospun Partially Aligned Polyacrylonitrile (PAN) Nanocomposites, Materials. 4 (2011) 621–632. doi:10.3390/ma4040621.

[335] A. Saleem, L. Frormann, A. Iqbal, High performance thermoplastic composites: Study on the mechanical, thermal, and electrical resistivity properties of carbon fiber-reinforced polyetheretherketone and polyethersulphone, Polymer Composites. 28 (2007) 785–796. doi:10.1002/pc.20297.

[336] G. Choudalakis, A.D. Gotsis, Permeability of polymer/clay nanocomposites: A review, European Polymer Journal. 45 (2009) 967–984. doi:10.1016/j.eurpolymj.2009.01.027.

[337] H. Wu, J. Zhang, C. Zhang, J. Feng, M.A. Rahman, E. Baer, Structure–Properties Relationship of a Novel Multilayer Film/Foam Material Produced through Co-extrusion and Orientation, Ind. Eng. Chem. Res. 55 (2016) 10947–10954. doi:10.1021/acs.iecr.6b03418.

[338] J. Du, D. Liu, S. Chen, D. Wan, H. Pu, A novel method for fabricating continuous polymer nanofibers, Polymer. 102 (2016) 209–213. doi:10.1016/j.polymer.2016.09.018.

[339] R.J. Young, M. Liu, The microstructure of a graphene-reinforced tennis racquet, J Mater Sci. 51 (2016) 3861–3867. doi:10.1007/s10853-015-9705-6.

List of Publications

1. Gao, Y., Picot, O. T., Bilotti, E., & Peijs, T. (2017). Influence of filler size on the properties of poly (lactic acid)(PLA)/graphene nanoplatelet (GNP) nanocomposites. European Polymer Journal, 86, 117-131.

2. Gao, Y., Picot, O. T., Zhang, H., Bilotti, E., & Peijs, T. (2017). Synergistic effects of filler size on thermal annealing-induced percolation in polylactic acid (PLA)/graphite nanoplatelet (GNP) nanocomposites. Nanocomposites, 1-9.

3. Gao, Y., Picot, O. T., Tu, W., Bilotti, E., & Peijs, T. (2017). Multilayer co-extrusion of graphene polymer nanocomposites with enhanced structural organization and properties. Journal of Applied Polymer Science, Submitted.